

# Magnetic Properties of Electrical Steel, Power Transformer Core Losses and Core Design Concepts

Zur Erlangung des akademischen Grades eines

DOKTOR-INGENIEURS

an der Fakultät für  
Elektrotechnik und Informationstechnik  
des Karlsruher Institutes für Technologie (KIT)  
genehmigte

DISSERTATION

von

Dipl.-Ing. Christian Freitag  
geb. in: Malsch

|                             |                                 |
|-----------------------------|---------------------------------|
| Tag der mündlichen Prüfung: | 9. Februar 2017                 |
| Hauptreferent:              | Prof. Dr.-Ing. Thomas Leibfried |
| Korreferent:                | Prof. Dr.-Ing. Stefan Tenbohlen |



This document is licensed under the Creative Commons

Attribution 3.0 DE License

(CC BY 3.0 DE): <http://creativecommons.org/licenses/by/3.0/de/>

# Danksagung (Acknowledgments)

Die vorliegende Arbeit entstand während meiner Tätigkeit als wissenschaftlicher Mitarbeiter am Institut für Elektroenergiesysteme und Hochspannungstechnik (IEH) des Karlsruher Instituts für Technologie (KIT). Im Folgenden möchte ich mich bei allen bedanken, die mich während dieser Zeit begleitet und unterstützt haben.

Besonderer Dank gebührt Herrn Prof. Dr.-Ing. Thomas Leibfried für die Möglichkeit zur Promotion und die Übernahme des Hauptreferates. Des Weiteren danke ich ihm für das Interesse an meiner Arbeit, die hervorragenden Arbeitsbedingungen sowie die fachliche Förderung und Unterstützung.

Herrn Prof. Dr.-Ing. Stefan Tenbohlen von der Universität Stuttgart danke ich für die Übernahme des Korreferates und sein großes Interesse an der Thematik dieser Arbeit.

Bei allen ehemaligen und jetzigen Kollegen des Institutes bedanke ich mich für das angenehme Arbeitsklima und die gute Zusammenarbeit. Für den fachlichen Austausch und die hilfreichen Diskussionen auf dem Gebiet der Leistungstransformatoren bzw. deren Simulation möchte ich Herrn Dr.-Ing. Daniel Geißler und Herrn Dipl.-Ing. Benjamin Klaus herzlich danken. Ausdrücklich möchte ich Herrn Dr.-Ing. habil. Martin Sack erwähnen, der mir im Bereich Messtechnik wertvolle Hinweise und Anregungen gab.

Auch den Studierenden, die mir im Rahmen von studentischen Arbeiten und als wissenschaftliche Hilfskräfte bei der Forschungsarbeit bzw. anderen Aufgaben im Institut behilflich waren, möchte ich meinen Dank aussprechen.

Mein Dank gilt auch den Mitarbeiterinnen des Sekretariats und den Mitarbeitern der elektrischen sowie der mechanischen Werkstatt für ihr Engagement und ihre tatkräftige Unterstützung.

Weiterhin richtet sich mein Dank an Herrn Christian Joost, M. Sc. und Herrn Dipl.-Ing. Frank Sutter der Firma J. Schneider Elektrotechnik GmbH, die mich mit wertvollen Hinweisen und detaillierten Informationen im Bereich des Transformatorenbaus unterstützt haben.

Ganz besonders danke ich meinen Eltern, Irmgard und Heinrich Freitag, die mir das Studium ermöglicht und mich immer darin bestärkt haben.

Der größte Dank gehört Sarah Straub für ihren Rückhalt, ihre Unterstützung und ihr großes Verständnis während der letzten Jahre.

Karlsruhe, im Februar 2017

Christian Freitag

# Table of contents

- Kurzfassung (German Abstract)..... 7**
- 1 Introduction..... 9**
  - 1.1 Motivation ..... 9
  - 1.2 Objectives of the thesis ..... 11
    - 1.2.1 Measurement and modeling of magnetic properties ..... 11
    - 1.2.2 Investigation of transformer core losses ..... 11
    - 1.2.3 Improvements in transformer core design ..... 12
- 2 Fundamentals ..... 13**
  - 2.1 Power transformers..... 13
    - 2.1.1 Core setup ..... 14
    - 2.1.2 Stacking methods ..... 16
  - 2.2 Electrical steel..... 18
    - 2.2.1 Ferromagnetism and magnetic hysteresis ..... 18
    - 2.2.2 Iron losses ..... 21
  - 2.3 Maxwell equations ..... 24
- 3 Measurement of magnetic properties ..... 25**
  - 3.1 Measurement setup..... 25
    - 3.1.1 Hardware ..... 25
    - 3.1.2 Software..... 28
  - 3.2 Established measurement devices..... 35
    - 3.2.1 Epstein frame ..... 35
    - 3.2.2 Single sheet tester ..... 37
- 4 Modeling and characterization of magnetic properties..... 41**

|          |  |            |
|----------|--|------------|
| 4.1      | Specific total loss and specific apparent power .....                    | 41         |
| 4.2      | Hysteresis model based on harmonics in the magnetic field.....           | 44         |
| 4.3      | B(H) characteristics .....   | 50         |
| 4.4      | Magnetic anisotropy .....  | 54         |
| <b>5</b> | <b>Investigation of flux density orthogonal to the sheet plane .....</b> | <b>57</b>  |
| 5.1      | Measurement setup.....   | 57         |
| 5.2      | Construction of the NDT.....   | 61         |
| 5.3      | Evaluation of the NDT.....   | 62         |
| 5.3.1    | Parasitic effects.....   | 62         |
| 5.3.2    | Consideration of eddy currents .....                                     | 67         |
| 5.4      | Measurement and data analysis .....                                      | 71         |
| 5.4.1    | BH-curve determination.....  | 71         |
| 5.4.2    | Calculation of eddy current losses .....                                 | 78         |
| <b>6</b> | <b>Simulation of core losses.....</b>                                    | <b>83</b>  |
| 6.1      | Concept of FE simulation and post-processing.....                        | 83         |
| 6.2      | Validation with Single sheet tester model .....                          | 87         |
| 6.3      | Investigation of power transformers .....                                | 91         |
| 6.3.1    | Single phase transformer.....  | 91         |
| 6.3.1.1  | Transformer $T_1$ .....  | 91         |
| 6.3.1.2  | Transformer $T_2$ .....  | 99         |
| 6.3.2    | Three phase transformer.....   | 100        |
| 6.3.2.1  | Transformer $T_3$ .....  | 101        |
| 6.3.2.2  | Transformer $T_4$ .....  | 103        |
| 6.4      | Discussion.....  | 104        |
| <b>7</b> | <b>Core optimization.....</b>  | <b>107</b> |
| 7.1      | Mixed core design without change in geometry .....                       | 107        |

---

|          |  |            |
|----------|--|------------|
| 7.1.1    | Combination of different steel grades .....              | 107        |
| 7.1.2    | Core loss simulation .....                               | 111        |
| 7.1.3    | Load loss approximation .....                            | 112        |
| 7.1.4    | Cost consideration .....                                 | 113        |
| 7.2      | Mixed core design with change in geometry .....          | 115        |
| 7.2.1    | Analytic approximation of $TCO$ .....                    | 115        |
| 7.2.2    | Selection of different steel grades based on $TCO$ ..... | 118        |
| 7.2.3    | Validation with FE simulation .....                      | 120        |
| <b>8</b> | <b>Conclusion .....</b>                                  | <b>123</b> |
|          | <b>Appendix .....</b>                                    | <b>127</b> |
| A        | Measurement setup .....                                  | 127        |
| A.1      | Graphic user interface (GUI) .....                       | 127        |
| A.2      | Datasheets .....   | 130        |
| A.3      | Transfer ratios and calibration .....                    | 133        |
| B        | Tables and measured data .....                           | 136        |
| B.1      | Test certificate of transformer $T_1$ .....              | 136        |
| B.2      | Measured steel sheet data .....                          | 137        |
| C        | Bibliography .....                                       | 140        |
| C.1      | References .....   | 140        |
| C.2      | Standards .....  | 144        |
| C.3      | Author's publications .....                              | 145        |
| C.4      | Supervised thesis by author .....                        | 146        |
| D        | Nomenclature .....                                       | 147        |



# Kurzfassung (German Abstract)

Die vorliegende Arbeit umfasst die messtechnische Betrachtung der magnetischen Eigenschaften von Elektrolech, die Simulation von Leerlauf- und Kernverlusten in Leistungstransformatoren und reicht bis zur Untersuchung neuer Methoden zum Kerndesign. Der Schwerpunkt liegt auf der Reduktion von Leerlaufverlusten, denn diese treten fortwährend und unabhängig von der Last auf und bestimmen damit wesentlich Effizienz und Life-Cycle-Kosten von Leistungstransformatoren.

Der erste Teil der Arbeit beschäftigte sich mit der Messung der magnetischen Eigenschaften von Elektrolech, wobei ein eigenes Messsystem entwickelt und gebaut wurde. Es ermöglicht eine softwaregestützte und daher automatisierte Messung nach Norm und ist mit verschiedenen Messgeräten kompatibel; wie mit den etablierten Geräten Single-Sheet-Tester und Epsteinrahmen. Beide Messgeräte können die magnetischen Eigenschaften von Elektrolech innerhalb der Blechebene erfassen, eine Messung orthogonal zur Blechebene ist jedoch nicht möglich. Daher wurde ein neues Messsystem zur Untersuchung der magnetischen Charakteristika von Elektrolech senkrecht zur Blechebene entworfen. Die Eignung des Messgerätes wurde im Hinblick auf parasitäre Effekte wie beispielsweise Streuflüsse im Detail untersucht. Ein Vergleich der Ergebnisse entlang der Blechebene und senkrecht zur dieser zeigte signifikante Unterschiede auf. Mit den Messgeräten wurden Hysteresekurven, die das Elektrolech magnetisch komplett beschreiben, von sehr kleinen Aussteuerungen bis in die Sättigung aufgenommen. In einem weiteren Teil der Arbeit wurde ein Hysteresemodell vorgestellt, welches auf Messdaten basiert und eine Hysteresekurve für beliebige Aussteuerungen in guter Genauigkeit abbildet. Mit Hilfe dieses Modells wurden drei unterschiedliche Magnetisierungskurven bestimmt. Sie enthalten nur noch Informationen über die aussteuerungsabhängige Permeabilität des Elektrolechs, vernachlässigen indes die Hystereseeigenschaften. Die Reduktion der vielen einzelnen Hysteresen, die für das jeweilige Material aufgenommen wurden, zu einem Magnetisierungsverlauf, liefert jedoch eine einfache Beschreibung der magnetischen Eigenschaften des Elektrolechs.

Neben der direkten Untersuchung von Elektrolech, stand auch die Simulation der Kernverluste im Fokus der Arbeit. Es wurde eine Finite Elemente Analyse der betrachteten Transformatoren mit einem Post-Processing-Algorithmus kombiniert. Die Transformatoren wurden anhand von Konstruktionsdaten des Herstellers detailgetreu modelliert, vor allem in Bezug auf die geometrischen Abmessungen des Kerns. Die magnetischen Eigenschaften des im Kern verwendeten Elektrolechs wurden an einer Blechprobe gemessen

und mit den drei verschiedenen Magnetisierungskurven abgebildet. Es wurden daraufhin transiente Simulationen der jeweiligen Transformatoren durchgeführt um eine Flussdichteverteilung im Transformator kern in Abhängigkeit von der Aussteuerung zu generieren. Die Verteilung der Flussdichte wurde in ihrem zeitlichen Maximum exportiert und anschließend zur Berechnung der Kernverluste im Post-Processing-Algorithmus genutzt. Vergleiche von diesen Simulationsergebnissen mit Messungen am Transformator haben gezeigt, dass eine genaue Kenntnis der im Kern verwendeten Blechqualität nötig ist, um eine gute Übereinstimmung zu erzielen. Im Falle eines einphasigen Transformators konnte sichergestellt werden, dass die vermessene Blechprobe in Bezug auf Hersteller und Qualität dem Material im Kern entsprach. Hierbei ergaben sich geringe Abweichungen zwischen Simulation und Messung der Leerlaufverluste. Eine genaue Vorhersage der Verluste durch die Kombination aus Finite-Elemente-Simulation und Post-Processing-Algorithmus während der Planungs- und Konstruktionsphase des Transformators ist nun möglich. Hersteller greifen bisher nur auf Abschätzungen und Erfahrungswerte von bereits produzierten Transformatoren zurück. Die Leerlaufverluste sind daher bei der Wahl einer anderen Blechqualität oder Designanpassungen unbekannt, wohingegen das in dieser Arbeit vorgestellte Verfahren zur Bestimmung der Kernverluste eine verlässliche Angabe machen kann.

Die beschriebene Methode zur Simulation der Leerlaufverluste wurde im letzten Teil der Arbeit eingesetzt, um ein neues Kerndesignkonzept zu untersuchen, mit dem Ziel die Verluste zu reduzieren. Transformatorkerne bestehen bislang nur aus einer Blechqualität. In einem Mischkerndesign kamen nun zwei unterschiedliche Blechqualitäten bezüglich ihrer spezifischen Verluste zum Einsatz. Zu Vergleichszwecken bestand ein jeweiliger Referenzkern nur aus einer Blechsorte. Der Preis je Elektroblechsorte hängt von den spezifischen Verlusten ab, je geringer die Verluste, desto teurer ist das jeweilige Blech. Das Verhältnis der beiden Blechsorten im Mischkern wurde so gewählt, dass deren Gesamtkosten denen des Referenzkerns entsprechen. Neben der Blechwahl war eine Variation des Kernquerschnitts Teil der Designmethode, was sich sowohl auf die Herstellungskosten als auch auf die Gesamtverluste des Transformators auswirkte. Die Reduktion der Verluste durch das Mischkerndesign wurde zunächst analytisch abgeschätzt um geeignete Blechkombinationen zu finden. Die Ergebnisse der Abschätzung fanden Eingang in die Verlustsimulation, die eine realistischere und somit genauere Bestimmung der Kernverluste ermöglicht. Letztlich wurde das Mischkernkonzept aus ökonomischer Sicht, d.h. an Hand von Herstellungs- und Betriebskosten über die Lebensdauer des Transformators bewertet.

# 1 Introduction

In the 1830s the pioneer Michael Faraday discovered the principle of electromagnetic induction and laid the foundation for electric power to become the backbone of modern life. During the early days DC power was used in localized and isolated power grids, but with the invention of the power transformer at the end of the nineteenth century, the development of constant voltage AC supply systems became possible. With power stations located far away from the consumer, the usage of power transformers was of highest importance to transmit electric power over long distances with low losses. Since that time, transmission and distribution systems were restored in size and capacity to satisfy the growing demand of electricity in industry and households. There was a constant need for higher efficiency in these systems. After the Second World War, cold rolled electrical steel as a key component of power transformer cores was produced on a commercial scale offering significantly lower losses than the previously used materials. Developments during the middle of the 20<sup>th</sup> century in core design and manufacturing helped to reduce transformer losses even further.

Environmental friendly and renewable generation of electric power is the goal of politics today and leads to a more and more decentralized power generation. In the future, the number of large power plants like nuclear or coal-fired power stations in the GW range will decrease and at least partially replaced by solar and wind power. Especially wind farms installed offshore are planned to cover the demand of electrical energy, and in the case of Germany, a transmission via HVDC connection from coastal regions in the north to its industrial centers in the south are part of the future strategy. Moreover, also in this application, power transformers are a key element as a link between DC transmission and AC power supply for the consumer. Hence, power transformers are and will be an essential and highly critical component in the power transmission and distribution network which provides the infrastructure for growth and wealth in modern societies. The world without this quasi unlimited and always available electric power supply is unthinkable today.

## 1.1 Motivation

Power transformers are among the most valuable devices in the electric power grid. In the case of large power transformers, the purchase price could easily reach several million euros. Fig. 1.1 demonstrates the average composition of a purchase price belonging to

large power transformers. Approximately two-thirds of the price are true material costs including electrical steel, copper and other components like fixtures or tank. Electrical steel donates almost one-quarter of the price turning it into a key raw material used in power transformers. It is the component with the highest impact on efficiency and life cycle cost of power transformers.

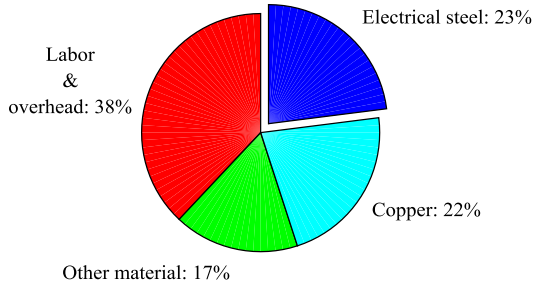


**Fig. 1.1:** Cost contribution of power transformer's purchase price, data is derived from [38, p. 11]

The efficiency of power transformers by means of core losses depends on the quality of the electrical steel used to build the core. Core losses as part of the no-load losses in transformers are estimated to contribute up to 5 % of the entire generated electric power [49, pp. 41-43]. They occur whenever a transformer is energized, and they are responsible for operational costs over the transformer's lifetime and could be at least in the same range as the previous purchase price.

Another important point is the eco-design requirements for power transformers according to COMMISSION REGULATION (EU) No 548/2014 [50] with regards to small, medium and large power transformers. This directive defines upper limits for no-load losses and lower limits for efficiency depending on rated power of transformers which will be tightened over the next years.

As a conclusion, it becomes clear that an increase of transformer efficiency is the answer for the mentioned aspects. Thus, the investigation of electrical steel's properties, the simulation of core losses and the development of a new core design method are in focus of this work.

## 1.2 Objectives of the thesis

### 1.2.1 Measurement and modeling of magnetic properties

Magnetic characteristics of electrical steel can be gauged with two different measurement devices, Epstein frame and Single sheet tester. Both devices are valid according to the standards IEC 60404-2 [72] and IEC 60404-3 [70]. In this thesis, a new measurement setup is built including hard- and software which enables measurements in compliance with the mentioned standards. However, Epstein frame and Single sheet tester can only record magnetic properties parallel to the sheet plane. Therefore, a new measurement device is developed offering the possibility to gauge magnetic properties of electrical steel orthogonal to the sheet plane.

The recorded hysteresis data from minor to major loops are reduced to a magnetization and a loss curve which are the main parameter sets to describe and grade magnetic properties of electrical steel. A new hysteresis model based on a Fourier expansion of the magnetic field is introduced and utilized to determine different magnetization curves also known as  $B(H)$  characteristics.

### 1.2.2 Investigation of transformer core losses

Core losses limit the efficiency of power transformers. Therefore, it is of great importance to be able to calculate core losses of a power transformer during its design stage. Nowadays, transformer manufacturers evaluate the no-load losses with core mass and loss curve of the used electrical steel. A weighting factor based on core design and experience is usually part of the estimation. However, the estimation might be inaccurate in the case of core design or material changes.

As part of this work, a simulation approach calculating transformer core losses is proposed. It relies on a combination of a Finite Element (FE) simulation and a post-processing algorithm. Several different transformers are analyzed, and their geometric dimensions as well as the magnetic properties of the used electrical steel expressed by magnetization and loss curves, are implemented in FE software. The simulation results are the basis for a novel post processing algorithm with the goal to calculate the core losses of each transformer.

### 1.2.3 Improvements in transformer core design

Power transformer cores typically consist of only one electrical steel grade, carefully chosen to meet no-load loss requirements of the customer. This work introduces a new core design method aiming at reducing core losses. Two different steel qualities with respect to their specific losses are assembled in one core. This mixed core design generates lower core losses compared to a reference core design made of only one steel grade with the same purchase price. The mixed core design could reduce life cycle cost of a power transformer considerably. A finite element simulation validates this new core design concept. Finally, economic aspects evaluate the loss reduction of a mixed transformer core design.

## 2 Fundamentals

In this chapter, background and basic information is given for a better understanding of the thesis. At first, the power transformer including all functional components is explained. The main focus is the core of the power transformer with regards to design and material. It consists of stacked electrical steel sheets. Stacking methods are described in detail, and their influence on efficiency is discussed. Further on, ferromagnetic phenomena as they occur in magnetic materials like electrical steel are explicated.

### 2.1 Power transformers

A transformer is a static electrical device without continuously moving parts from a physical point of view. It couples two or more electric circuits via induction and is part of an electric power system (see Fig. 2.1). There is a loose classification of transformers regarding their application in the electric energy system. Starting at the point of electric power production, a generator step-up transformer (GSU) is implemented which increases the output voltage of the generator for transmission. Different transmission systems by means of voltage level are connected via coupling transformers. On the way to the consumer the voltage is decreased again by step-down transformers. At the end point of the transmission, the voltage is finally reduced by distribution transformers to an appropriate level used in households [47, p. 3].

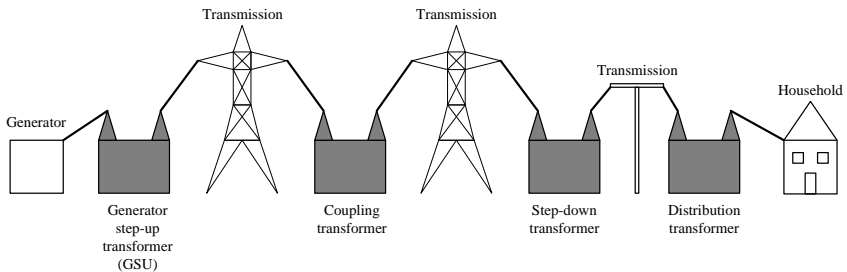


**Fig. 2.1:** Different applications of power transformers [47, p. 3]

Fig. 2.2 shows an 850 MVA generator step-up transformer (GSU) including all necessary components. The transformer's active part consists of core and windings placed in a steel

tank filled with oil. The oil fulfills the purpose of insulation and cooling. The compensator works as an oil overflow tank and controls the change in volume due to varying temperatures. Depending on the rated power of the transformer a forced cooling by radiators is possible. Bushings connect the transformer to the transmission network.

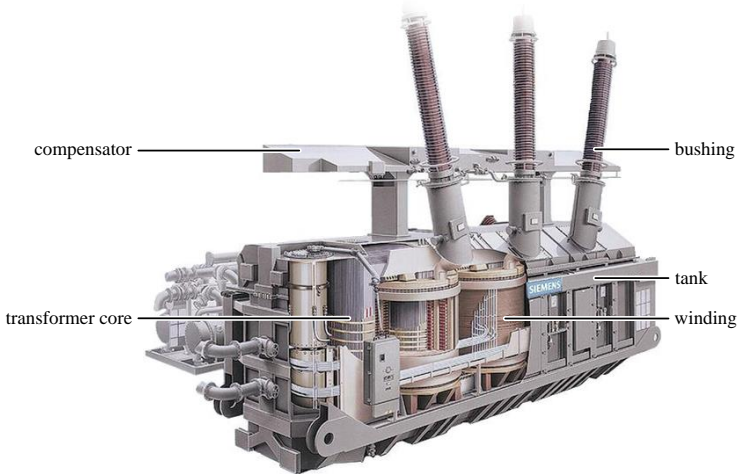


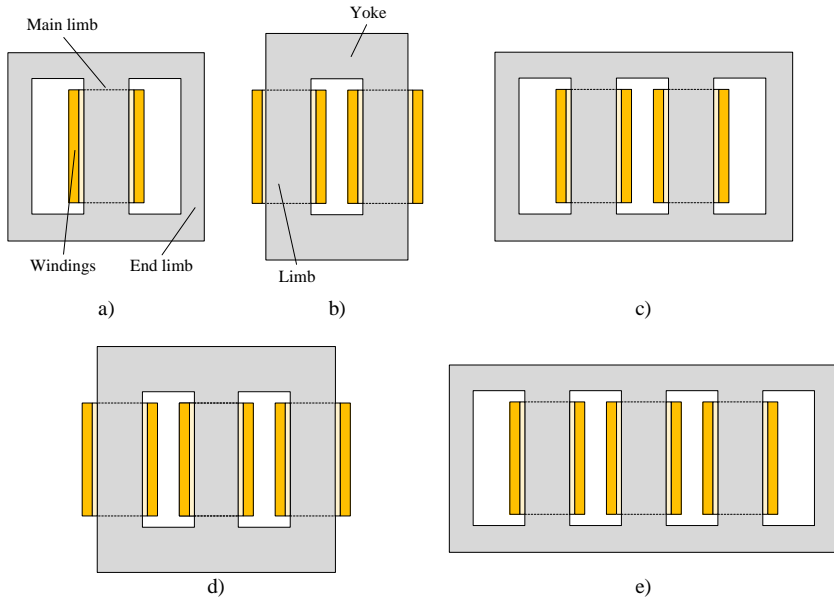
**Fig. 2.2:** Sketch of an 850 MVA generator step-up transformer including all necessary components, Siemens AG

This kind of liquid-immersed transformers are used for outdoor application whereas dry-type transformers are usually chosen for indoor operation [48, section 2.1]. In this work, the transformer core, its design and the magnetic characteristics of the material to build it are of interest. Hence, all other components of a power transformer are left aside.

### 2.1.1 Core setup

A transformer core is made of ferromagnetic material to assure a good magnetic coupling between the windings. However, it cannot be designed as a solid block which would cause high losses and further on heat in the core due to eddy currents. To reduce eddy currents, cores are laminated [48, section 1-4]. Cores of power transformers have usually core-type design [49, p. 14]. The coils are stacked or wrapped around the limbs of the core whereas the yokes close the magnetic circuit. Fig. 2.3 illustrates conventional core constructions of single phase applications. In setup a) the windings are wrapped around the main limb which has the double cross section as the two end limbs. This construction leads to equally halved flux in the end limbs. There are also single phase transformer designs where the

winding system is separated, and each part is placed on one limb as sketched in b). They are sometimes used for applications of high ratings due to their excellent short circuit capability. Both end limbs are equal in cross section. A further development of this design is demonstrated in c), where two end limbs smaller in cross section are part of the core. This four limb setup has the advantage of a reduced height which might be important for transportation of heavy weighted transformers.



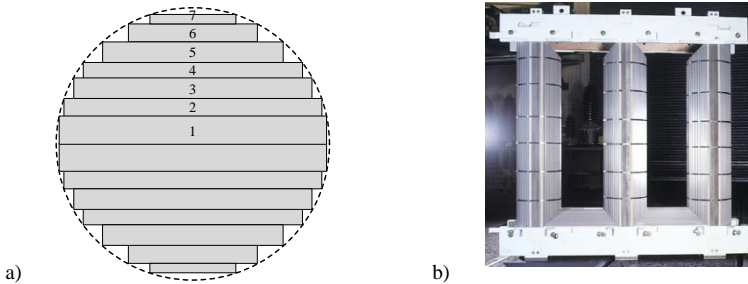
**Fig. 2.3:** Core constructions of single phase transformers (a – c)) and three phase transformers (d) and e)) [53, p. 39], [54, p. 93]

Fig. 2.3 also shows commonly utilized core designs in three phase applications. The design in d) is employed for small and medium-sized power transformers. The cross sections of limbs and yokes are the same. The flux generated by one phase in one limb passes through the other two, and no additional path is necessary which saves weight and material. However, as a matter of different magnetic path lengths comparing inner and outer limbs, no-load current and losses become asymmetric. Similar to the four limb single phase design in c), the five limb three phase setup in e) offers a height reduction to fulfill requirements of railway transport.

Technical specifications, limits in manufacturing and logistical constraints influence the chosen core construction. Under economic aspects, a three phase transformer is 20 % to 25 % less expensive than three connected single phase transformers for the same purpose.

Concerning redundancy, one single phase transformer as a spare unit could be more economically useful than an additional three phase transformer [53, pp. 38-40].

The core cross section approximates a circular shape in limbs and yokes to fill the cylindrical windings as good as possible (Fig. 2.4 a)). The number of steps in the cross section equals the amount of different stripe widths a manufacturer uses in the building process. Depending on the size of the transformer, up to seven steps are preferred in small cores whereas eleven or more are applied in cores of large power transformers like a GSU e.g. [49, pp. 106-108].



**Fig. 2.4:** Stepped cross section (a) and assembled core (b)) of a three phase three limb power transformer

Fig. 2.4 b) demonstrates an assembled core for a three phase application (compare Fig. 2.3 d)). To support the core structure, the top and bottom yokes are clamped with beams around each side of the yokes. They are connected directly by clamping bolts or indirectly by fixtures passing around the yokes. The last option leads to a bolt-less core generating significantly lower losses [54, pp. 98-102 ]. The limbs are supported by bands made of a high strength non-conductive material, which holds the laminations together and prevents vibrations in service [47, pp. 10-15].

### 2.1.2 Stacking methods

There are several approaches building a laminated core which is essential to reduce eddy current losses to an acceptable minimum. The core can be wound with one strip of electrical steel to produce a series of separate, concentric laminations per core step as explained in [51]. However, laid flat laminations build the main part of power transformer cores as sketched in Fig. 2.5. The area where an outer limb meets a yoke is termed L-joint while the region where inner limb and yoke unite is titled T-joint. Two forms of interleaved joints are common, squared and mitered joints. The squared form is popular for

cores made of non-grain orientated steel (Fig. 2.5 a)). When grain-orientated steel is applied, additional losses occurs where flux passes through sheet areas orthogonal to the grain-orientation. To benefit from the lower losses in grain-orientation, mitered joints are invented as illustrated in Fig. 2.5 b). The handling of mitered joints is more complex and therefore related to higher manufacturing costs compared to the squared joints. Nonetheless, this drawback is outweighed by the reduction of no-load losses [54, pp. 94-96]. The angle of overlap is between  $30^\circ$  to  $60^\circ$ , but an angle of  $45^\circ$  is usual [53, p. 41].

There are two stacking methods to handle mitered joints, single-step lap (SSL) and multi-step lap (MSL), both illustrated in Fig. 2.6 [52]. It is obvious that the SSL concept is less complex than the MSL method due to only two alternating steps. Nevertheless, cores based on MSL are more efficient as indicated by the red dashed lines in Fig. 2.6 which symbolize magnetic flux. Above and below the air gaps the flux density is higher in SSL than in MSL joints producing extra losses in these areas [46]. Thus, the MSL stacking method is applied even in small power transformers such as distribution transformers because the ratio of joint and core volume is higher for small transformers amplifying the benefit of the MLS concept [49, p. 117].

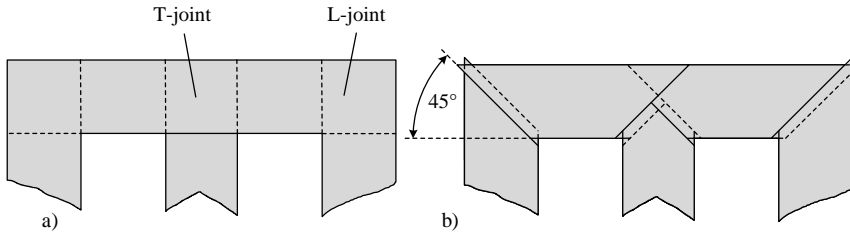


**Fig. 2.5:** Squared (a) and mitered (b) joints

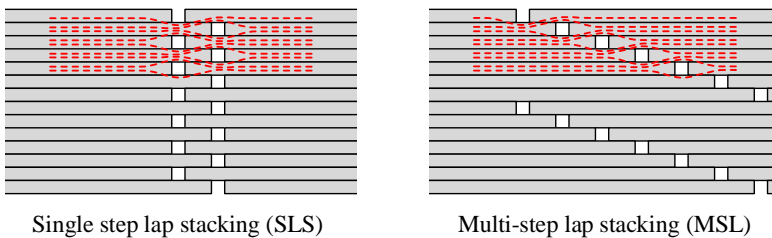


**Fig. 2.6:** Stacking methods in mitered joints

In [40, 41, 52] the impact of air gap length and number of laminations per step are investigated coming to the conclusion, that a small number of laminations per step (best option

would be one) and an air gap length as short as possible lead to few losses. The number of steel sheets per layer also plays an important role. One sheet per layer generates lower losses but causes high labor costs due to more complex core manufacturing. Hence, two sheets per layer are commonly used in core manufacturing [53, p. 43]. An own test stand to investigate different MSL arrangements is developed in [86] and published in [76].

Fig. 2.7 gives an example of an L-joint in a two limb single phase transformer based on MSL stacking method (see the sketch for exact location). The overlapping corners of the different laminations are clearly visible. One lamination consists of three steel sheets. And three steps in yoke and limb direction respectively are part of the MSL.

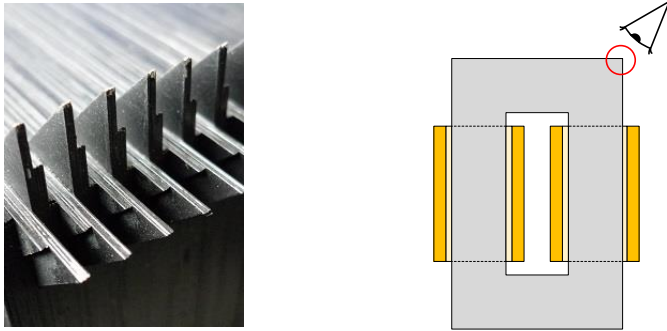


**Fig. 2.7:** Example of MSL in a single phase transformer core

## 2.2 Electrical steel

Cores in power transformers consist of laminated electrical steel. Its characteristics determine the efficiency of power transformers which are explained in the following subsections.

### 2.2.1 Ferromagnetism and magnetic hysteresis

Magnetic phenomena are described by magnetic field  $H$  and magnetic flux density  $B$ .  $H$  represents the movement of charges and  $B$  stands for force on charges. Both quantities follow the principle of cause and effect. Their relationship is expressed by equation (2.1), whereas the constant  $\mu_0$  is the absolute permeability of  $4\pi \cdot 10^{-7}$  Vs/Am. The relative permeability  $\mu_r$  has a value of 1 in vacuum, but it varies if magnetic material is present.

$$B = \mu_r \mu_0 H \quad (2.1)$$

The introduction of another field quantity, the polarization  $J$ , which denotes the effect of material allows to rewrite equation (2.1) as follows:

$$B = \mu_0 H + J . \quad (2.2)$$

The polarization is defined by  $\mu_0$  and the magnetization  $M$ :

$$J = \mu_0 M . \quad (2.3)$$

Further, the ratio  $M$  and  $H$  gives the magnetic susceptibility  $\chi_m$  expressing the influence of material on the magnetic quantities without their dependency in vacuum (2.4).

$$\chi_m = \frac{M}{H} = \mu_r - 1 \quad (2.4)$$

The behavior of  $\mu_r$  and  $\chi_m$  is a material characteristic, in the case of  $\mu_r \gg 1$  and  $\chi_m \gg 0$  it is called ferromagnetic. There are other magnetic effects like para- and diamagnetism, but in this work, only ferromagnetism is discussed because electrical steel is a ferromagnetic material [61, pp. 183-185]. They contain elementary magnetic moments of quantum-mechanical origin. Ferromagnetism occurs when all magnetic moments are orientated in the same direction, but according to Weiss<sup>1</sup>, the ferromagnetic material is subdivided into magnetic domains which could have different orientations [39, pp. 4-6]. The domain distribution is established to reach a status of minimum free energy. Fig. 2.8 illustrates the formation of a domain wall structure which minimizes its free energy from left to right. At first, leakage flux closes the magnetic circuit. The domains are separated until the magnetization is zero, and the material contains the whole energy inside it.

---

<sup>1</sup> Pierre-Ernest Weiss, Physicist: \* 25.03.1865; † 24.10.1940

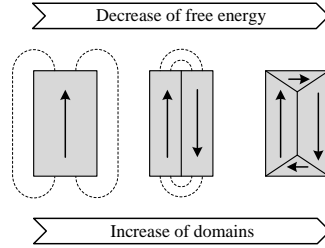


**Fig. 2.8:** Formation of a domain wall structure [44, p. 11]

There is a thin layer between two domains called Bloch<sup>2</sup> domain wall, in which the elementary magnetic moments reverse their alignment (Fig. 2.9).

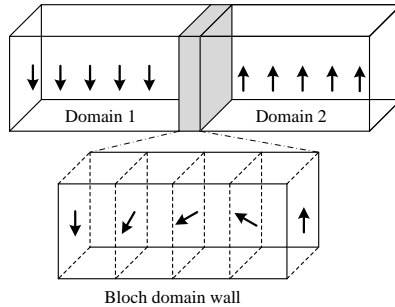


**Fig. 2.9:** Bloch domain wall [61, p. 195]

The interaction of domains and domain walls during the process of magnetization determine the magnetization and hysteresis behavior of a certain material. Five different parts characterize this process of magnetization. At the beginning in part I, the material is entirely demagnetized, all elementary magnetic moments compensate each other, and macroscopically the magnetization is zero. A small magnetic field is applied in the next state (II), and the domains in a similar direction of the applied field grow while all others decrease. This wall movement is reversible in case of small fields which means the previous state (I) is obtained with no field present and a hysteresis does not appear. While the field rises, an irreversible domain wall movement occurs in section III. Hysteresis is now part of the process. Some domain walls stay in position if the magnetic field is reduced and the material remains partly magnetized. During this state of magnetization, the highest permeability arises. In part IV a rotation of the magnetization appears until it is aligned with the applied field. The permeability is small in this region of the magnetization curve.

<sup>2</sup> Felix Bloch, Physicist: \* 23.10.1905; † 10.09.1983

If the magnetic field is increased even further, magnetic saturation by means of the saturation flux density  $B_S$  is reached in section V, and the relative permeability equals 1. The absolute permeability expresses the coupling between the magnetic field and flux density. The red dashed line indicates a typical hysteresis loop in Fig. 2.10. At the crossing of hysteresis curve and  $B$ -axis the magnetic field is zero but the material remains magnetized with the remanent flux density  $B_R$ . To reduce  $B_R$  to zero, a certain magnetic field value called coercivity  $H_C$  must be applied. It is used to classify ferromagnetic materials. A small coercivity characterizes soft magnetic materials like electrical steel, whereas a high  $H_C$  describes hard magnetic materials as they chosen for permanent magnets. The area of the hysteresis loop describes the necessary work to magnetize a material from positive to negative saturation and back. Hence, a small coercivity means less work and therefore lower losses which is suitable for power transformers [44, pp. 11-12].

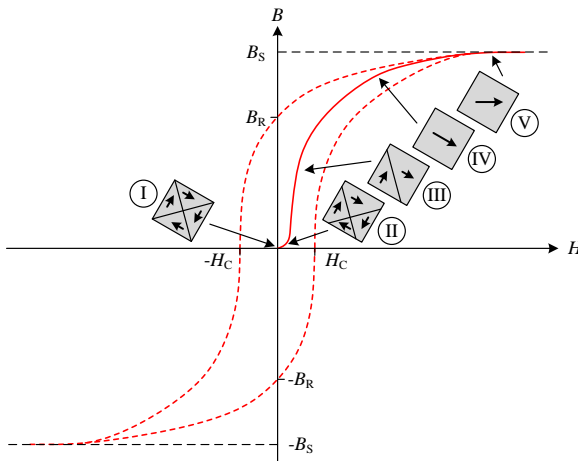


**Fig. 2.10:** Magnetization and hysteresis curve with different states of magnetization [44, p. 12, 61, p. 197]

## 2.2.2 Iron losses

Electrical steel is a polycrystalline material, and these crystals or grains show a strong magnetic anisotropy. They develop an entirely different magnetic behavior depending on the direction of the magnetic field. In the 1930s Norman Goss<sup>3</sup> invented a process of cold-rolling and heat-treatment for electrical steel which improved the magnetic properties significantly along the rolling direction of the sheet [45]. This process orders the grains in

<sup>3</sup> Norman P. Goss: \* 02.04.1902; † 28.10.1977

the direction of the best magnetic characteristics and achieves a high degree of preferred crystal orientations [42].

The ordered direction of crystals or grains is termed Goss texture characterizing cold-rolled-grain-oriented electrical steel. Power transformer cores are made of this product which is called electrical steel from now on for convenience.

As mentioned in the previous section, the work processed during an entire slope of the hysteresis curve can be expressed by its covered area. Equation (2.5) explains this conclusion [1, p. 57]. The specific work  $W_s$  describes the work per unit mass whereas the variable  $\rho$  gives the mass density. In a time varying field, the specific power  $P_s$  equals the time-related average of the specific work over one cycle  $T$ . The magnetization changing with time is assumed to be sinusoidal for the following statements in this chapter.

$$W_s = \frac{1}{\rho} \int_0^B H dB$$

$$P_s = \frac{1}{\rho} \frac{1}{T} \int_0^T H \frac{dB}{dt} dt$$
(2.5)

The specific power  $P_s$  is also known as specific total loss and is used to characterize the quality of electrical steel (compare section 4.1). According to [43],  $P_s$  can be separated into three different loss components regarding the origin of the power loss. There are specific hysteresis  $P_{s,H}$ , eddy current  $P_{s,EC}$  and excess or anomalous loss  $P_{s,EX}$  (2.6).

$$P_s = P_{s,H} + P_{s,EC} + P_{s,EX}$$
(2.6)

All three loss components are related to eddy currents, but their way and place of generation inside electrical steel is different. Hysteresis loss occurs while small domain wall segments alternate between local minima of the system free energy creating localized eddy currents and as a result losses around the jumping walls [39, pp. 26-27]. This kind of loss is found to be proportional to the frequency  $f$  of the magnetizing field and to be depended on the flux density amplitude  $\hat{B}$  squared leading to equation (2.7).

$$P_{s,H} = C_0 \hat{B}^2 f$$
(2.7)

The second term in equation (2.6) belongs to the classical eddy current loss determined by the geometry of the conductive material. The detailed deviation is given in [62] leading to equation (2.8) which is only valid for thin conductive layers.

$$P_{s,EC} = \frac{\pi^2 \sigma d^2}{6\rho} (\hat{B}f)^2 \quad (2.8)$$

The classical eddy current loss relies on flux density amplitude  $\hat{B}$  and frequency  $f$  squared as well as on the material properties density  $\rho$ , conductivity  $\sigma$  and the thickness of the sheet  $d$  [43]. To minimize this loss component, 3 % silicon is added during the production process of electrical steel to reduce the conductivity. A higher percentage of silicon increases the brittleness of the material which is problematic for cutting the sheets. Another option is a small thickness of the steel sheets explaining why transformer cores are made of laminated electrical steel. Thicknesses in between 230  $\mu\text{m}$  and 350  $\mu\text{m}$  are commonly used [69], but there are also high-performance steel qualities with a thickness of 180  $\mu\text{m}$  [64]. A thin insulation layer called coating covers the sheet from each side to prevent eddy currents [68]. It is described as glass film with a thickness of 2  $\mu\text{m}$  to 5  $\mu\text{m}$  [64]. Both possibilities, silicon content and sheet thickness complicate core manufacturing and therefore a compromise between handling and loss reduction is necessary [56].

The final term in equation (2.6) is named excess loss due to a difference in estimated losses based on the two first components ( $P_{s,H} + P_{s,EC}$ ) and measured losses (2.9). It depends on the product of flux density and frequency by the power of 1.5.

$$P_{s,EX} = C_1 (\hat{B}f)^{1.5} \quad (2.9)$$

Eddy currents around domain walls moved by the driving action of the external field generate this kind of loss [39, pp. 26-27]. Since excess loss depends on the scale of magnetic domains, their size needs to be decreased. Laser or mechanical scribing perpendicular to the rolling direction produces localized stresses at the surface of the sheet leading to a domain refinement which reduces excess loss significantly [47, pp. 448-450].

The parameters  $C_0$  (2.7) and  $C_1$  (2.9) can be best determined at a flux density amplitude of 1.5 T and two different magnetization frequencies in between 20 Hz and 100 Hz. Doing so, equation (2.6) delivers a relative deviation between calculated and measured losses of +/- 10 % in a flux density range of 0.7 T to 1.7 T [43]. Despite these variances, commercial software commonly implements the explained loss calculation method to model and simulate iron losses in electrical steel [58].

## 2.3 Maxwell equations

The Finite Element Method (FEM, also called Finite Element Analysis (FEA)) is used in ANSYS Maxwell which is the FE software applied in this work to simulate flux density and magnetic field distributions in electromagnetic devices such as magnetic measurement equipment or power transformers. The applied frequencies are small, and a change in field quantities happens simultaneously at every point of the model. Thus, simplifications according to conduction fields with skin effect are allowed here [59, pp. 120-125], leading to the relevant Maxwell and material equations:

$$\begin{aligned}\nabla \times \vec{E}(t) &= -\frac{\partial \vec{B}(t)}{\partial t} \\ \nabla \times \vec{H}(t) &= \vec{J}_1(t) \\ \nabla \cdot \vec{B}(t) &= 0\end{aligned}\tag{2.10}$$

and

$$\begin{aligned}B &= \mu \cdot H \\ J_1 &= \sigma \cdot E.\end{aligned}\tag{2.11}$$

Based on both sets of equations, a relationship of magnetic field  $H$  and flux density  $B$  can be found:

$$\nabla \times \left( \frac{1}{\sigma} \nabla \times \vec{H}(t) \right) = -\frac{\partial \vec{B}(t)}{\partial t}.\tag{2.12}$$

Equation (2.12) is used for transient, low-frequency application including nonlinear magnetization characteristics of the modeled materials [57]. Further details about the FEM are stated in [55].

## 3 Measurement of magnetic properties

The magnetic properties of electrical steel are gauged in compliance with the standards IEC 60404-2 [72] and IEC 60404-3 [70]. These standards describe the test setup and provide all necessary requirements. At first, the measurement setup is explained while the details of three different measurement devices are given later.

### 3.1 Measurement setup

The aim of the measurement setup is to record hysteresis curves from minor to major loops within a magnetic polarization  $\hat{J}$  of 0.05 T to 1.95 T. Additionally a frequency range of 25 Hz to 300 Hz is provided. The hysteresis loops are gauged automatically across the polarization and frequency range. The used hardware must be compatible with three different measurement devices. A graphic user interface (GUI) running on a computer controls all measurements.

#### 3.1.1 Hardware

The appendix of IEC 60404-3 [70] explains conditions for a digital hardware setup. A minimum resolution of the A/D converter of 12 bit and a simultaneous recording of all measured signals are required. To avoid a phase shift between signals, multiplexed analog inputs are not recommended. Further requirements are discussed in the software section 3.1.2.

The setup to measure magnetic characteristics consists of one measurement device, a power supply as well as a data acquisition and signal generation unit (see Fig. 3.1). All three measurement devices behave like a single phase transformer without load in a first approach. The magnetic field  $H$  and the magnetic polarization  $J$  inside the core of the transformer, which characterize the investigated steel sheet samples, are computed with Ampere's and Faraday's law. The primary current  $I_1$ , the number of turns in the primary winding  $N_1$  and the magnetic path length  $l_{Fe}$  are needed for the magnetic field calculation (3.1). However, there are also other approaches to determine the magnetic field strength using field sensing coils as stated in [63].

The polarization  $J$  is calculated with the secondary voltage  $U_2$ , the number of turns in the secondary winding  $N_2$ , the cross section of the investigated steel sheet samples  $A_{\text{Fe}}$  and the applied frequency  $f$  (3.2). Due to the compensation of air flux in the measurement device (compare subsection 3.2.1), the secondary voltage  $U_2$  is related to the polarization  $J$  and not to the flux density  $B$ .

$$H(t) = I_1(t) \frac{N_1}{l_{\text{Fe}}} \quad (3.1)$$

$$J(t) = \frac{1}{N_2 A_{\text{Fe}}} \int U_2(t) dt \quad (3.2)$$

The flux density  $B$  equals the sum of polarization  $J$  and the magnetic field  $H$  multiplied with the absolute permeability  $\mu_0$ . The polarization contributes the magnetization of the magnetically active material and the second term denotes flux density in vacuum.

$$B(t) = J(t) + \mu_0 \cdot H(t) \quad (3.3)$$

Fig. 3.1 and Fig. 3.2 provide a detailed overview of the measurement setup. The explanation follows the signal processing. The voltage drop across a high precision shunt resistor  $R_{\text{shunt}}$  of  $0.5 \Omega$  (tolerance:  $0.1 \%$ , temperature drift:  $10 \text{ ppm/K}$ ) represents the primary current  $I_1$ . An ohmic voltage divider reduces the secondary voltage  $U_2$  of the measurement device with a transfer ratio of  $0.8:1$ . Metal film resistors of the E96 row with a temperature drift of  $50 \text{ ppm/K}$  are used. The entire input resistance yields  $20 \text{ k}\Omega$  and fulfills the requirements in [70] of at least  $1 \text{ k}\Omega/\text{V}$ , since the maximum value of  $U_2$  is always below  $20 \text{ V}$ . Both signals do not need to be amplified to the input voltage range of  $\pm 10 \text{ V}$  of the data acquisition and signal generation unit DT9847 (see Appendix A.2) because of its high resolution of 24 bit. Even signals in the millivolt range can be recorded easily without quantization errors. The signal inputs for the voltage  $U_2$  and the voltage drop generated by the current  $I_1$  work simultaneously to avoid phase shift between the signals due to multiplexing. The DT9847 also generates an analog output voltage which is amplified by a four-quadrant chopper and then applied to the measurement device. Another task of the data acquisition and generation unit is the communication with a PC via USB connection. Software running on this PC controls the entire measurement. A four-quadrant chopper DCP 520/30 (see Appendix A.2) works as a power supply with a rated power of  $500 \text{ W}$ . It linearly amplifies the output voltage of the data acquisition and generation unit and creates the primary voltage for each measurement device. This four-quadrant chopper can be described as a power operational amplifier equipped with an external circuit (Fig. 3.2)

creating a gain of 5.3 combined with a maximum output voltage of 25 V and a maximum output current of 20 A.

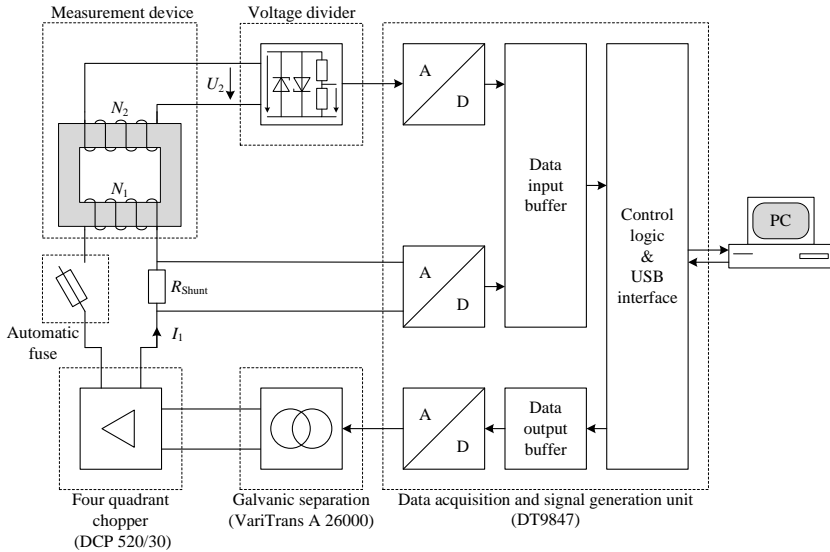


**Fig. 3.1:** Sketch of the measurement setup

Electromagnetic Compatibility (EMC) is additionally considered in the measurement setup. Signals in the millivolt range need to be gauged which are very sensitive to electromagnetic interferences. Hence, all signal lines are kept as short as possible and are realized with coax cables. Furthermore, the power supply is galvanic separated to the grid by the use of an isolation transformer, which blocks disturbances on personal earth. To avoid the influence of radiated disturbances the entire measurement setup is located in a shielded room.

A safety concept is also part of this measurement configuration. An automatic fuse in the supply path (Fig. 3.1) prevents too high currents which might destroy a measurement device. A sudden change in primary current could induce a high secondary voltage. The analog inputs tolerate a maximum voltage of 60 V. Hence, two anti-parallel suppressor diodes with a rated voltage of 24 V protect the secondary voltage input. They are integrated into the voltage divider. A further safety feature is the galvanic separation (VariTrans 26000 A, see Appendix A.2) of generated and amplified signal to produce the supply voltage.

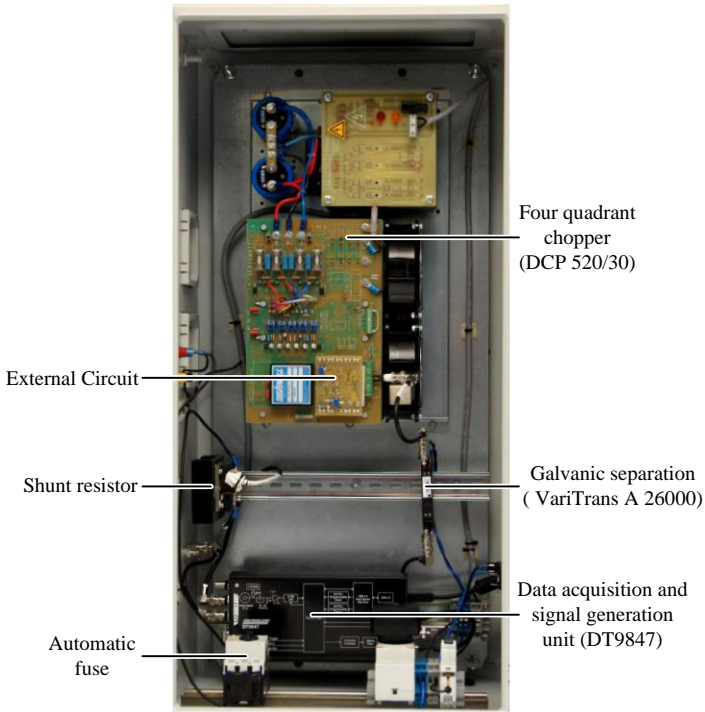


**Fig. 3.2:** Picture of the measurement setup

### 3.1.2 Software

A program implemented in the numerical analysis software MATLAB controls the measurement procedure. A graphic user interface (GUI) is part of it and offers an easy handling of magnetic properties measurements. It visualizes measured signals, calculates results and indicates controller progress. The software behind the GUI is responsible for automatic measurements including sample demagnetization and secondary voltage control. Further tasks are the calculation of magnetic properties and data storage of results.

Fig. 3.3 demonstrates a flowchart of the software with all its steps. In the beginning, measurement device and sample parameters are initialized, and an appropriate demagnetization voltage is defined. The investigated steel sheet samples need to be demagnetized to avoid

the influence of a possible magnetic remanence on the measurements. As stated in [60] the sample is magnetized to saturation, and then the flux density is decreased to zero by a sinusoidal excitation voltage with a linearly descending amplitude. The user adjusts the parameters such as voltage amplitude, frequency as well as rise and fall time. A frequency between 5 Hz and 10 Hz, a rise time of 1 s plus a fall time of 10 s are recommended. The voltage amplitude depends on the measurement device and must induce magnetic saturation in the sample. The demagnetization of steel is investigated and simulated based on an own test setup in [75, 80, 81, 85].

In a next step, the user can choose the polarization and frequency ranges from 0.05 T to 1.95 T and 25 Hz to 300 Hz with an arbitrary step size. During the measurement of each polarization and frequency step, the sample is demagnetized at first, and after that, the control of the sinusoidal waveform of the secondary voltage comes into action. When the allowed error values regarding polarization amplitude and the sinusoidal waveform of the secondary voltage are accomplished, the sinus control stops and the generated primary voltage is applied to the measurement device for an arbitrary number of periods. In the meanwhile, the software records the secondary voltage and calculates the magnetic characteristics of the investigated steel sheet samples. Finally, measured and calculated data is stored on the hard drive of the PC. In the following section, the relevant parts of the measurement loop are explained in detail. Appendix A.1 illustrates pictures of the GUI with all its features.

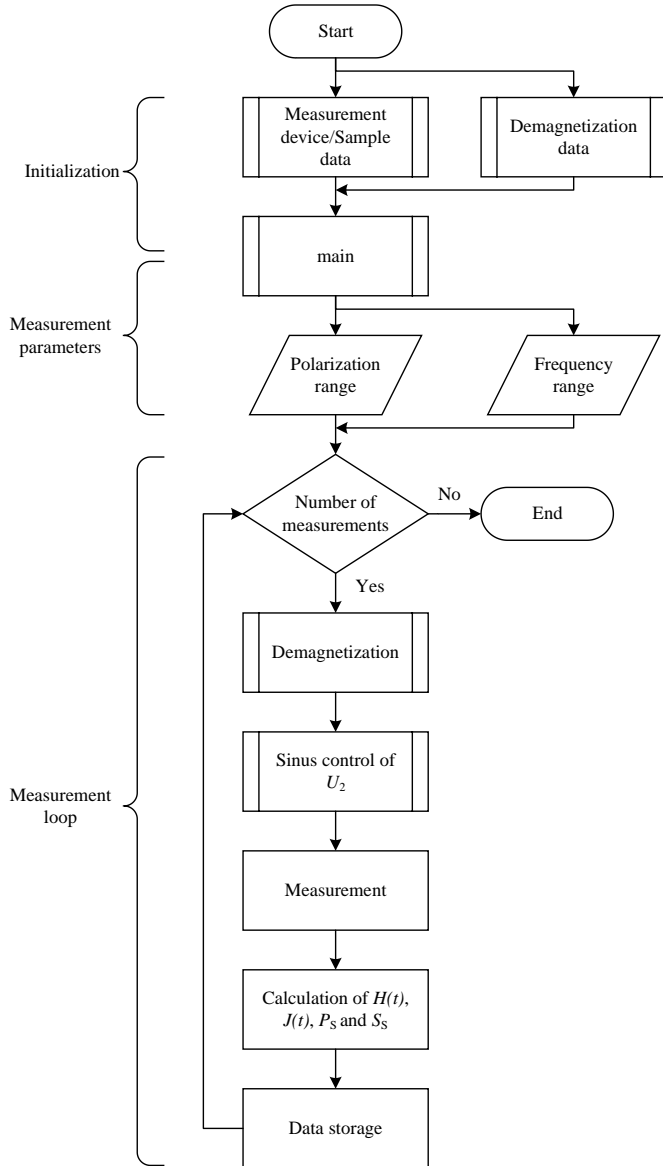


**Fig. 3.3:** Program flowchart

Fig. 3.4 explains the digital control system of the sinusoidal secondary voltage.

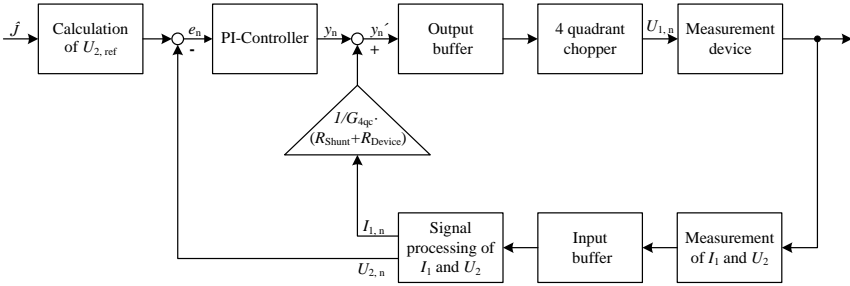


**Fig. 3.4:** Control algorithm of sinusoidal secondary voltage

The reference secondary voltage  $U_{2, \text{ref}}$  is calculated using equation (3.2) for each desired polarization amplitude  $\hat{j}$ . The controller processes one period of the secondary voltage per cycle. In the beginning, a start polarization amplitude of 0.1 T is applied to the measurement device.  $U_{2, \text{ref}}$  is then compared to its measured signal  $U_{2, n}$  leading to the control difference  $e_n$  which is the input of the PI-controller. It relies on an integration algorithm with a trapezoid approximation preventing sudden changes in of the controller output variable  $y_n$  [12, pp. 547-575]. Equation (3.4) gives its transfer function. The index  $n$  denotes the actual cycle whereas  $n-1$  stands for the previous cycle.

$$y_n = y_{n-1} + K_P (e_n - e_{n-1}) + \frac{K_P T_C}{T_1} \frac{(e_n + e_{n-1})}{2} \quad (3.4)$$

Proportional action coefficient  $K_P$ , reset time  $T_1$  and controller cycle time  $T_C$  must be adjusted for each measurement device separately and manually. Sometimes a readjustment depending on the investigated steel sheet samples is necessary because their characteristics have a major impact on the control system behavior. Controller tuning as developed by Takahashi [12, p. 574] is not practical here. The controller output variable  $y_n$  is increased by the voltage drop across shunt resistor  $R_{\text{shunt}}$  and input resistance of the measurement device  $R_{\text{Device}}$ . A division by the four-quadrant chopper gain  $G_{4qc}$  is also part of this feedback path. This voltage drop across both resistors is the main reason for a harmonic distortion of the secondary voltage. It is considered as disturbance variable here, leading to fewer cycles in the control loop and accelerating the control system. The improved controller output variable  $y_n'$  passes the output buffer and is amplified by the four-quadrant chopper which delivers the necessary power and generates the primary voltage for each measurement device. The primary current and secondary voltage are gauged and written into the input buffer of the data acquisition and generation unit. As part of the

signal processing, the average period in primary current and secondary voltage across all measured periods are calculated. Furthermore, the zero crossing followed by a maximum in the voltage signal is detected. With the help of a curve fit, the voltage and the current signal are shifted to the detected point as signal starting position, which is necessary to avoid a phase shift between the reference and the measured voltage. Before the control algorithm processes both signals, they must be filtered to reduce the impact of signal noise. A digital filter fulfills this purpose. It is integrated into the control loop and is not allowed to increase the cycle time. Otherwise, the entire control system is slowed down. The easiest approach would be a moving average filter which is a good solution in time domain. However, this kind of filter creates a substantial reduction of bandwidth which is not practical in magnetic saturation where the content of harmonics in primary current increases [13, p. 280]. The alternative is a filter in the frequency domain. A Fourier expansion of the current and voltage signal is calculated which delivers the DC component, the fundamental and the harmonics of each signal. The signals in time domain are inversely calculated with their fundamental and harmonics up to the 60<sup>th</sup> order which is sufficient according to [72], which mentions a minimum of 41 orders. Only odd order harmonics are part of the original signals due to their point symmetry and therefore, even order harmonics are neglected in the inverse calculation of the filtered signals. This kind of filtering can easily be implemented into the control loop and does not prolong the cycle time significantly.

The USB communication (between measurement unit and PC) plus the control operation produce a cycle time of the control system  $T_C$  of approximately 0.5 s. During that time the control system processes one signal period between 3.33 ms (300 Hz) and 20 ms (50 Hz). A real-time behavior of the controller is not possible. A buffer management for input and output signals solves this problem. At the beginning of each control cycle, the input buffer records primary current and secondary voltage. The control system works with this data during the next cycle. The improved controller output variable  $y_n$  is then written in the output buffer for several periods to create a signal duration that equals at least the controller cycle time. The prolonged signal in the output buffer guarantees a continuous primary voltage at the measurement device. The buffer management assures a synchronous comparison of the reference and the measured secondary voltage  $U_2$ .

A real-time control system is not necessary for this kind of application. Although the controller cycle time is rather long with 0.5 s, the controller accomplishes a sinusoidal secondary voltage in less than one minute, even for high flux density values. The used control system is cheaper and easier to realize than a real time controller. A real-time system cannot work on a Windows based PC due to its non-deterministic behavior and instead, complex microcontroller platforms would be necessary.

The controller loop stops when the desired polarization amplitude and a sinusoidal secondary voltage are reached within defined limits. The form factor ( $FF$ ) describes the relationship of the secondary voltage and an ideal sine waveform. The ratio of voltage RMS value and average absolute value defines it (3.5).

$$FF = \frac{\sqrt{\frac{1}{T} \int_0^T (u_2(t))^2 dt}}{\frac{1}{T} \int_0^T |u_2(t)| dt} \quad (3.5)$$

According to the standards [70, 72] an  $FF$  for the secondary voltage of 1.11 with an allowed variation of  $\pm 1\%$  must be fulfilled. However, the  $FF$  is not an appropriate criterion to determine the distortion of the secondary voltage. Fig. 3.5 illustrates two measurements of the secondary voltage recorded for high magnetic saturation. In the red curve, the voltage distortion is clearly visible although the deviation to the form factor is below  $0.1\%$ . The blue voltage curve shows a contradicting behavior with a deviation in  $FF$  of  $0.2\%$ , although the voltage distortion is obviously smaller in the blue voltage curve than in the red voltage curve.

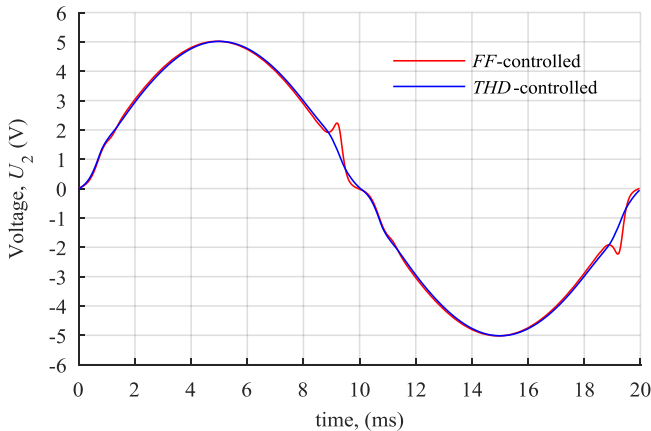


**Fig. 3.5:** Comparison of secondary voltages during a single sheet tester measurement (compare section 3.2.2) at 1.95 T with control criterion form factor ( $FF$ ) and total harmonic distortion ( $THD$ )

Hence, the total harmonic distortion (*THD*) is chosen to describe the content of harmonics in the secondary voltage [65]:

$$THD = \sqrt{\sum_{h=2}^{h_{\max}} \left( \frac{U_h}{U_1} \right)^2}. \quad (3.6)$$

The voltage's fundamental component is symbolized by  $U_1$  whereas  $U_h$  denotes the harmonic component of the order  $h$  and  $h_{\max}$  gives the maximum number of orders. In Fig. 3.5, the red voltage signal delivers a *THD* of about 5 % whereas the blue record shows a *THD* value of less than 2 %. Thus, the *THD* is a very feasible criterion for this purpose and it is limited to less than 1 % for all measurements.

After the controller generates an appropriate primary voltage, it is applied to the measurement device for a certain number of periods. Usually, 110 periods are chosen including 100 measurement and ten extra periods. Again the average period of primary current and secondary voltage are calculated, whereas the first ten additional periods are neglected to assure steady-state conditions. Based on voltage and current signal the magnetic field  $H(t)$  and the magnetic polarization  $J(t)$  are computed (see equation (3.1) and (3.2)). Equation (3.7) and (3.8) calculate further magnetic properties such as the specific total loss  $P_s$  and the specific apparent power  $S_s$  [70, 72].

$$P_s = \frac{1}{m_a} \frac{1}{N_s} \sum_{N_s}^{j=1} i_{1j} \cdot u_{2j} \quad (3.7)$$

$$S_s = \frac{1}{m_a} \frac{1}{N_s} \sqrt{\sum_{N_s}^{j=1} i_{1j}^2} \sqrt{\sum_{N_s}^{j=1} u_{2j}^2} \quad (3.8)$$

A signal period is recorded for  $N_s$  samples, whereas  $j$  represents the sample index. Both properties give a ratio of active or apparent power and the active mass  $m_a$  of the investigated steel sheet sample. The determination of the active mass  $m_a$  is related to the used measurement device and therefore explained in equation (3.9) and (3.11). The number of samples per period  $N_s$  is chosen to be 600 in order to fulfill requirements given by the Nyquist–Shannon sampling theorem explained in the applied standard [72].

The transfer ratio of both analog input channels must be determined correctly. A Single Sheet Tester as described in 3.2.2 is attached to the measurement setup and gauges the magnetic properties of a C165-35 steel sample. The voltage divider and the shunt resistor influence the transfer ratios of the corresponding analog input channel. Hence, a parallel

measurement of primary current and secondary voltage is performed with a high precision power meter (LMG 500, accuracy: 0.015 % of measured value + 0.01 % of measurement range [10]). The RMS values of both signals, calculated by the software and the power meter, are compared, and the transfer ratio is computed. After the transfer ratios are implemented in the software, the active power is recorded by the power meter and the measurement setup from minor to major polarization values. The difference between measurement configuration and power meter never exceeded 0.2 %. Appendix A.3 explains the transfer ratio determination and the calibration procedure.

## 3.2 Established measurement devices

During the last century, many different methods and a broad range of various apparatus to measure the magnetic properties of electrical steel were developed. Because it is necessary to compare electrical steel characteristics of different grades and manufacturers with a known reproducibility [44, pp. 93-94], two different measurement methods were standardized: Epstein frame (EPF) and single sheet tester (SST). Both devices are designed for the investigation of grain-orientated and non-grain-orientated electrical steel. Although leading to contradicting measurement results, EPF and SST are used equally according to the latest standards [11, 65, 70, 72]. Despite these two established apparatus, a new device for measuring magnetic properties align with the normal direction of the magnetic flux density is introduced in chapter 5.

### 3.2.1 Epstein frame

The EPF is the earlier development of the two established devices, and its usage was rather common among electrical steel manufacturers, but due to the extensive sample preparation, it is more and more replaced by the SST [11]. Fig. 3.6 illustrates its setup. Steel sheet stripes are stacked inside coils for excitation and measurement to form the magnetic circuit of a transformer without load. Each stripe must have a length between 280 mm and 320 mm with a maximum difference of  $\pm 0.5$  mm. While investigating grain-orientated electrical steel, the samples must be cut parallel to this orientation in a deviation of  $\pm 1^\circ$ . Non-grain-orientated steel stripes are cut parallel and orthogonal to the rolling direction, where a deviation of  $\pm 5^\circ$  is allowed. The two different kind of samples are stacked alternating, but stripes inside two parallel coil pairs must follow the same order. The width of the steel sheet stripes is defined to be 30 mm including a tolerance of 0.2 mm. The corner areas where the samples overlap must have a quadratic shape with a side length equal to the stripe's width. A force of 1 N is applied to these corner areas to reduce air gaps between the steel stripes. A cutting method producing a negligible burr

along the edge of the samples is required. The number of stripes must be a multiple of four. The total sample mass  $m$  is determined with a deviation of 0.1 %. Four measurement (secondary) and four excitation (primary) coils connected in series surround the sample. In the used EPF the whole number of turns in primary and secondary winding are 700. Equation (3.1) and (3.2) calculate magnetic field and polarization with primary current and secondary voltage. The magnetic path length  $l_{Fe}$  is defined to be 940 mm by [72]. It is a result of the overlapping steel stripes in the corners of EPF (Fig. 3.7). This overlap also affects the active mass of the steel sheet stripes  $m_a$  with a lower limit of 240 g at a stripe's length  $l$  of 280 mm (3.9). The active mass is required to compute specific total loss  $P_s$  and the specific apparent power  $S_s$  (see section 3.1.2).

$$m_a = m \frac{l_{Fe}}{4 \cdot l} \quad (3.9)$$

Based on the entire mass of the sample  $m$ , the sample cross section  $A_{Fe}$  is determined (3.10), where  $\rho$  denotes the density of electrical steel.

$$A_{Fe} = \frac{m}{4 \cdot l \cdot \rho} \quad (3.10)$$

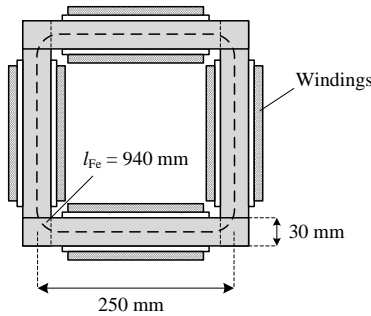


**Fig. 3.6:** 250 mm Epstein frame

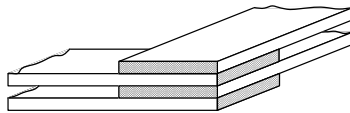


**Fig. 3.7:** Sample overlap in Epstein frame

There is a magnetic coupling between primary and secondary coils in the EPF as a result of air flux which is responsible for measurement errors. A mutual inductance works as a so-called air flux compensation. It consists of two coils wound in different directions and magnetically coupled through air. One coil is serially connected to the primary winding of the EPF, whereas the other one is attached to the secondary winding in the same way. The number of turns in the coils is adjusted while there are no steel sheet stripes present in the EPF until the influence of air flux is negligible [14].

### 3.2.2 Single sheet tester

The SST is designed for a single steel sample as its name says. The steel sheet sample completes the magnetic circuit between an upper and a lower yoke. An excitation (primary) and a measurement (secondary) winding surround the sample (Fig. 3.8). The construction of the SST and whether a single yoke is sufficient is discussed in [17].

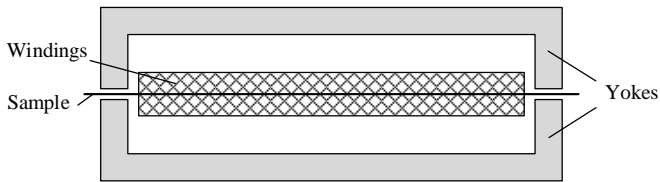


**Fig. 3.8:** Setup of the single sheet tester

The U-shaped yokes can be made of a wound iron core cut in two equally sized halves. Insulated grain-orientated steel with low magnetic resistance and specific total losses not exceeding 1.0 W/kg at a polarization amplitude of 1.5 T and a frequency of 50 Hz is used to build the yokes. This yoke setup reduces eddy currents and assures a homogeneous flux distribution inside them. The geometric dimensions are sketched in Fig. 3.9.

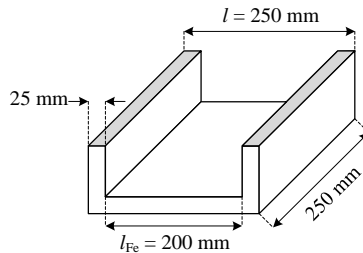


**Fig. 3.9:** Geometric dimensions of a yoke in the SST

A sample size of 250 mm x 250 mm is chosen which is more practical than the 500 mm side length suggested by [70]. This change in dimensions is covered by the standard [70] because the manufacturer of the SST guarantees the comparability of both SST sizes. The magnetic path length  $l_{Fe}$  equals the inner distance between the cross sections of the yokes, which means 200 mm in this case (see Fig. 3.9). The difference in sample length  $l$  and magnetic path length  $l_{Fe}$  leads to the active mass of the steel sheet sample  $m_a$  which is needed to compute specific total loss  $P_s$  and the specific apparent power  $S_s$  (compare equations (3.7) and (3.8)):

$$m_a = m \frac{l_{Fe}}{l} \quad (3.11)$$

Similar to the EPF, the sample cross section  $A_{Fe}$  depends on the entire mass of the sample  $m$  and its density  $\rho$  (3.12):

$$A_{Fe} = \frac{m}{l \cdot \rho} \quad (3.12)$$

However, as stated in [15, 18], the magnetic path length is not constant and depends on the permeability of the investigated sample and the magnetic potential drop in the air gaps between yokes and sample. As a result, the magnetic field determination with equation (3.1) leads to errors in case of a sample with high permeability and wider air gaps. In contrast to the magnetic field, the measurement of specific total loss and specific apparent power is not affected by the change in the magnetic path length. Thus, the air gap between lower and upper yoke is not allowed to be more than 5  $\mu\text{m}$ . A lifting device allowing an easy exchange of samples in the SST partly compensates the upper yoke's force of inertia. The final force must be between 100 N and 200 N.

The quadratic shape of the sample allows the measurement parallel and orthogonal to the rolling direction. The yoke cross section must have a width of 25 mm +/-1 mm, and the overlap of both yokes must be within a deviation of 0.5 mm. The large yoke cross section in comparison to the sample cross section decreases the polarization amplitude in the yokes and therefore their impact on the measurements.

In the used SST, the primary and secondary winding have 150 turns each. The minimum length of the investigated steel sheet sample is 250 mm, but must not be longer than for easy handling of the sample necessary. The width of the sample must at least cover 60 % of the yoke's width. Similar to the stripes of the EPF, the SST sample is cut parallel to the rolling direction with a deviation of 1° for grain-orientated and 5° for non-grain-orientated electrical steel. The requirements for mass measurement and cutting method of the sample

equal those of the EPF. The air flux compensation is built and adjusted in the same way as for the EPF.

EPF and SST are both correct measurement devices, but their measurement results are different [11]. The EPF shows 3 to 8 % less specific total losses, whereas the SST gauges 2 % too high  $P_s$  values for grain-orientated steel in a range of 1.5 T to 1.7 T. The different results in specific total loss measurements affect the determination of the core loss building factor in transformers [11]. The building factor is the relation of SST or EPF  $P_s$  data for a particular electrical steel grade and its magnetic behavior in an electrical machine [14] (compare subsection 4.1). It is used to estimate core losses of electrical machines during design stage. Thus, EPF and SST measurement results cannot be exchanged because doing so increases the uncertainty in core loss prediction.

As a summary, the SST has the advantage of an easy sample preparation and handling. The cutting of steel sheet stripes for the EPF and in the case of grain-orientated material the necessary stress relief annealing are very time consuming [11]. If annealing is applied, the magnetic properties of the electrical steel can vary to those before cutting. The reason is the bending of electrical steel to wound a coil for transportation. This kind of tension and stress which could have a substantial impact on the magnetic properties, vanish during annealing and therefore the magnetic properties improve [16]. Furthermore, the flux distribution in the EPF sample is not uniform, especially in the corners of the EPF. Corner effects contribute to the uncertainty of the magnetic path length determination [63]. A comparison of EPF and SST measurement results delivers a statistical rather than a deterministic relationship [5], and a calibration of the SST with EPF values is not performed [70]. Although the SST has its disadvantage concerning the magnetic path length as previously explained, it is the more practical measurement device in comparison to the EPF, and therefore the SST is the measurement device of choice in this work.



# 4 Modeling and characterization of magnetic properties

AC properties of electrical steel define its quality in means of economic considerations. Especially the magnetic loss characteristic is of great importance due to its impact on the efficiency of all electrical and electromechanical energy transformations. There are two main parameters to describe magnetic properties of electrical steel: the specific magnetic power losses and the  $B(H)$  characteristic which denotes a relationship of magnetic field  $H$  and flux density  $B$ . They are used to grade the electrical steel's quality. This chapter explains the specific magnetic power losses and introduces a hysteresis model which is the mathematical basis to determine  $B(H)$  characteristics [11, 44, pp. 8-12].

## 4.1 Specific total loss and specific apparent power

The calculation of specific total loss and specific apparent power are explicated previously in subsection 3.1.2. Especially the specific total loss is used to describe the quality of electrical steel. Different steel grades are categorized using specific total loss as outlined in the standards [67, 69]. The shortcut for standardized steel qualities is created as follows:

- The letter “M” for electrical steel
- The specific total loss value in  $W/kg$  at a polarization of 1.7 T and a frequency of 50 Hz multiplied with one hundred
- The rated thickness of the sheet in  $mm$  multiplied with one hundred
- The code letter:
  - “S” for conventional grain-orientated electrical steel
  - “P” for grain-orientated electrical steel with high permeability

Manufacturers of electrical steel employ an own nomenclature for their products. Considering the electrical steel grade named C165-35 (Manufacturer: ThyssenKrupp) as an example, the number 165 stands for 1.65 W/kg at a polarization of 1.7 T and a frequency of 50 Hz. The last two digits of the name (35) denote the thickness of the electrical steel, 350  $\mu m$  in this case. However, the naming of steel grades depends on the manufacturer and is not defined by a standard. In the electrical steel 23ZH85 (Manufacturer: Nippon Steel), the nomenclature is upside down to the previous steel mentioned. The first number is related to the steel sheet's thickness (23: 230  $\mu m$ ), and the last number gives the selected

specific loss value (85: 0.85 W/kg). Fig. 4.1 demonstrates a  $P_S$ -curve and  $S_S$ -curve for the steel grades C165-35 and 23ZH85 obtained by SST measurements. The 23ZH85 quality is a high-performance electrical steel indicated by low losses while the low-cost material C165-35 shows a high loss consumption in comparison. The two different steel qualities are chosen as examples to cover the variety of electrical steel qualities.

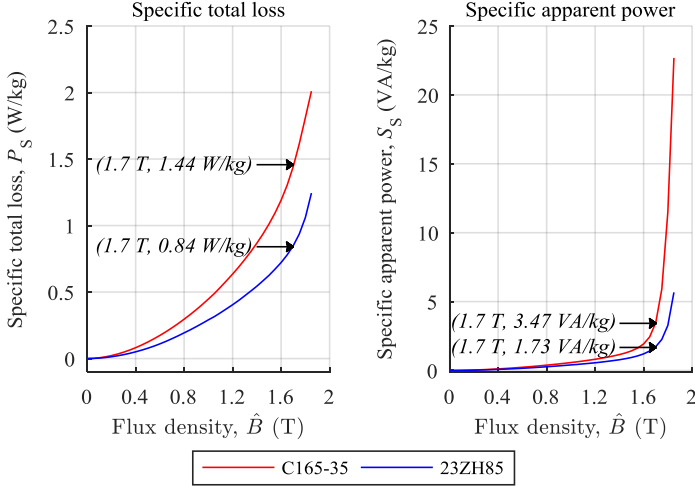


**Fig. 4.1:**  $P_S$ -curve and  $S_S$ -curve for the steel grades C165-35 and 23ZH85 obtained by SST measurements

The specific total loss of an electrical steel grade is important for manufacturers of electrical machines such as power transformers. The no-load losses of power transformers equal the core losses [48, section 1-6], and they scale life cycle costs of transformers (subsection 7.1.4). The core losses rely on the used electrical steel quality. They are an important criterion for the customer. If the planned maximum value of core losses is exceeded even by few percent, a penalty is usual. Thus, a determination of core losses as accurate as possible during design stage of the power transformer is of interest. The losses of the core  $P_{Core}$  can be approximated with core mass  $m_{Core}$ , the applied flux density  $\hat{B}$  and the specific total loss  $P_S$ :

$$P_{Core} = m_{Core} \cdot P_S(\hat{B}). \quad (4.1)$$

However, this loss estimation is rather poor, and a correction factor, the so-called building factor is introduced. It gives the relation between the results of equation (4.1) and the

measured power consumption of the transformer without load (compare subsection 6.3.1). The building factor is based on experience achieved while producing the same or at least comparable transformer types. A continuous adjustment is mandatory due to changes in steel quality.

The specific total loss at a polarization amplitude of 1.7 T and a frequency of 50 Hz defines the steel quality. This value is an upper limit; the real specific total loss is usually lower as shown in Fig. 4.1. Furthermore, the magnetic behavior for other polarizations is not standardized and varies from manufacturer to manufacturer. Fig. 4.2 demonstrates specific total loss curves for a steel grade M165-35 and it also indicates the specific loss value based on the steel name.

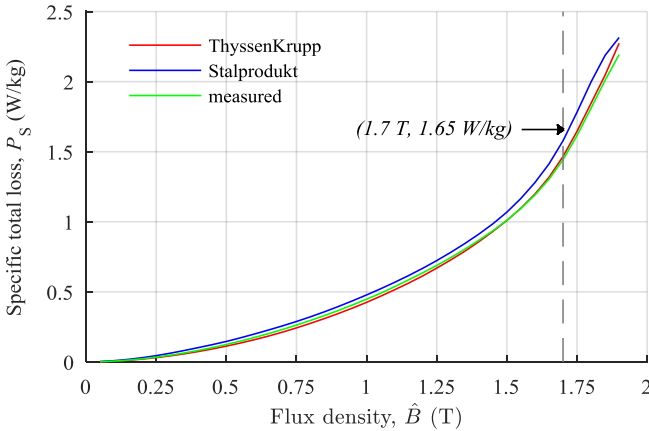


**Fig. 4.2:**  $P_S$ -curves from ThyssenKrupp, Stalprodukt and own measurements

The data are derived from ThyssenKrupp and Stalprodukt as well as from own measurements performed with an SST. ThyssenKrupp and own measured data are based on the same steel grade C165-35. The differences between own measurements and the producer data are evident. The relative deviation in Fig. 4.3 between manufacturer datasets and own measurements is more distinctive for smaller flux densities, while the deviation of the Stalprodukt  $P_S$ -curve is higher than the one from ThyssenKrupp. This comparison shows that on the one hand, steel grades produced by different manufacturers could have significantly different magnetic properties and on the other hand, magnetic characteristics of electrical steel made by one manufacturer and belonging to one certain quality depend on each production batch [4]. These deviations are a challenge for modeling and simulation of magnetic properties in electromagnetic devices when only a small sample is available

to describe the magnetic properties. It becomes clear that an exchange of a steel manufacturer has a major impact on the behavior of the assembled device even if the steel grades belong to the same standardized category. To reduce errors in modeling magnetic properties, several samples of the used electrical steel are recommended to determine average magnetic characteristics.

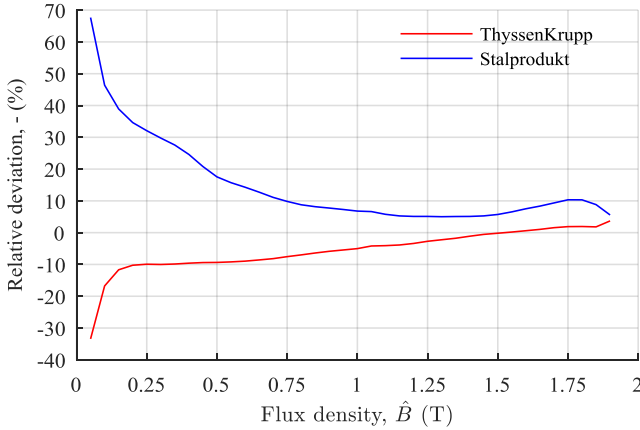


**Fig. 4.3:** Relative deviation in  $P_s$ -curves between own measurements, ThyssenKrupp and Stalprodukt data

## 4.2 Hysteresis model based on harmonics in the magnetic field

Up to now, there have been several hysteresis models for grain- and non-grain-orientated steel sheets, such as the generalized Chua- [2] or the Saito-model [3]. They rely on a Fourier expansion of the magnetic field intensity. A mathematical description for polarization and cosine components of the magnetic field and one for the derivation of polarization and sine components of the field are developed [8]. However, it is still difficult to find appropriate model parameters to acquire a sound reproduction of measured hysteresis curves especially in magnetic saturation. This chapter explains a new hysteresis model for electrical steel based on a Fourier analysis of the magnetic field. This model approach relies on a series of measured hysteresis curves from minor to major loops for each inves-

tigated steel sheet sample. The two different electrical steel grades introduced in subchapter 4.1, are selected for modeling to cover a broad range of electrical steel qualities. The steel grade C165-35 produced by ThyssenKrupp is low-cost steel. Nippon Steel manufactures the high-quality steel 23ZH85. The model algorithm is only given with 23ZH85 steel data for convenience, but concerning model accuracy both mentioned steel grades are reflected. All measurements are performed with the measurement setup explained in subsection 3.1 including the SST.

A mathematic description of a magnetic hysteresis curve is rather difficult. There are two polarization values for each magnetic field value; their mathematical relation is not unique as explained by Fig. 4.4.

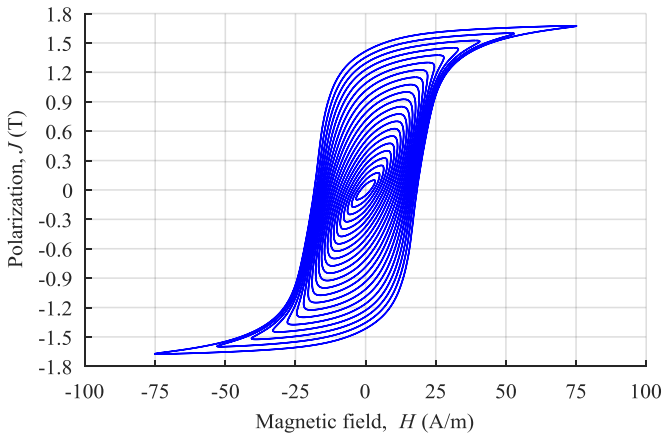


**Fig. 4.4:** Measured hysteresis loops for the steel 23ZH85 manufactured by Nippon Steel

A way to find a definite relation is to switch from time to frequency domain; a Fourier expansion of the magnetic field is necessary. Analysis and calculations are performed with the numerical analysis software MATLAB. The investigated data consist of hysteresis loops which are gauged with a polarization controlled to be sinusoidal. All harmonics are part of the magnetic field due to the non-linear relationship of field and polarization. Fig. 4.5 demonstrates the absolute spectrum of the magnetic field. Only harmonics with odd multiples of the fundamental frequency occur. The magnetic field does not contain a direct component. This spectrum does not provide any information about the phase between each harmonic of the field and the polarization amplitude. It shows the dependency of the absolute field components (fundamental and harmonics) and the polarization.

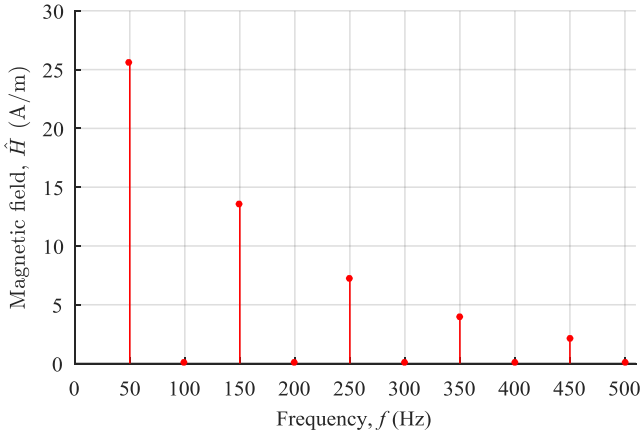


**Fig. 4.5:** Spectrum of magnetic field at a polarization  $\hat{J}$  of 1.7 T

While separating fundamental and harmonics in the magnetic field into sine and cosine waves, the phase angle to the corresponding polarization amplitude is still known. Fig. 4.6 explains the relationship of cosine ( $a_1$ ) and sine ( $b_1$ ) components belonging to the fundamental of the field versus the polarization amplitude.

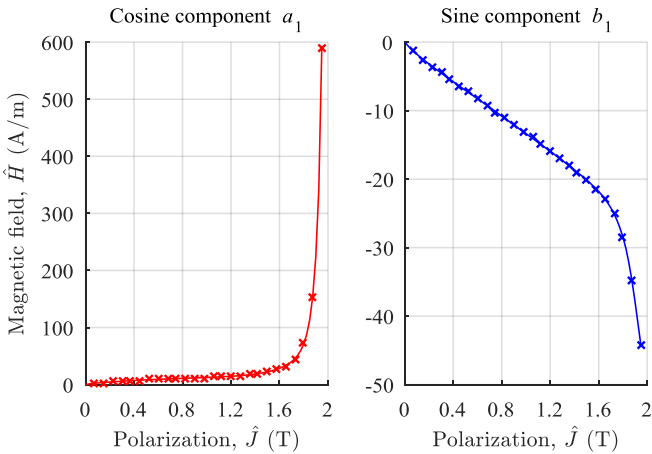


**Fig. 4.6:** Cosine ( $a_1$ ) and sine ( $b_1$ ) component of the fundamental of the magnetic field

With a linear interpolation of the cosine and sine components, the fundamental of the field in time domain is calculated as a function of the polarization's amplitude  $\hat{J}$  (4.2). The variables  $f$  and  $t$  denote frequency and time, respectively.

$$H_1(t, \hat{J}) = \begin{bmatrix} a_1(\hat{J}) \cdot \cos(2\pi f \cdot t) \\ + \\ b_1(\hat{J}) \cdot \sin(2\pi f \cdot t) \end{bmatrix} \quad (4.2)$$

The magnetic field does not only consist of its fundamental, but odd order harmonics are also part of it. For each harmonic, a similar relationship as in the fundamental of the magnetic field can be found. Fig. 4.7 shows the relationship of cosine and sine elements versus polarization amplitude for the third, fifth and seventh order.

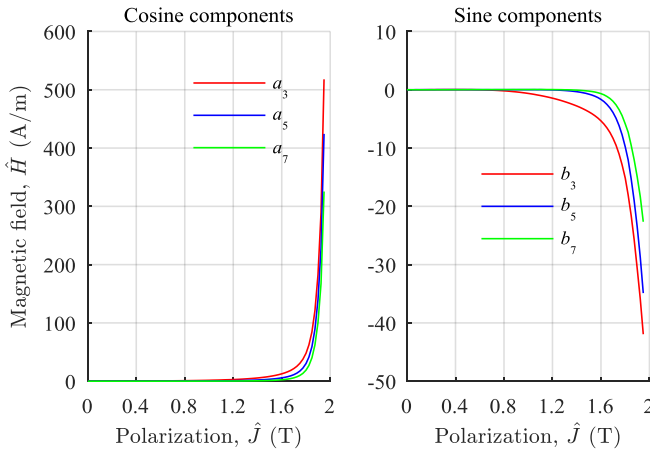


**Fig. 4.7:** Cosine ( $a_{3; 5; 7}$ ) and sine ( $b_{3; 5; 7}$ ) components of the 3<sup>rd</sup>, 5<sup>th</sup> and 7<sup>th</sup> order harmonic in the magnetic field

Again the components for each harmonic are linearly interpolated. Now, the components are known for arbitrary polarization amplitudes  $\hat{J}$ . The complete time dependent signal of the magnetic field is a summation of its fundamental and its harmonics:

$$H(t, \hat{J}) = \sum_{h=1}^{60} \left[ \begin{array}{l} a_h(\hat{J}) \cdot \cos(2\pi fh \cdot t) \\ + \\ b_h(\hat{J}) \cdot \sin(2\pi fh \cdot t) \end{array} \right]. \quad (4.3)$$

A comparison of measured and modeled hysteresis loops confirms that 60 orders ( $h$ ) are necessary for some electrical steels to achieve a good representation of the magnetic field. Equation (4.3) describes the hysteresis model based on the sum of harmonics in the magnetic field which is called hysteresis model from now on.

In a next step, the accuracy of the magnetic field generated by the hysteresis model is analyzed. Additionally, a linear interpolation of measured data in time domain expresses the magnetic field. The relationship of flux density amplitude and magnetic field curve as function of time delivers the basis for this interpolation in time domain. For both approaches, hysteresis model and linear interpolation in time domain, only measured data with even multiples of 0.025 T from 0.05 T to 1.95 T are taken into account. The remaining data with only odd multiples of 0.025 T from 0.075 T to 1.925 T is used for comparison. These data are denoted as measured data in Fig. 4.8, which displays the curves of the magnetic field for 1.925 T as an example.

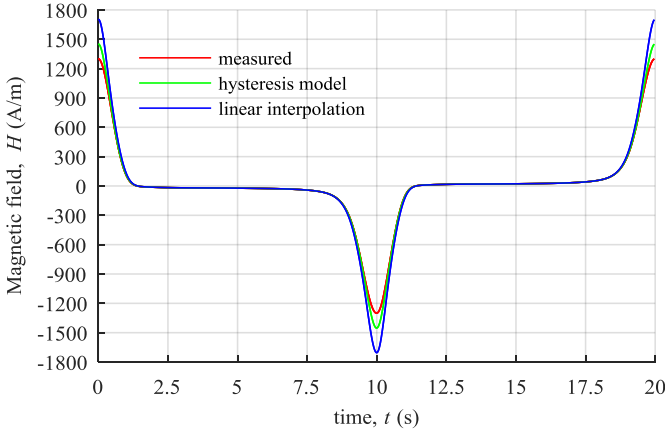


**Fig. 4.8:** Measured magnetic field and the field generated by hysteresis model or linear interpolation at  $\hat{J} = 1.925$  T of steel grade 23ZH85

The relative error based on RMS values of the magnetic field strength is utilized to compare the results of linear interpolation and hysteresis model to the remaining measured

data. Fig. 4.9 illustrates the relative error of the linear interpolation and the hysteresis model as a function of the polarization amplitude for steel grades 23ZH85 and C165-30. Both approaches have an error value smaller than 1 % between 0.175 T and 1.425 T, but above 1.425 T the hysteresis model delivers better results especially when reaching magnetic saturation. The relative error is more important for higher than for small polarization amplitudes because it affects the simulation of core losses in the same polarization range. Power transformers are usually designed for a polarization amplitude of 1.6 T to 1.8 T [48, section 1-5]. The relative error caused by the hysteresis model is significantly smaller in this polarization range compared to the deviation created by the linear interpolation in time domain.

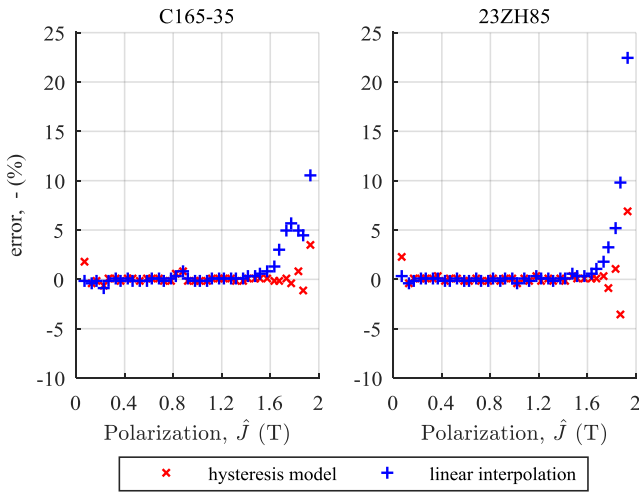


**Fig. 4.9:** Relative error of hysteresis model and linear interpolation

Despite the good agreement of measured and simulated hysteresis loops, there are limitations of the hysteresis model. It is for usage in steady state only. Modeling inrush currents of a transformer is not possible, for instance. The investigated relationship of magnetic field and polarization depends on a sinusoidal waveform of the polarization. Otherwise, the distribution of harmonics in the corresponding magnetic field would be different, and the model described by equation (4.3) is not valid.

A new hysteresis model for electrical steel sheets relying on measured data is developed in this chapter. The data analysis is implemented in a MATLAB program which can create a hysteresis model for a variety of different electrical steel grades. In comparison to the

linear interpolation of the magnetic field in time domain, the hysteresis model shows better results, especially for saturating fields. This model approach has already been published in [77]. It is extended to an advanced hysteresis model in [79] describing flux density amplitude and frequency dependence.

### 4.3 $B(H)$ characteristics

The relationship of magnetic field  $H$  and magnetic flux density  $B$  in a ferromagnetic material is usually nonlinear. The ratio of  $B$  and  $H$  defines the permeability  $\mu$ . It relies on the applied magnetic field strength and therefore a fixed permeability value describes only the actual point of operation. The permeability as a function of the magnetic field is not feasible to characterize ferromagnetic properties. A magnetization curve representing the dependence of magnetic flux density and magnetic field is a more useful expression of ferromagnetic properties in technical applications [44, p. 9].

There are several approaches to determine magnetization curves from measured hysteresis loops. The most common method to reduce information of an entire range from minor to major hysteresis loops to one single curve is the construction of a BH-curve. The maximum values for magnetic field and flux density are selected in each measured hysteresis loop. All these points are connected starting at the point of origin [44, p. 12]. This kind of magnetization curve is called *maximum* BH-curve from now on (compare Fig. 4.10 and Fig. 4.11). Both maxima (magnetic field and flux density) do not occur simultaneously and therefore, the point defined by the maximum values is not part of the corresponding hysteresis loop.

The hysteresis model introduced in section 4.2 is employed to calculate the values of the maximum magnetic field and polarization values (4.4).

$$\hat{H}(\hat{J}) = \max \left( \sum_{h=1}^{60} \begin{bmatrix} a_h(\hat{J}) \cdot \cos(2\pi f h \cdot t) \\ b_h(\hat{J}) \cdot \sin(2\pi f h \cdot t) \end{bmatrix} \right) \quad (4.4)$$

After that, equation (4.5) computes the flux density amplitude  $\hat{B}$  with  $\hat{H}$  and  $\hat{J}$ .

$$\hat{B} = \hat{J} + \mu_0 \hat{H} \quad (4.5)$$

Another way to achieve a magnetization curve from measured data is a selection of the maximum polarization value  $\hat{J}$  and the time corresponding magnetic field value  $H(\hat{J})$ . Again the hysteresis model computes the value pairs of polarization and magnetic field:

$$\begin{aligned}
 H_L(\hat{J}, t=0) &= \sum_{h=1}^{60} \left[ \begin{aligned} &a_h(\hat{J}) \cdot \cos(2\pi fh \cdot t) \\ &+ \\ &b_h(\hat{J}) \cdot \sin(2\pi fh \cdot t) \end{aligned} \right] \\
 &= \sum_{h=1}^{60} [a_h(\hat{J})] .
 \end{aligned} \tag{4.6}$$

The hysteresis model represents the time-dependent magnetic field  $H(t)$  as the sum of cosine and sine waves while the polarization  $J(t)$  is cosinusoidal without any harmonics. The polarization reaches its maximum at  $t=0$ , where all sinusoidal components in the magnetic field are zero. Thus, the desired magnetic field value is the addition of cosine elements in the magnetic field only. Similar to the *maximum* BH-curve, the flux density is calculated with the polarization and magnetic field value in equation (4.5). The second kind of magnetization curve is named *inductive* BH-curve. Only inductive components of the magnetic field are part of this magnetization curve. The flux density  $B(t)$  relies on the secondary voltage  $U_2(t)$  measured with the SST due to Faraday's law (compare section 3.1.1). When the flux density  $B(t)$  is at its maximum the secondary voltage  $U_2(t)$  is zero. Finally, there are no active components in primary current  $I_1(t)$  and magnetic field  $H(t)$  at that time. This *inductive* BH-curve (index "L") is especially useful for the characterization of power transformers when the behavior of its main inductance is of interest.

At last, a third kind of magnetization curve is developed as part of this thesis. In contrast to the *inductive* magnetization curve, the component of the magnetic field's fundamental is considered which is in phase with the secondary voltage. This part of the magnetic field represents active losses in the electrical steel sheet under cosinusoidal excitation. The achieved magnetization curve is called *resistive* BH-curve. The hysteresis model delivers again the desired component of the magnetic field's fundamental ( $h=1$ ) which is in phase to the sinusoidal secondary voltage  $U_2(t)$  reaching its maximum at  $t=T/4$  (4.7).

$$\begin{aligned}
 H_R\left(\hat{J}, t = \frac{T}{4}, h=1\right) &= \sum_{h=1}^{60} \left[ \begin{aligned} &a_h(\hat{J}) \cdot \cos(2\pi fh \cdot t) \\ &+ \\ &b_h(\hat{J}) \cdot \sin(2\pi fh \cdot t) \end{aligned} \right] \\
 &= b_1(\hat{J})
 \end{aligned} \tag{4.7}$$

Equation (4.5) computes the flux density amplitude with the polarization and magnetic field value similar to the previous BH-curve approaches. This *resistive* BH-curve (index “R”) is practical for the investigation of transformer’s no-load losses.

Fig. 4.10 and Fig. 4.11 illustrate all three BH-curves and their relationship to measured hysteresis loops. The phase shift between flux density and magnetic field is neglected. Therefore, a hysteresis is not part of the description of magnetic characteristics. Both figures show only hysteresis curves from 0.05 T to 1.7 T for convenience.

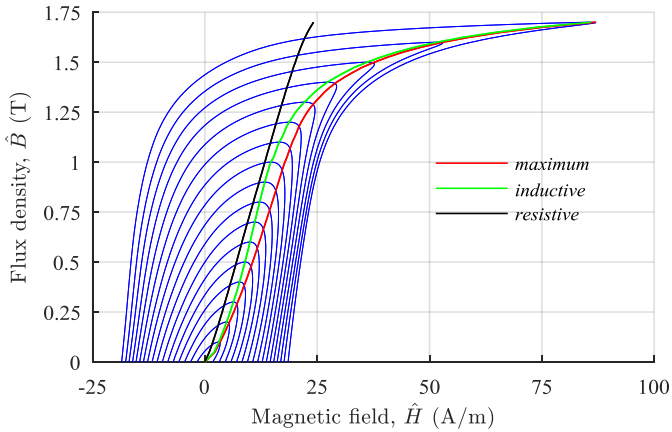


**Fig. 4.10:** Determination of *maximum*, *inductive* and *resistive* BH-curve relying on SST measurements from 0.05 T to 1.7 T with a 23ZH85 steel sheet sample

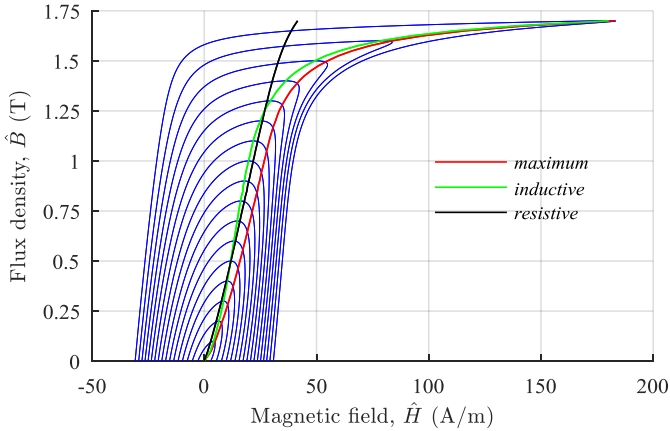


**Fig. 4.11:** Determination of *maximum*, *inductive* and *resistive* BH-curve relying on SST measurements from 0.05 T to 1.7 T with a C165-35 steel sheet sample

The *maximum* and *inductive* BH-curves follow a similar slope while reaching magnetic saturation, whereas the *resistive* BH-curve shows an almost linear behavior.

Based on a BH-curve, the differential permeability  $\mu_{\text{diff}}$  can easily be calculated:

$$\mu_{\text{diff}} = \frac{\Delta B}{\Delta H}. \quad (4.8)$$

The *maximum* BH-curve shows the smallest differential permeability in comparison to *inductive* and *resistive* BH-characteristics for both steel grades. The *resistive* BH-curve follows an almost constant permeability. The differential permeability is used to model magnetic material's properties in Finite Element (FE) software, which requires that magnetization curves must reach magnetic saturation. The differential permeability in saturation equals the absolute permeability  $\mu_0$  between the two last value pairs of flux density and field. The saturation polarization stated in the data sheet of the electrical steel manufacturer  $J_s$  is 2.03 T [64]. Each BH-curve is prolonged with a linear extrapolation to a polarization  $\hat{J}$  of 2.029 T. To fulfill the FE Software requirements of a relative permeability  $\mu_r = 1$  between the two last value pairs of the BH-curve, the saturation polarization of 2.03 T is used to calculate the corresponding magnetic field value. The different BH-curve approaches are compared with an FE model of an SST and a power transformer in chapter 6.

## 4.4 Magnetic anisotropy

Electrical steel is a magnetically anisotropic material, and its properties strongly depend on the direction of the applied flux density. The anisotropy of specific total loss is discussed at first. Its maximum in grain-orientated electrical steel usually occurs at an angle of  $55^\circ$  and not at an angle of  $90^\circ$  with respect to the rolling direction [6, 9, 44, pp. 13-19]. Fig. 4.12 gives  $P_S$ -curves of the steel grade C165-35 for a magnetization angle to rolling direction of  $0^\circ$ ,  $45^\circ$  and  $90^\circ$  as example for the magnetic anisotropy of specific total loss. An angle of  $0^\circ$  to rolling direction is simply termed rolling direction, and an angle of  $90^\circ$  is named trans-rolling direction. Measurements are performed with an SST while the samples are cut at each magnetization angle. The magnetic induction level is limited to 1.5 T in order to avoid saturation which is reached at a lower flux density for angles of  $45^\circ$  and  $90^\circ$  compared to  $0^\circ$ . The anisotropy of specific total losses is substantial and strongly non-linear. The  $P_S$ -curve of  $45^\circ$  is also estimated with an average calculation based on specific total loss gauged in rolling and trans-rolling direction (see the cyan curve in Fig. 4.12). The difference between measured and estimated results is evident and underlines the non-linear behavior of specific total losses as a function of the magnetization angle.

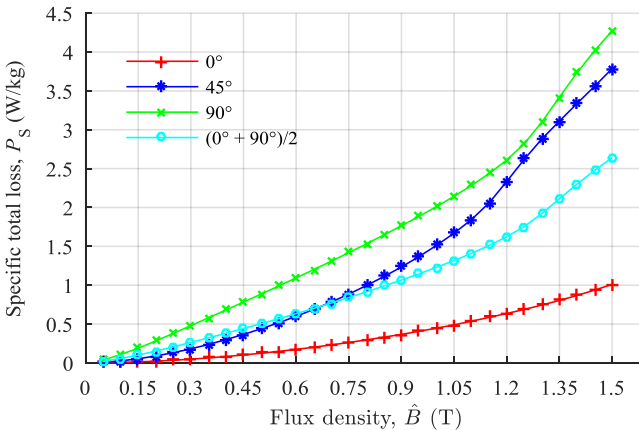


**Fig. 4.12:**  $P_S$ -curves of the steel grade C165-35 with an angle between applied flux density and rolling direction of  $0^\circ$ ,  $45^\circ$ ,  $90^\circ$  and an average calculation of  $0^\circ$  plus  $90^\circ$

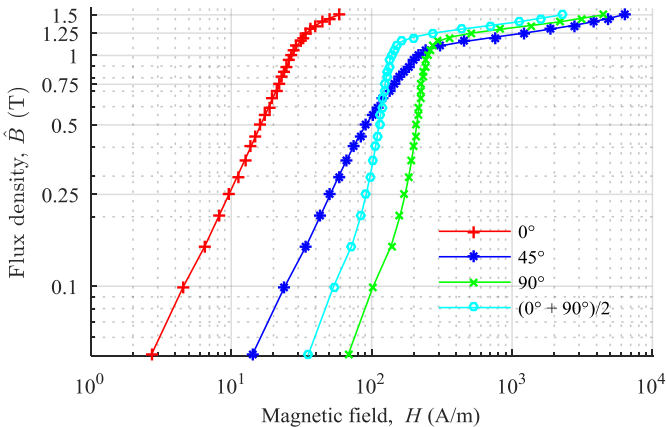
In a second step, the anisotropic behavior of electrical steel is analyzed using the *maximum* BH-curve as an example for all three magnetization curves introduced in this chapter.

Fig. 4.13 displays *maximum* BH-curves of the steel grade C165-35 gauged at a magnetization angle of  $0^\circ$ ,  $45^\circ$  and  $90^\circ$ . Similar to the  $P_S$ -curves in Fig. 4.12, the strong anisotropy is evident. An average BH-curve of  $45^\circ$  is estimated with magnetic field values measured in rolling and trans-rolling direction (see the cyan curve in Fig. 4.13). Additionally, Table 4.1 gives the relative permeability for each measured angle and for the average estimation at a flux density of 1 T.

**Table 4.1:** Relative permeability comparison for different angles

| angle                           | $0^\circ$ | $45^\circ$ | $(90^\circ + 45^\circ)/2$ | $90^\circ$ |
|---------------------------------|-----------|------------|---------------------------|------------|
| $\mu_r (\hat{B} = 1 \text{ T})$ | 29325     | 3704       | 5747                      | 3186       |

The results of Table 4.1 and Fig. 4.13 show significant differences in the relative permeability and the BH-curves for measured and estimated values at an angle of  $45^\circ$  which attest the non-linear behavior of relative permeability and BH-curves as a function of the magnetization angle.



**Fig. 4.13:** *maximum* BH-curves of the steel grade C165-35 with an angle between applied flux density and rolling direction of  $0^\circ$ ,  $45^\circ$ ,  $90^\circ$  and an average calculation of  $0^\circ$  plus  $90^\circ$

The investigation of anisotropy in grain orientated electrical steel with  $P_S$ -curve relative permeability and BH-curve prove that magnetic properties cannot be modeled correctly

with data measured in rolling and trans-rolling direction. Characteristics for various directions should be included in software used to design magnetic devices [44, p. 285]. Apparatus to gauge magnetic properties for arbitrary magnetization angles are discussed in [7, 19]. The FE Software ANSYS Maxwell 2016 is applied in this work. Unfortunately, it is not possible to implement several datasets for different magnetization angles, only properties in rolling and trans-rolling direction can be embedded. Therefore, characteristics in rolling direction are used to describe electromagnetic devices in the software.

# 5 Investigation of flux density orthogonal to the sheet plane

As described in chapter 3, there are two established measuring devices to investigate the characteristics of electrical steel: Epstein frame (EPF) and single sheet tester (SST). EPF and SST have the disadvantage that magnetic properties of electrical steel can only be measured along the sheet plane. Applications and improvements are stated in [11], but measurements along normal direction are not discussed. In literature, a few different approaches are mentioned to gauge magnetic properties perpendicular to the steel sheet plane [29, 31, 32]. Especially the setups in [31] and [32] are rather sophisticated. Small coils integrated into the sheet sample causing a tedious preparation measure the magnetic flux density applied in normal direction [32]. In [31] only DC magnetization is investigated, and magnetic flux density is gauged by a steadily moving coil generating a voltage related to the applied flux density. All found measurement devices have a rather complex setup and provoke a complicated handling. As part of this work, a less sophisticated setup is introduced to quantify the magnetic characteristics of electrical steel in normal direction. The new measurement device is called normal direction tester (NDT) from now on. Its experimental setup was designed and tested in a master thesis [82].

## 5.1 Measurement setup

The NDT consists of an upper and a lower yoke surrounded by a primary and a secondary winding (Fig. 5.1). Steel sheet samples are placed between the yokes and complete the magnetic circuit. A plastic layer above each sample is also part of the setup. Its thickness is known (here:  $d_{\text{plastic}}=35 \mu\text{m}$ ) which is much bigger as assumed deviations in the flatness of the yoke cross sections. The plastic layer compensates possible differences in the air gap between the yokes and creates a homogeneous flux density in the steel sheet samples.

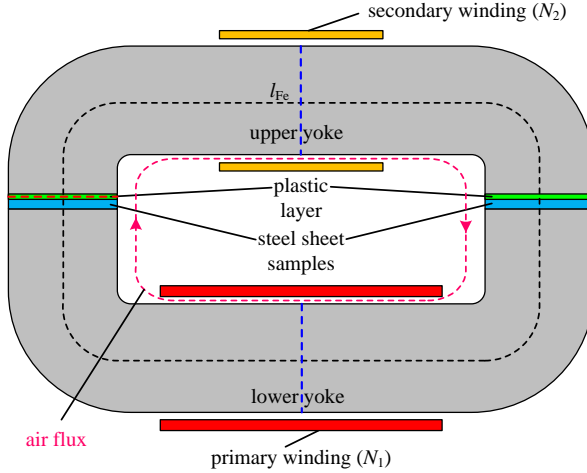


**Fig. 5.1:** Setup of the Normal Direction tester (NDT)

The functionality of the measurement device is similar to those of EPF and SST (see section 3.2). It behaves like a transformer without load. The current  $I_1$  in the primary winding  $N_1$  is related to the magnetic field, and the integral of the voltage  $U_2$  at the secondary winding  $N_2$  is proportional to the magnetic flux density  $B$ :

$$H(t) = I_1(t) \frac{N_1}{l_{\text{Fe}}} \quad (5.1)$$

and

$$B(t) = \frac{1}{N_2 A_{\text{Fe}}} \int U_2(t) dt . \quad (5.2)$$

An upper and a lower yoke with a square cross section  $A_{\text{Fe}}$  of  $0.0016 \text{ m}^2$  and an entire magnetic path length  $l_{\text{Fe}}$  of  $0.487 \text{ m}$  are chosen. A wound core is cut in halves to produce the yokes. The yoke cross sections are treated with hydrochloric acid to remove burrs as a result of cutting, which could cause a galvanic connection between the steel sheet layers of the yokes [70]. These connections would lead to an increase of eddy current losses in the yokes and could have an adverse impact on the homogeneity of the applied flux density. The upper yoke is smaller for a better handling of the NDT during a change of steel sheet samples or plastic layers. Since the geometric dimensions are defined, the number of turns  $N_1$  must be determined. Fig. 5.2 illustrates the electric circuit of the NDT. All elements of this circuit are described analytically and time independently based on the

circuit theory. Steel sheet samples are not part of the circuit for simplicity. Nevertheless, a plastic layer of  $d_{\text{plastic}}=35 \mu\text{m}$  is taken into account. According to [30], normal flux density reaches amplitudes up to 0.3 T in laminated transformer cores. Thus, a maximum flux density of 1 T is chosen to accomplish a safety margin.

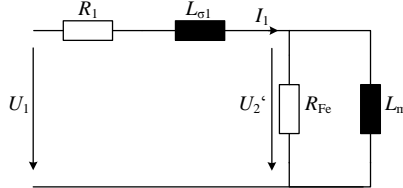


**Fig. 5.2:** Electric circuit of the NDT

The yokes are made of the electrical steel H103-27. The yoke manufacturer provides a sample of the used steel grade. The *inductive* BH-curve and the specific total losses of the electrical steel in the yokes are measured with a SST. A value of 18.5 A/m for the magnetic field  $\hat{H}$  and a specific total loss  $P_S$  of 0.37 W/kg correspond to the chosen flux density  $\hat{B}$  of 1 T. The peak supply voltage  $U_1$  is limited to 10 V.

The parasitic resistance  $R_1$  is the sum of the shunt resistor  $R_{\text{shunt}}$  in the measurement setup (compare chapter 3.1.1:  $R_{\text{shunt}} = 0.5 \Omega$ ) and the copper resistance of the primary winding (5.3). It is computed with the specific resistance of copper  $\rho_{\text{Cu}}$ , the length of the wire  $l_{\text{Cu}}$  and the conductor cross section  $A_{\text{Cu}}$ . The wire length  $l_{\text{Cu}}$  equals the product of the peripheral length of the yoke cross section and the number of turns  $N_1$ . The conductor cross section  $A_{\text{Cu}}$  is chosen to be 3 mm<sup>2</sup> allowing a maximum current of 9 A (RMS) [33].

$$R_1 = R_{\text{shunt}} + \rho_{\text{Cu}} \cdot \frac{l_{\text{Cu}}}{A_{\text{Cu}}} \quad (5.3)$$

A voltage drop across the leakage inductance  $L_{\sigma 1}$  is negligibly small compared to voltage across  $R_1$ . Hence, the leakage inductance is left aside.

Equation (5.4) calculates the equivalent core loss resistance  $R_{Fe}$ , which represents the active power consumption of the yokes. The product of specific losses  $P_S$  and yoke mass  $m_{\text{yoke}}$  delivers the active power quantity.

$$R_{Fe} = \frac{U_2^2}{P_S \cdot m_{\text{yoke}}} \quad (5.4)$$

Equation (5.5) approximates the main inductance  $L_m$ , where the permeability of the used yoke steel is the ratio of chosen magnetic field  $\hat{H}$  and flux density  $\hat{B}$  values.

$$L_m = \frac{A_{Fe} \cdot N_1^2}{\frac{l_{Fe}}{\mu_r} + \frac{2d_{plastic}}{\mu_0}} = \frac{A_{Fe} \cdot N_1^2}{l_{Fe} \frac{\hat{B}}{\hat{H}} + \frac{2d_{plastic}}{\mu_0}} \quad (5.5)$$

Finally, a program realized in the numeric analysis software MATLAB based on the mathematic description of the circuit in Fig. 5.2 iterates the total number of turns in the primary winding  $N_1$ . The number of turns  $N_1$  is increased in steps of 1 until the flux density as a function of  $U_2$  (equation (5.2)) equals the desired value of 1 T. The iteration of  $N_1$  for the NDT results in 20 turns for the primary winding with the NDT design data given above. The same number of turns  $N_2$  are chosen for the secondary winding.

## 5.2 Construction of the NDT

The magnetically active parts of the NDT like the upper and lower yoke equipped with primary and secondary winding are introduced in subchapter 5.1. In this section, the focus is set on the peripheral hardware components of the entire measurement device as shown in Fig. 5.3. The lower and upper yoke are arranged in a fixture made of synthetic resin bonded paper. Metal is not used close to the yokes to avoid a distortion of flux density due to eddy currents. The upper yoke fixture is connected to a sled. A left and a right sliding shaft keeps the sled in position. With the help of a spindle, the upper yoke can be lifted easily to remove or change plastic layers and steel sheet samples. The connection of the upper yoke fixture and the sled is equipped with a pressure relief to assure a reproducible clamping force. This mechanism does not allow a force created by the spindle. Only a force of inertia generated by the mass of the upper yoke and the fixture is possible which equals a constant clamping force of approximately  $3000 \text{ N/m}^2$ . The entire hardware construction allows a precise and reproducible positioning of the upper onto the lower yoke. Furthermore, the user can check the location of plastic layer and steel sheet samples while the upper yoke is standing on the lower one. A negative influence of fringing flux is reduced to a minimum this way (compare subsection 5.3.1).

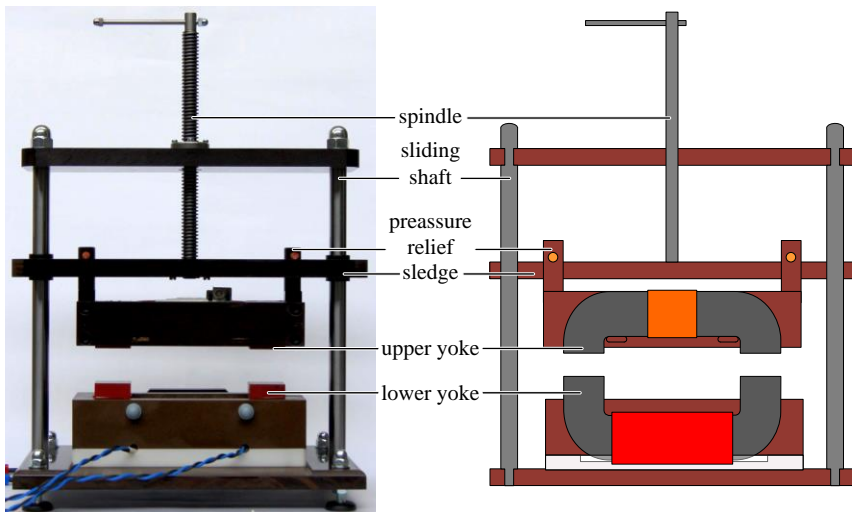


**Fig. 5.3:** Construction of the NDT

## 5.3 Evaluation of the NDT

In this subchapter, the NDT's suitability to gauge magnetic characteristics orthogonal to the sheet plane is analyzed. Parasitic effects are described, and their impacts on the measurements are evaluated with an FE simulation of the NDT.

### 5.3.1 Parasitic effects

The influence of fringing flux, air flux and inhomogeneity of applied flux density on measurements are discussed. At first, the effect of fringing flux is explained as demonstrated in Fig. 5.4.

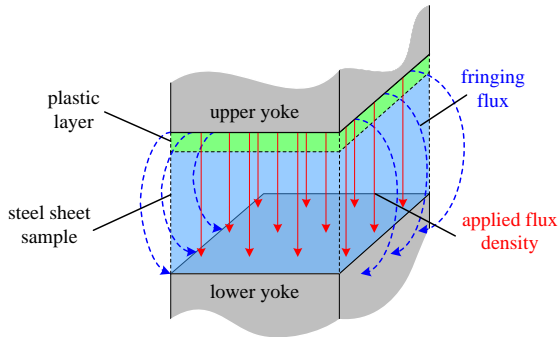


**Fig. 5.4:** Applied flux density and fringing flux in the NDT [31]

Flux bypasses the plastic layer and the steel sample through air and causes an overestimation of the applied flux density, which is determined with the secondary winding (see Fig. 5.1). In order to avoid fringing flux, both yokes must overlap entirely. Even small deviations in overlapping yoke cross section increase fringing effects. Furthermore, the steel sheets samples must have the same geometric dimensions as the yoke cross section and must be placed between both yokes carefully.

Another parasitic flux component is called air flux generated by the excitation winding. It is responsible for magnetic coupling of the primary and secondary winding through air. Fig. 5.1 illustrates its path (dashed magenta line). Similar to fringing flux effects, it contributes to an erroneous flux density measurement. The design of the NDT must reduce its influence due to the lack of a compensation winding as implemented in SST and EPF (compare chapter 3.2). Hence, the primary winding is wound around the lower yoke, and

the secondary winding is placed at the upper yoke. This setup offers the greatest possible distance between both windings and decreases their coupling through air to a minimum.

Two sets of NDT measurements are necessary to calculate the magnetic properties of the investigated steel sheet samples: one with only the plastic layer present and another one where the NDT is equipped with plastic layers and steel sheet samples. The measurement with the plastic layer characterizes the power loss of the yokes which is subtracted from measured data while the NDT is equipped with both plastic layers and steel sheet samples to acquire the magnetic properties of the samples only (compare subsection 5.4.1). A homogeneous flux density distribution all over the distance between upper and lower yoke is required to enable a comparison of measurements with and without steel sheet samples. A 2D model of the NDT is realized in the FE Software ANSYS Maxwell 2016 to investigate the flux density distribution in the measurement device. The software relies on the Maxwell equations explained in chapter 2.3. The NDT cannot be modeled in all details. The following paragraph explains the model simplifications.

Only one-half of the NDT needs to be implemented due to symmetry. An even symmetry boundary, which zeros the tangential component of the field, is applied to the cross section of the yokes indicated by the blue dashed lines in Fig. 5.1. Both yokes are treated as one magnetically isotropic object. A stacking factor of 95 % known from the yoke manufacturer defines the relation of steel, coating and air gaps between the steel sheets. An *inductive* BH-curve measured with an SST (compare chapter 4.3) characterizes the magnetic properties of the electrical steel (H103-27). When a steel sheet sample is part of the modeled setup, its relative permeability is assumed to be constant with a value of 100. This value is a rough approximation based on experiments stated in [32]. The sample thickness  $d_{\text{sheet}}$  is set to 350  $\mu\text{m}$  which is the highest thickness available for grain-orientated electrical steel [69] leading to the maximum expectable impact of parasitic effects mentioned before.

The primary winding is part of the model setup for excitation which is realized as stranded winding with 20 turns. The impact of eddy currents is neglected in this first investigation because their implementation is rather complex and requires a 3D model introduced in subsection 5.3.2. A transient simulation of the NDT is performed, and a cosinusoidal excitation voltage is applied. The maximum flux density  $\hat{B}$  is reached after a quarter period leading to a simulation time of 5 ms in this case. Time steps of  $\Delta t = 100 \mu\text{s}$  and a nonlinear residual of  $10^{-7}$  describe the transient simulation. Fig. 5.5 illustrates the flux density distribution belonging to an excitation of 1 T and a simulation time of 5 ms. It shows the NDT with steel sheet sample (a) and without (b)). Both flux density distributions equal each other, which is necessary to determine the characteristics of electrical steel explained in section 5.4.1. The flux density in the middle of the plastic layer along the red dashed line in Fig. 5.1 is simulated for each excitation flux density from 0.1 T to 1.0 T. In the

case of a simulation with steel sheet samples, the flux density distribution in the middle of the sample is analyzed for the same excitations. The width of plastic layer or steel sheet is sampled with 1001 points. A change in flux density equals its inhomogeneity. Fig. 5.6 illustrates the flux density distributions along the width of plastic layer or steel sheet sample.

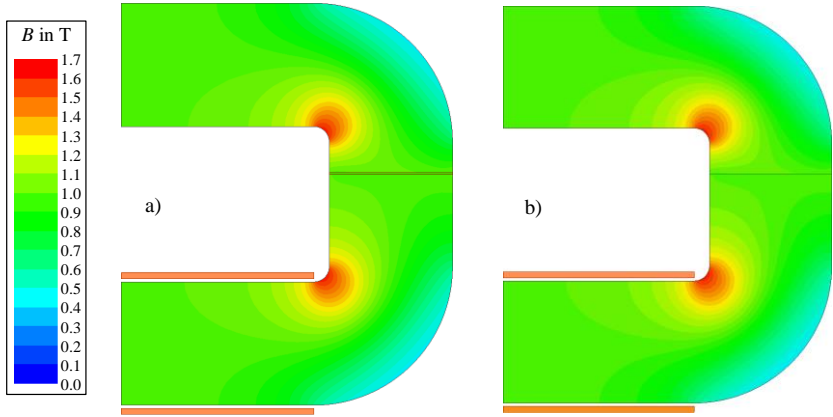


**Fig. 5.5:** Flux density distribution in NDT with (a) and without steel sheet sample (b) with an excitation of 1 T and a simulation time of 5 ms

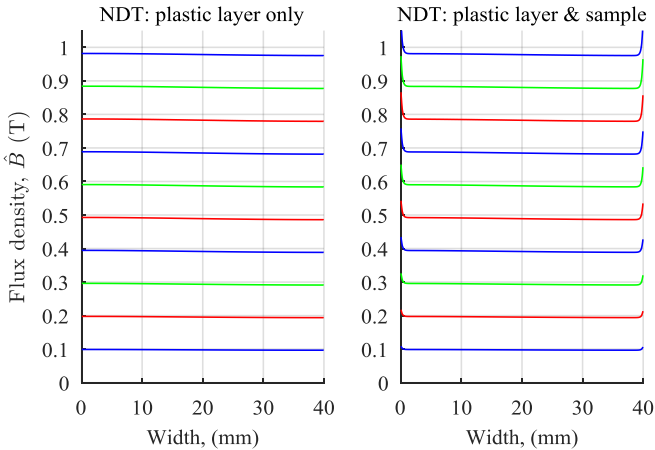


**Fig. 5.6:** Flux density distribution in plastic layer (left) and in steel sheet sample (right)

A homogeneity difference between flux density in plastic layer or steel sheet sample can hardly be estimated, despite a flux density increase along the edges of the sample at 0 mm and 40 mm. Thus, the relative standard deviation  $\gamma$  is computed using (5.6) to describe the inhomogeneity of flux density.

$$\gamma(\bar{B}_{\text{plastic/sample}}) = \frac{\sqrt{\frac{1}{N_S - 1} \sum_{j=1}^{N_S} (B_{\text{plastic/sample}}(j) - \bar{B}_{\text{plastic/sample}})^2}}{\bar{B}_{\text{plastic/sample}}} \cdot 100\% \quad (5.6)$$

The variable  $j$  denotes the point index, and  $N_S$  represents the total number points. The first and the last point are neglected to avoid boundary errors due to a change in permeability along the edge of the sample.

Fig. 5.7 demonstrates the relative standard deviation  $\gamma$  as a function of the average flux density  $\bar{B}$  in for both cases: NDT equipped with a plastic layer only and including a steel sheet sample.

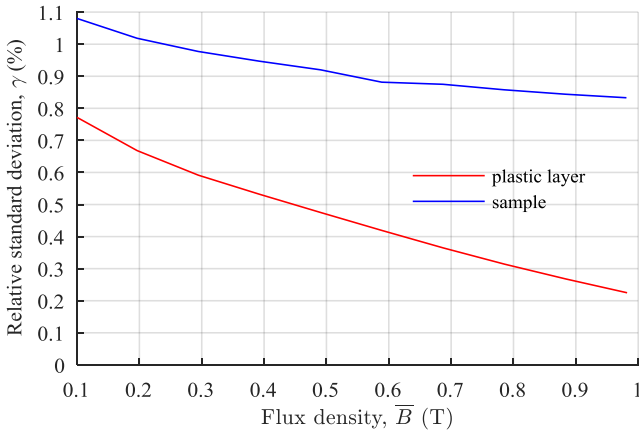


**Fig. 5.7:** Relative standard deviation of flux density in plastic layer and steel sample

Simulation results with plastic only show a smaller standard deviation compared to the results based on a sample. Nevertheless, the flux density distributions in plastic layer and steel sheet sample are assumed to be homogeneous due to their small relative standard deviations  $\gamma$  of less than 1.1 %.

During both simulations, the flux density distribution along the cross section of the upper yoke in the secondary winding (see upper blue dashed line in Fig. 5.1) are analyzed (Fig. 5.8). The average flux density in this part of the yoke is proportional to the measured secondary voltage which is utilized to characterize the conditions in the sample or plastic layer. Hence, a difference between average flux density  $\bar{B}_{\text{yoke}}$  in the upper yoke and average flux density  $\bar{B}_{\text{plastic/sample}}$  in plastic layer or sample leads to a misinterpretation of the sample's magnetic properties. However, the flux distribution in the upper yoke needs not to be homogeneous since the voltage induced in the secondary winding depends on the derivative of the flux, which is the surface integral of the flux density and therefore the average the flux density multiplied with the cross section area of the upper yoke (5.7).

$$U_2 = -\frac{d\Phi}{dt} = -N_2 \frac{d}{dt} \int_A B_{\text{yoke}} dA_{\text{Fe}} = -N_2 \frac{d}{dt} \bar{B}_{\text{yoke}} A_{\text{Fe}} \quad (5.7)$$

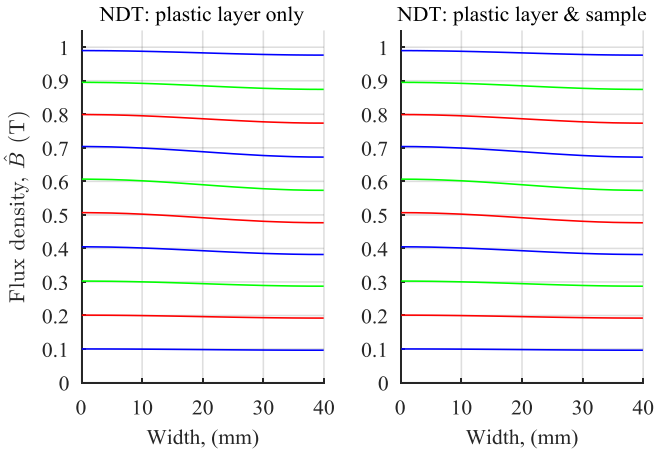


**Fig. 5.8:** Flux density distribution in upper yoke while NDT is equipped with plastic layer only or plastic layer and steel sheet sample

A comparison of  $\bar{B}_{\text{plastic/sample}}$  and  $\bar{B}_{\text{yoke}}$  evaluates the influence of fringing and air flux. Equation (5.8) computes the relative flux density deviation  $\delta$ :

$$\delta = \frac{\bar{B}_{\text{upper yoke}} - \bar{B}_{\text{plastic/sample}}}{\bar{B}_{\text{plastic/sample}}} \cdot 100\% . \quad (5.8)$$

Fig. 5.9 demonstrates the results of this calculation. The relative flux density deviation  $\delta$  is almost constant in the investigated flux density range. If there is only a plastic layer part of the setup, the relative deviation is less than 0.3 %. When a combination of plastic layer and steel sheet sample is applied,  $\delta$  stays below 0.4 %. Both percentages are considered to be acceptable. The 2D FE simulations of the NDT prove that the influence of parasitic flux paths and inhomogeneity of flux density are within an applicable range. Thus, the NDT is a suitable measurement device to investigate magnetic characteristics in normal direction of the applied flux density.

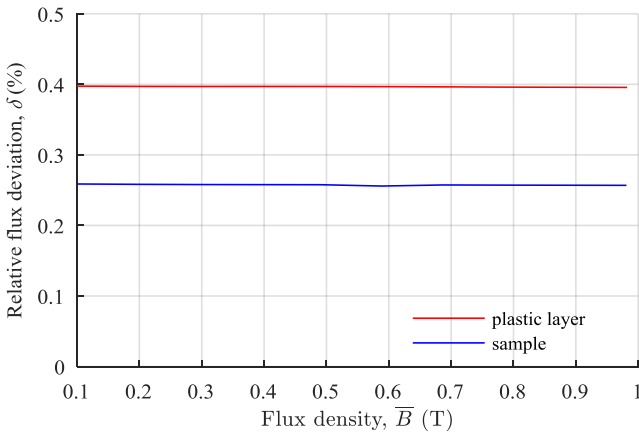


**Fig. 5.9:** Relative deviation  $\delta$  of the flux density distribution in plastic layer and steel sheet sample

### 5.3.2 Consideration of eddy currents

The surface of the steel sheet samples is penetrated by the applied flux density producing a high eddy current density as illustrated in Fig. 5.10. It is evident that the eddy currents strongly depend on the geometric dimensions of steel sheet samples due to Faraday's law.

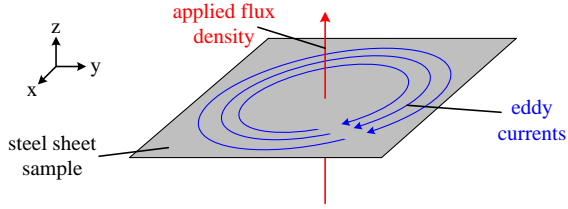


**Fig. 5.10:** Eddy currents inside the steel sheet sample

The eddy current distribution affects homogeneity of flux density inside the sample which is essential for the comparison of measurements with and without samples. The Maxwell equations explain the relationship of applied flux density  $B$  and generated eddy current density  $J$  (compare section 2.3):

$$\begin{aligned}\nabla \times \vec{E}(t) &= -\frac{\partial \vec{B}(t)}{\partial t} \\ \nabla \times \vec{J}_1(t) &= -\sigma \frac{\partial \vec{B}(t)}{\partial t} .\end{aligned}\quad (5.9)$$

The flux density  $B(t)$  is assumed to be sinusoidal and by introducing the complex exponential form, equation (5.9) is rewritten as:

$$\nabla \times \vec{J}_1 = -j\omega\sigma\vec{B} .\quad (5.10)$$

The current density  $J_1$  only depends on  $x$ - and  $y$ -axes leading to the final equation (5.11) [62]:

$$\frac{\delta J_{1,y}}{\delta x} - \frac{\delta J_{1,x}}{\delta y} = -j\omega\sigma B_z .\quad (5.11)$$

The current distribution components in  $x$ - and  $y$ -direction create a flux density along the  $z$ -axis, but there is a phase shift between both quantities of  $90^\circ$ . The flux density reaches its time-related maximum while the current density is zero and vice versa. Hence, the flux density must be analyzed during its time corresponding maximum to assure homogeneity. There is an analytic approach in literature [36] to calculate eddy current and flux density for steel plates with arbitrary geometric dimensions. It is based on sophisticated series expansions and rather complex. Therefore, an FE simulation of the NDT in ANSYS Max-

well is performed. A 3D model is necessary to describe eddy effects in the sample correctly. In contrast to the 2D approach in 5.3.1, the 3D simulation is executed for a flux density of 1.0 T only because it is very time-consuming and a lot of processing power is necessary.

Again an *inductive* BH-curve describes the magnetic properties of the yoke material. A relative permeability of 100 characterizes the magnetic properties of the steel sheet sample and its thickness equals 350  $\mu\text{m}$  similar to the 2D simulation in part 5.3.1. Only one-quarter of the NDT needs to be implemented in the FE software due to symmetry. An odd symmetry boundary, where the normal component of the magnetic field is zero, is defined for the vertical middle of the NDT. Other boundaries are defined alike the 2D FE simulation in subsection 5.3.1. A simulation time of 20 ms for a transient simulation is necessary to reach steady state conditions. Time steps of  $\Delta t = 100 \mu\text{s}$  and a nonlinear residual of  $10^{-7}$  are applied.

Fig. 5.11 a) demonstrates the generated mesh in the entire NDT model on the left and inside the sample on the right-hand side. It consists of approximately 150,000 elements caused by the difference in size of yokes and sample. Fig. 5.11 b) illustrates the flux density distribution in its time-related maximum. Especially the distribution inside the sample proves a uniform flux density. The maximum eddy current density inside the sample (Fig. 5.11 c), upper part) increases from the sample center to its outer edges and does not distort the flux density in its time related maximum. However, eddy currents generate a flux density themselves (Fig. 5.11 c), lower part). The question is, whether this flux density affects the power loss of the yokes whereas the NDT is equipped with plastic layer and sample. The average flux density values yields 0.26 T and causes a specific total loss of about 0.034 W/kg in the volume of the yokes close to the sample. The applied flux density of 1 T in this case generates a specific total loss value of approximately 0.37 W/kg all over the yokes which is at least ten times bigger. Thus, the impact of additional power losses in the yokes of the NDT caused by flux density as a result of eddy currents in the samples are neglected due to their small value and their localized appearance. It is assumed that a NDT measurement without sample represents the power loss of the yokes in a measurement with samples.

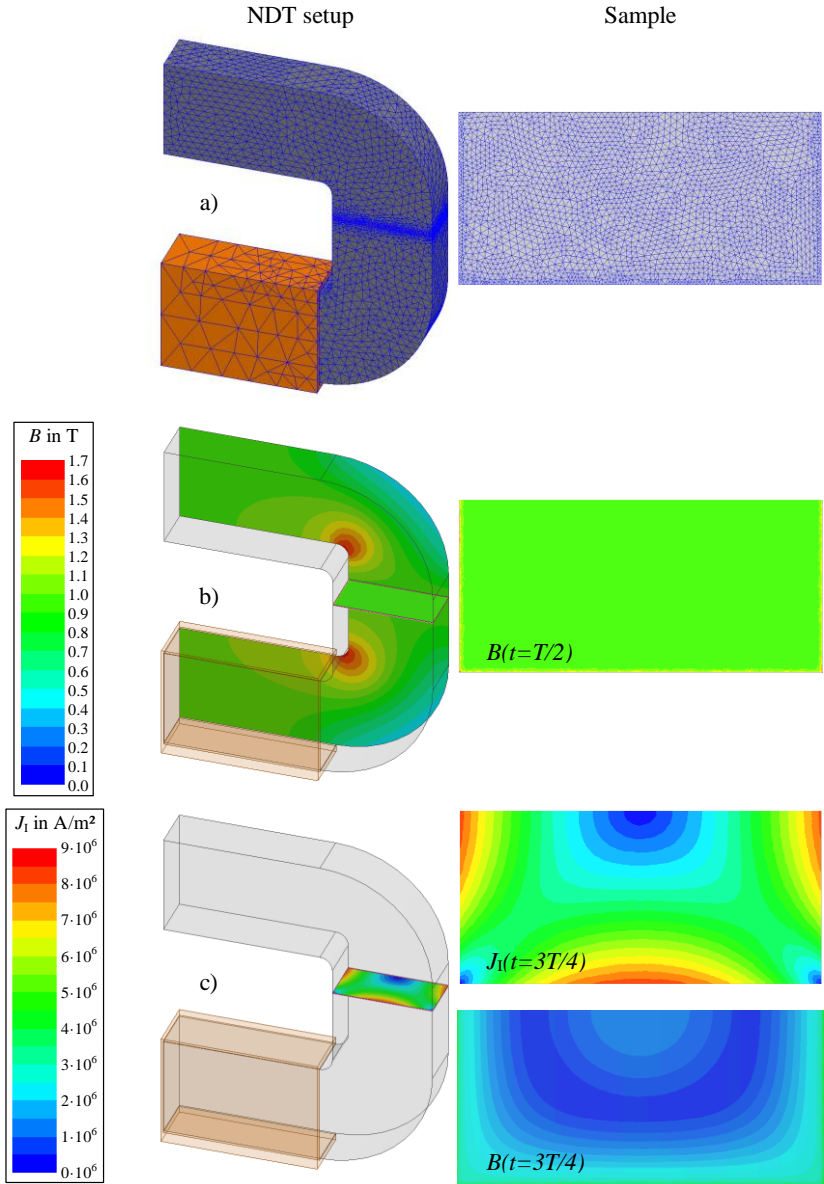


**Fig. 5.11:** 3D FE simulation of the NDT: a) mesh, b) flux density and c) eddy current distribution

Equation (5.12) computes the generated loss per cycle based on this eddy current density distribution [39]. The conductivity of the sample  $\sigma$  of 2.0833 MS/m is stated in the datasheets [37, 64] and  $V$  symbolizes the volume of the sample. Eddy currents are supposed to be sinusoidal.

$$P_{\text{EC}} = \int \frac{2}{T} \left( \int_{0.5T}^T \frac{(J_1(t))^2}{\sigma} dt \right) dV \quad (5.12)$$

Sample size affects the eddy current losses  $P_{\text{EC}}$  and turns specific total loss  $P_s$  as well as specific apparent power  $S_s$  into inappropriate criteria to characterize magnetic properties orthogonal to the sheet plane. Different sample sizes would cause varying results in  $P_s$  and  $S_s$ . Further on, the geometric conditions in transformer cores where normal flux occurs are always different. Thus, specific power loss as a result of flux density orthogonal to the sheet plane is not analyzed in this work.

## 5.4 Measurement and data analysis

Both yokes of the NDT and the investigated steel sheet samples have the same cross section. Hence, the same flux density is applied to both of them. The influence of the yokes on the measurements cannot be neglected. Two series of measurements, one with and one without steel sheet sample are necessary. Flux density is controlled regarding waveform and amplitude during both series similar to [70, 72]. In the following, the BH-curve of the steel sheet samples is determined. However, eddy currents generated in the sample by the applied flux density must be considered at first.

### 5.4.1 BH-curve determination

The size of the investigated steel sheet samples and geometric conditions in an electromagnetic device like power transformers strongly affect eddy currents generated by flux orthogonal to the sheet plane (compare subsection 5.3.2). Hence, the magnetic properties of electrical steel can only be determined when eddy effects do not occur.

The vector diagram in Fig. 5.12 a) explains the relationship of flux density  $B$ , secondary voltage  $U_2$  and primary current  $I_1$  in the NDT equipped with steel sheet samples. The secondary voltage  $U_2$  is placed on the real axis in the diagram, and the flux density  $B$  is aligned with the imaginary axis due to the phase shift of  $90^\circ$  between the two quantities. The current  $I_1$  is separated into its real ( $I_{1,\text{real}}$ ) and imaginary ( $I_{1,\text{im}}$ ) part. The time-related

change in flux density  $B$  induces the eddy currents  $I_{EC}$  in the yokes and primarily in the samples. They are in phase with the real axis and the secondary voltage  $U_2$ . The real part of the primary current  $I_{1, \text{real}}$  consists of eddy currents  $I_{EC}$  and the real component of the magnetization current  $I_{\mu, \text{real}}$  caused by hysteresis and excess loss (compare subsection 2.2.2). The imaginary part of the magnetization current  $I_{\mu, \text{im}}$  is parallel with the flux density  $B$ . Since the induced eddy currents  $I_{EC}$  are zero when the sinusoidal flux density reaches its maximum, the primary current  $I_1$  equals the imaginary part of the magnetization current  $I_{\mu, \text{im}}$ , which is used to calculate the magnetic field  $H$ .

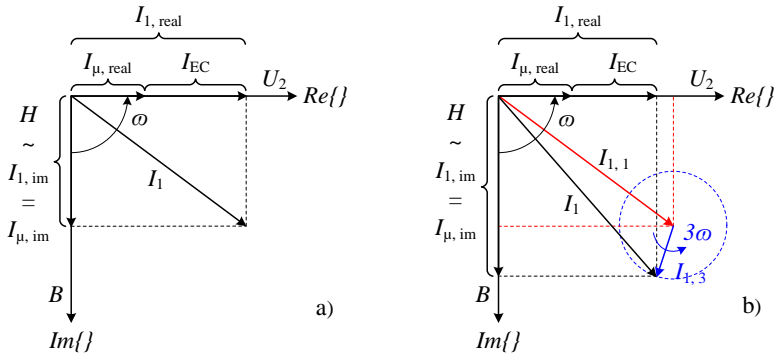


**Fig. 5.12:** Vector diagram of real and imaginary current (a) and harmonic components in  $I_1$  (b)

This method to avoid the impact of eddy currents is only allowed when there are negligibly small harmonics part of the primary current  $I_1$ . Fig. 5.12 b) illustrates the influence of the third harmonic  $I_{1,3}$  as an example (colored in blue). The amplitude of the primary current  $I_1$  is the sum of its fundamental  $I_{1,1}$  and the third harmonic  $I_{1,3}$ . If the participation of harmonics in  $I_1$  is significant, the content of eddy currents and magnetization current are not interpreted correctly. The red dashed lines indicate the results for current components achieved without harmonics.

Several NDT measurements without samples and equipped with different steel grades are performed (Table 5.1). The  $THD$  (equation (3.6)) of the primary current  $I_1$  is calculated and is always less than 1 %. Since the content of harmonics in the primary current is small, their influence is neglected, and magnetization current can be determined as sketched in Fig. 5.12 a). As a result, the BH-curve describing magnetic properties in normal direction consists of the maximum flux density value and the time corresponding magnetic field value. This kind of magnetization curve is introduced in section 4.3 and is called *inductive* BH-curve. Equation (5.13) describes the calculation of the *inductive* magnetic field  $H_L$  in the NDT with and without steel sheet samples as a summation of the cosinus components

$a_h$  in a Fourier expansion of the magnetic field. The variable  $h$  denotes the number of applied orders which is one as explained above.

$$H_L(\hat{B}) = \sum_{h=1}^1 [a_h(\hat{B})] \quad (5.13)$$

The hysteresis model offers the possibility to determine a magnetic field value for an arbitrary flux density amplitude  $\hat{B}$ , which is necessary for the calculation of the magnetic field in the sheet, where an *inductive* BH-curve with and without steel sheet sample is required. To avoid errors, both curves must rely on the same flux density vector and not on the individually measured flux density amplitudes.

An equivalent magnetic circuit is used to explain the BH-curve determination of the samples. The Hopkinson's law describes this kind of circuit with a simple example in Fig. 5.13.

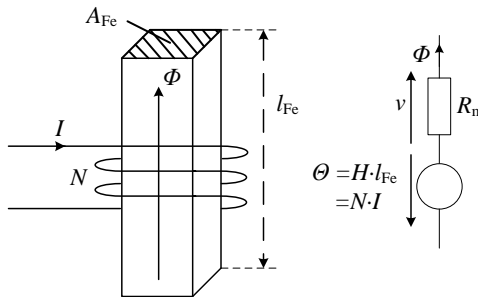


**Fig. 5.13:** Hopkinson's law [34]

Equation (5.14) computes the magneto-motive force  $\Theta$  which equals the electromotive force with the magnetic field  $H$  and the average magnetic path length  $l_{Fe}$  or the number of turns  $N$  in the excitation winding and the applied current  $I$ . Ampere's law defines this relationship:

$$\Theta = H \cdot l_{Fe} = N \cdot I . \quad (5.14)$$

The magnetic voltage  $v$  matches the electric voltage, and the magnetic flux  $\Phi$  stands for the magnetic current. The magnetic resistance  $R_m$  connects flux and magnetic voltage [34] which depends on the average magnetic path length  $l_{Fe}$ , the cross section  $A_{Fe}$  of the

ferromagnetic material inside the excitation winding and the permeability  $\mu$  of the ferromagnetic material (5.15).

$$v = \Phi \cdot R_m = \Phi \cdot \frac{l_{Fe}}{\mu \cdot A_{Fe}} \tag{5.15}$$

The Hopkinson's law is applied to the NDT and leads to the magnetic circuit illustrated in Fig. 5.14. A complete circuit is shown on the left; an individual magnetic resistance expresses each circuit component. On the right-hand side, the full circuit is simplified. The NDT measurement without steel sheet samples represents the magnetic voltage drop across yokes and plastic layers in a NDT equipped with samples.

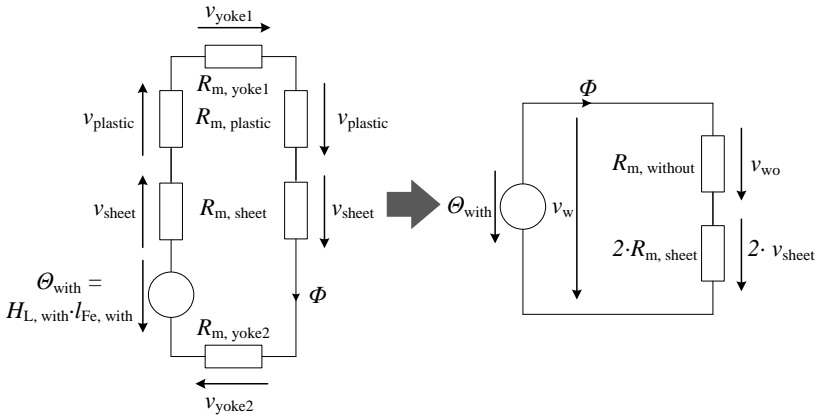


**Fig. 5.14:** Magnetic circuit of the NDT

Equation (5.16) describes the simplified circuit in Fig. 5.14 and the calculation of the magnetic field  $H_{L, sheet}$ . It contains information about the field in steel and coating of the steel sheet sample. Therefore, the characteristics of the entire sheet with steel and coating are related to the thickness of steel  $d_{sheet}$ .

$$\begin{aligned}
 v_{\text{with}} &= v_{\text{without}} + 2v_{\text{steel}} \\
 H_{L, \text{with}} l_{\text{Fe, with}} &= H_{L, \text{without}} l_{\text{Fe, without}} + 2\Phi R_{m, \text{sheet}} \\
 \Phi R_{m, \text{steel}} &= \frac{H_{L, \text{with}} l_{\text{Fe, with}} - H_{L, \text{without}} l_{\text{Fe, without}}}{2} \\
 \Phi \frac{d_{\text{sheet}}}{\mu_{\text{steel}} A_{\text{Fe}}} &= \frac{H_{L, \text{with}} l_{\text{Fe, with}} - H_{L, \text{without}} l_{\text{Fe, without}}}{2} \\
 \frac{\hat{B}}{\mu_{\text{steel}}} d_{\text{sheet}} &= \frac{H_{L, \text{with}} l_{\text{Fe, with}} - H_{L, \text{without}} l_{\text{Fe, without}}}{2} \\
 \rightarrow H_{L, \text{sheet}} &= \frac{H_{L, \text{with}} l_{\text{Fe, with}} - H_{L, \text{without}} l_{\text{Fe, without}}}{2d_{\text{sheet}}}
 \end{aligned} \tag{5.16}$$

This thickness must be measured on several samples with a micrometer gauge, and an average value is calculated (Table 5.1). The thickness stated in the datasheet of the electrical steel grade is not sufficient due to the allowed tolerances of  $\pm 25 \mu\text{m}$  to  $\pm 30 \mu\text{m}$  [69] which would have a significant influence on the calculated magnetic field.

NDT measurements with only plastic layers present and equipped with both plastic layers and steel sheet samples are performed in a flux density range from 0.05 T to 1.0 T in 0.05 T steps and a frequency of 50 Hz. Five different electrical steel grades are investigated as listed in Table 5.1. Their manufacturers are unknown despite for the first and the last quality.

To estimate the reproducibility of the measurement procedure, five sample pairs per steel grade are analyzed, respectively. Additionally, NDT measurements without samples are repeated five times. The BH-curve of every single measurement is determined, and the relative standard deviation  $\gamma$  of the magnetic field in the NDT with and without samples is computed (compare (5.6)). Fig. 5.15 illustrates the relative standard deviation  $\gamma$  for five repetitions per steel grade and five measurements without samples as function of the applied flux density. Sample measurements produce the highest deviation of 2.2 % for small flux density values. However,  $\gamma$  decreases with increasing excitation flux density amplitudes. While the NDT is empty and only plastic layers are present, an approximately constant relative standard deviation of 0.25 % is achieved. Both approaches validate the NDT being a suitable measurement device to determine the magnetic field within a good reproducibility.

The sample preparation is of great importance, especially the influence of cutting the steel sheet samples must be reduced to a minimum. During the first NDT test measurements, the cutting edges of the used samples were bent and had burrs which were responsible for

an increase in the relative standard deviation of up to 20 %. The knife of the plate shears was replaced, and the negative impact of the sample cutting could be decreased leading to the small relative standard deviation mentioned above.

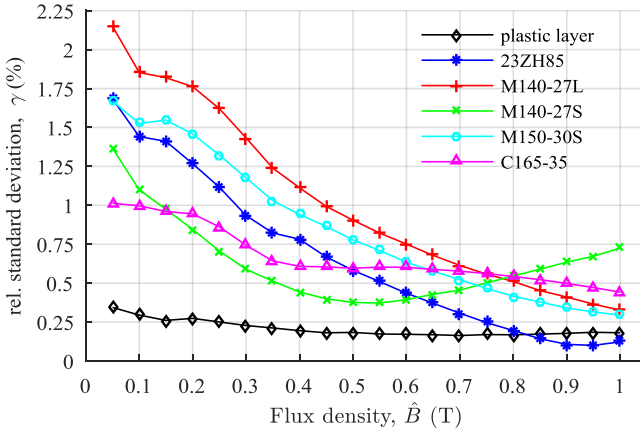


**Fig. 5.15:** Relative standard deviation in magnetic field measurements with NDT

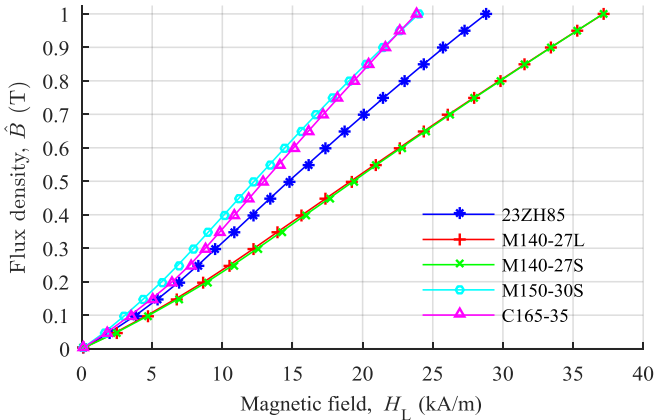
The *inductive* BH-curves for each investigated steel grade are calculated based on equation (5.16). Fig. 5.16 illustrates the results of these calculations. There is an almost linear relationship between magnetic field and flux density for all five different steel qualities leading to an approximately constant relative permeability  $\mu_r$  (5.17).

$$\mu_r = \frac{\hat{B}}{\mu_0 \left( \frac{H_{L, \text{with } l_{\text{Fe, with}}} - H_{L, \text{without } l_{\text{Fe, without}}}}{2d_{\text{sheet}}} \right)} \quad (5.17)$$

A linear regression computes an average relative permeability  $\mu_r$ . Table 5.1 shows the average relative permeability  $\mu_r$  of each electrical steel quality and the relative standard deviation describing the difference between  $\mu_r$  and the slope of the BH-curve. The small deviation of less than 3 % verifies the average relative permeability  $\mu_r$  as a good approximation of the magnetization behavior in normal direction. The values for the relative permeability of all steel qualities are within a range of 20 to 40. The electrical steel qualities of the grades in Table 5.1 are ranked in ascending order. A relationship between steel quality and  $\mu_r$  in normal direction cannot be found. Further on, there is no dependence of  $\mu_r$  and the steel grade thickness  $d_{\text{sheet}}$ .

**Table 5.1:** Investigated electrical steel grades

| Name     | Manufacturer   | $d_{\text{sheet}}$<br>in $\mu\text{m}$ | $m_{\text{sample}}$<br>in g | $\mu_r$ in normal direction |  |
|----------|----------------|--|-----------------------------|-----------------------------|--|
|          |                |  |                             | $\mu_r$                     | rel. standard deviation $\gamma$<br>in % |
| 23ZH85   | Nippon Steel   | 226.3                                  | 5.38                        | 27.4                        | 2.1                                      |
| M140-27L | <i>unknown</i> | 265.3                                  | 6.27                        | 21.1                        | 1.7                                      |
| M140-27S | <i>unknown</i> | 264.9                                  | 6.26                        | 21.1                        | 1.9                                      |
| M150-30S | <i>unknown</i> | 287.1                                  | 6.93                        | 33.0                        | 1.9                                      |
| C165-35  | ThyssenKrupp   | 342.3                                  | 8.15                        | 32.1                        | 2.9                                      |

**Fig. 5.16:** Inductive BH-curves of different steel grades in normal direction

Finally, Fig. 5.17 compares the magnetic behavior of electrical steel in rolling, trans-rolling and normal direction for a C165-35 steel grade. The magnetic field in trans-rolling direction is measured from 0.05 T to 1.5 T in 0.05 T steps because magnetic saturation is reached at a flux density of 1.5 T. The comparison is an example for the high anisotropy of electrical steel along the three spatial axis  $x$ ,  $y$  and  $z$ . Table 5.2 gives the relative permeability at a flux density amplitude of 1 T for all directions. Their anisotropic relationship is evident due to a factor of about 10 between relative permeability in rolling and trans-rolling direction as well as a  $\mu_r$ -ratio of approximately 1000 between rolling and normal direction.

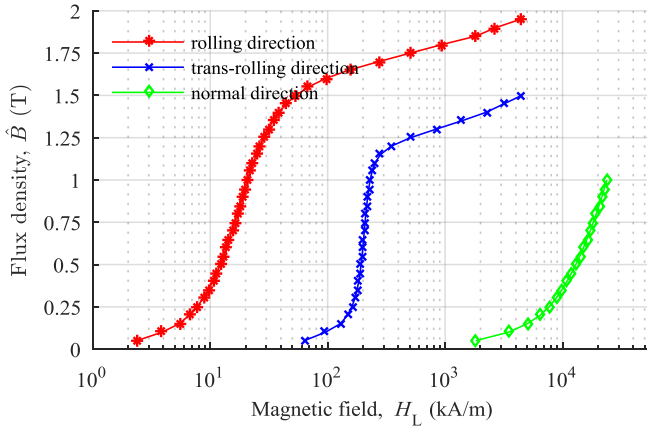


**Fig. 5.17:** Comparison of *inductive* BH-curves in rolling, trans-rolling and normal direction of the steel grade C165-35

**Table 5.2:** Relative permeability comparison of different directions

|                                | rolling direction | trans-rolling direction | normal direction |
|--------------------------------|-------------------|-------------------------|------------------|
| $\mu_r(\hat{B} = 1 \text{ T})$ | 38314             | 3459                    | 32.1             |

## 5.4.2 Calculation of eddy current losses

Subsection 5.3.2 explains, that eddy current losses generated by flux density orthogonal to the sheet plane depend on the geometric dimensions of the investigated setup and its magnetic properties. These losses are calculated for NDT samples in this part of the thesis. Again a 3D simulation of the NDT is necessary while the sample thickness and the relative permeability of two different steel grades are applied. A high-performance steel 23ZH85 and a low-cost material C165-35 are chosen to cover the variety of electrical steel qualities. Equation (5.12) computes the losses with the current density inside the sample.

$$P_{\text{EC}} \sim \hat{H}^2 \rightarrow P_{\text{EC}} \sim \hat{B}^2 \rightarrow P_{\text{EC}} = c_p \cdot \hat{B}^2 \quad (5.18)$$

According to [36], the eddy current losses are proportional to the applied magnetic field amplitude squared. While the relative permeability is assumed to be constant, the described relationship is also valid for the corresponding flux density amplitude. With the introduction of the constant  $c_p$ , which represents material and geometric properties of the sample, eddy current losses can be determined for arbitrary flux densities.

To prove equation (5.18), the eddy current distribution is simulated in a flux density range from 0.2 T to 1.0 T in 0.2 T steps and the constant  $c_p$  is calculated for eddy current loss at 0.2 T. Fig. 5.18 shows the relative error of simulated and calculated eddy current losses for the both steel grades over the flux density range. The relative error is always below 0.02 % attesting an excellent accuracy of the calculation (5.18), and therefore only one excitation needs to be simulated which saves simulation time.

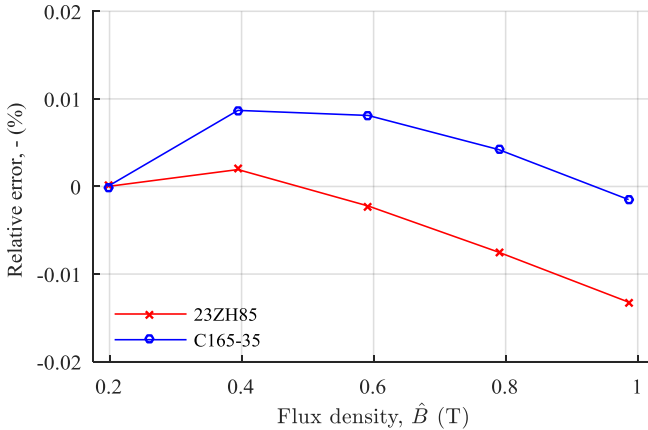


**Fig. 5.18:** Relative error in simulated and calculated eddy current losses for the steel grades 23ZH85 and C165-35

Fig. 5.19 and Fig. 5.20 illustrate the entire measured losses  $P_{\text{entire}}$  and the calculated eddy current losses  $P_{\text{EC}}$  for both steel grades investigated with the NDT.

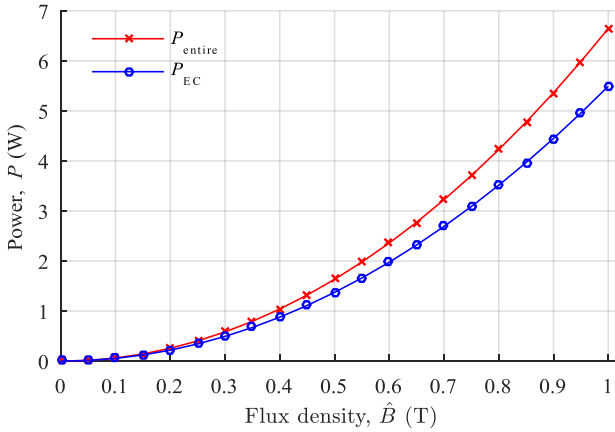


**Fig. 5.19:** Comparison of entire and eddy current losses of steel grade C165-35

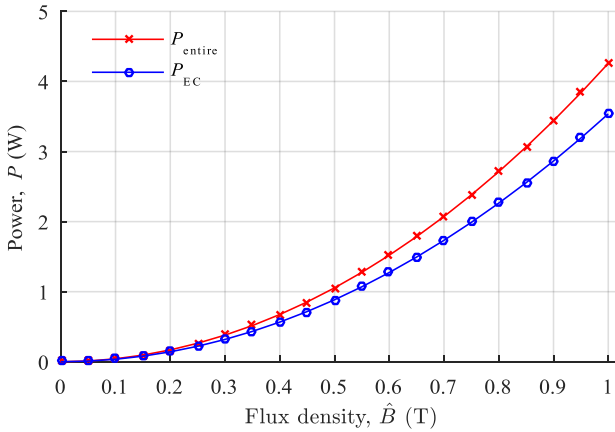


**Fig. 5.20:** Comparison of entire and eddy current losses of steel grade 23ZH85

The eddy current losses are mainly responsible for the active power consumption of the steel sheet. A loss separation into hysteresis, eddy current and excess loss as introduced in subsection 2.2.2 is not allowed because the flux density is not homogeneous despite in its time-related maximum. During all other time steps, the flux density is distorted by the eddy current density as illustrated in Fig. 5.11. This relationship is accomplished by equation (5.11). The difference between entire and calculated eddy current power consumption

(compare Fig. 5.19 and Fig. 5.20) equals hysteresis and excess losses but they depend on the sample geometry due to the mostly inhomogeneous flux density distribution. A determination of specific hysteresis and excess losses is not possible with this sample size dependency. Therefore, the calculation of eddy current losses is a good approximation to estimate losses created by flux density in normal direction.



# 6 Simulation of core losses

The simulation of core losses requires a power transformers modeling of sufficient accuracy. There are several different approaches to model power transformers [35] which can be separated according to their purpose. One possibility is a combination of magnetic and electric circuits which describe the magnetic behavior of the core and the electric relationship of excitation voltage and current as it is proposed in [78]. In this work, transformer modeling based on the Finite Element Method (FEM) is the most appropriate approach to simulate core losses. It is possible to implement the geometric dimensions of the investigated transformer in detail and to characterize magnetic properties of the used electrical steel close to reality relying on measured data. A good cooperation with the transformer manufacturer is essential in order to get construction plans of the modeled devices. All simulations are performed under steady state conditions only. Fast transients such as inrush currents are out of scope for this investigation.

The approach to simulate core losses in power transformers introduced in this chapter consists of two main steps: In the first place, a Finite Element (FE) model and simulation of the investigated electromagnetic device is needed to acquire a flux density and a magnetic field distribution. Furthermore, a post-processing algorithm determines the losses in the active magnetic material.

## 6.1 Concept of FE simulation and post-processing

This section presents a brief overview of the FE simulation coupled with the post-processing algorithm (Fig. 6.1). All investigated electromagnetic devices are implemented in the FE Software ANSYS Maxwell 2016. A simplified model in 2D or 3D is realized relying on blueprints or other construction data. The main interest is set on parts made of electrical steel because the focus of this work are the losses produced within the core, and geometric deviations have a major impact on the simulation results. The BH-curves determined in chapter 4.3 characterize the nonlinear magnetic behavior of the used electrical steel. A transient simulation with a sinusoidal voltage as excitation is performed. The eddy current solver is less accurate than the transient solver according to the manufacturer of the used software. The simulation generates a magnetic field and flux density distribution within the magnetically active components of the model. Both distributions including mesh information are exported as a text file for post-processing operations which are realized using MATLAB. During post-processing, the loss per finite element is computed

based on imported and measured data. The entire loss generated by the modeled device is a summation of all losses per element. The following section explains the concept of the post-processing algorithm.

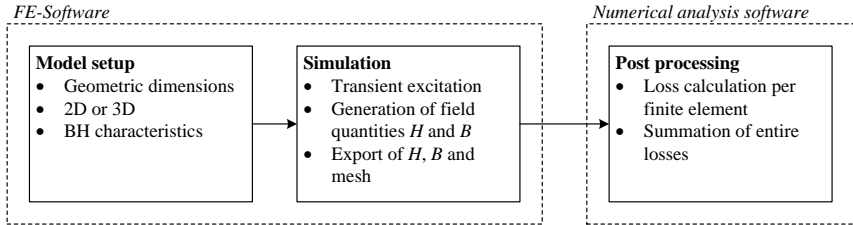


**Fig. 6.1:** Flow chart of FE simulation combined with post-processing

The details of FE simulations strongly depend on the modeled electromagnetic device. Hence, all specific information about each discussed device is given in the respective subchapter. A core loss calculation is already part of the used FE software. However, there are shortcomings in the implementation of the specific total loss leading to unsatisfying loss simulation results (compare section 2.2.2). Thus, a novel post-processing algorithm to determine core losses was developed. This algorithm is different depending on a 2D or 3D simulation model. As mentioned earlier, magnetic field and flux density at every single point of the modeled electrical steel parts are provided by the FE simulation. The geometry data which are also exported describe the shape and the position of each finite element.

At first, the geometry of each element is analyzed. In ANSYS Maxwell the finite elements of a 2D application are triangles and in 3D approach pyramids (Fig. 6.2). Triangles are defined by the three points ( $p_1$  to  $p_3$ ), whereas pyramids consist of four points ( $p_1$  to  $p_4$ ).

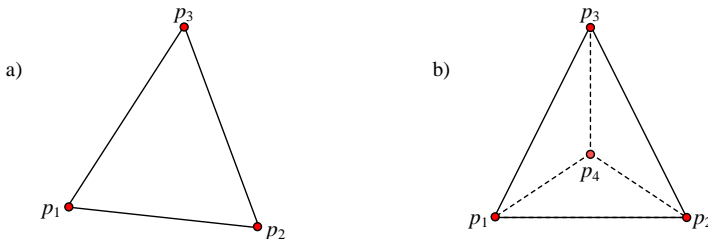


**Fig. 6.2:** Finite element in a 2D (a) and 3D (b) application

Equation (6.1) computes the triangle area  $A_{\text{triangle}}$ .

$$A_{\text{triangle}} = \frac{1}{2} \left| \det \begin{pmatrix} 1 & p_1(x, y) \\ 1 & p_2(x, y) \\ 1 & p_3(x, y) \end{pmatrix} \right| \quad (6.1)$$

The volume of each pyramid  $V_{\text{element}}$  is calculated in equation (6.2).

$$V_{\text{pyramid}} = \frac{1}{6} \left| \det \begin{pmatrix} p_2(x, y, z) - p_1(x, y, z) \\ p_3(x, y, z) - p_1(x, y, z) \\ p_4(x, y, z) - p_1(x, y, z) \end{pmatrix} \right| \quad (6.2)$$

The absolute values of the determinants in equation (6.1) and (6.2) are necessary because they can produce negative values depending on the coordinates of the applied points. When *maximum* or *inductive* BH-curves characterize the magnetic properties of the modeled steel part, only the flux density at each point and in all possible directions ( $x$ ,  $y$  and  $z$  in a 3D application) is exported. The average flux density per element  $\bar{B}_{xy[z]}$  is calculated for each direction separately. Equation (6.3) delivers the required values, where 3D extensions are shown in squared brackets for convenience.

$$\begin{aligned} \bar{B}_x &= \frac{\sum_{i=1}^3 B_{xi}^{[4]}}{3 [4]} \\ \bar{B}_y &= \frac{\sum_{i=1}^3 B_{yi}^{[4]}}{3 [4]} \\ \bar{B}_z &= \frac{\sum_{i=1}^3 B_{zi}^{[4]}}{3 [4]} \end{aligned} \quad (6.3)$$

The magnetic loss per element is expressed via equation (6.4).

$$P_{\text{element}} = \left( P_S(\bar{B}_x) + P_S(\bar{B}_y) + [P_S(\bar{B}_z)] \right) \cdot \rho \cdot V_{\text{element}} \quad (6.4)$$

In a 2D simulation, the volume of each element  $V_{\text{element}}$  is determined with triangle area (equation (6.1)) and model depth. For a 3D approach, the element volume  $V_{\text{element}}$  equals the result of equation (6.2). The mass of each element  $i$  is computed with the density of electrical steel  $\rho$  (here: 7,650 kg/m<sup>3</sup> [37, 64]) and its volume. Finally, the entire core losses are a summation over all elements  $q$  of the FE model (6.5).

$$P_{\text{entire}} = \sum_{i=1}^q P_{\text{element } (i)} \quad (6.5)$$

If a *resistive* BH-curve is applied in the modeling, the magnetic field data is also exported, and the average magnetic field value  $\bar{H}_{xy[z]}$  is determined in the same way as for the flux density (6.6).

$$\begin{aligned} \bar{H}_x &= \frac{\sum_{i=1}^{3 [4]} H_{xi}}{3 [4]} \\ \bar{H}_y &= \frac{\sum_{i=1}^{3 [4]} H_{yi}}{3 [4]} \\ \bar{H}_z &= \frac{\sum_{i=1}^{3 [4]} H_{zi}}{3 [4]} \end{aligned} \quad (6.6)$$

The *resistive* BH-curve is useful if the active losses in electrical steel under sinusoidal excitation are of interest. The entire active power consumption  $P$  of the transformer is computed with the input current  $I(t)$  and input voltage  $U(t)$  (6.7).

$$P = \frac{1}{T} \int_0^T I(t) \cdot U(t) dt \quad (6.7)$$

This calculation is a macroscopic treatment. In equation (6.8) the active power  $P$  is interpreted microscopically for each finite element relying on Ampere's law and Faraday's law.

$$P_{\text{element}} = \frac{V_{\text{element}}}{T} \int_0^T \left( H(t) \cdot \frac{-dB(t)}{dt} \right) dt \quad (6.8)$$

The flux density  $B(t)$  and its deviation  $dB(t)/dt$  have a sinusoidal waveform and do not contain harmonics. Hence, only the fundamental components in  $dB(t)/dt$  and  $H(t)$  which are in phase to each other are needed to calculate the consumed active power per element [22, p. 75]. They are time dependent and sinusoidal, but the solution of the integral delivers a constant value for the loss per element (6.9).

$$\begin{aligned}
 P_{element} &= \frac{V_{element}}{T} \int_0^T \left( H_R \sin(\omega t) \cdot \frac{-d\hat{B} \cos(\omega t)}{dt} \right) dt \\
 &= \frac{V_{element}}{T} \int_0^T \left( H_R \sin(\omega t) \cdot \hat{B} \omega \sin(\omega t) \right) dt \\
 &= \frac{V_{element}}{T} H_R \hat{B} \omega \int_0^T \sin^2(\omega t) dt \\
 &= \frac{H_R \hat{B} \omega}{2} V_{element}
 \end{aligned} \tag{6.9}$$

The amplitudes of the magnetic field and the flux density define the *resistive* BH-curve as explained in subsection 4.3. Similar to the *maximum* and *inductive* BH-curve approach, all spatial directions are part of the loss calculation per element (6.10).

$$P_{element} = \left( \bar{H}_x \bar{B}_x + \bar{H}_y \bar{B}_y + \left[ \bar{H}_z \bar{B}_z \right] \right) \frac{V_{element} \omega}{2} \tag{6.10}$$

Again equation (6.5) determines the entire losses.

The anisotropy of electrical steel is not considered as explained in section 4.4. Only the characteristics in rolling direction such as BH-curves and  $P_S$ -curve ( $P_S(B_{rolling}) = P_S(\bar{B}_x) = P_S(\bar{B}_y) = P_S(\bar{B}_z)$ ) describe the magnetic properties of electrical steel. These data sets are obtained by measurements or provided by the steel manufacturer. The basic concept to determine core losses as a combination of FE simulation and post-processing loss calculation were developed in [83] and further improvements were part of [84].

## 6.2 Validation with Single sheet tester model

A simple test setup approves the combination of FE simulation and post-processing algorithm. Thus, a 2D model of the SST is implemented in the FE software ANSYS Maxwell. The model is loaded with the same steel grades analyzed in chapter 4 (C160-35 and 23ZH85) and all three BH-characteristics introduced in subsection 4.3 for both grades are

analyzed. This approach neglects the magnetic anisotropy of electrical steel and assumes the same magnetic properties in all directions for the modeled steel sheet. Fig. 6.3 illustrates the SST 2D model setup.

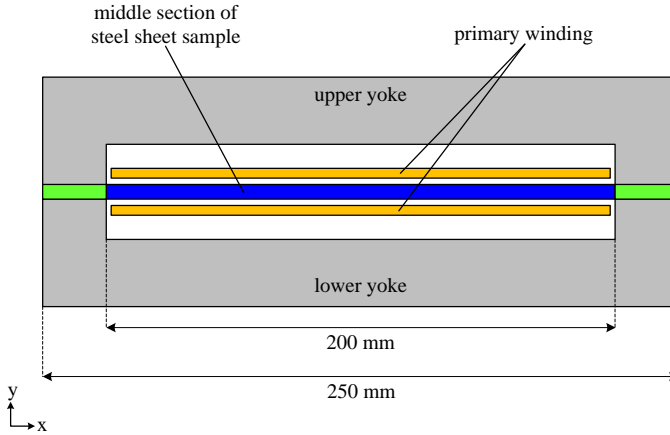


**Fig. 6.3:** Setup of the SST FE model

The yoke material is characterized by a constant relative permeability of 10,000, and only the primary winding of 150 turns is part of the model. It is treated as a stranded winding while skin and proximity effect are neglected. Since there is no secondary winding, a compensation coil which is an air transformer connected in series to primary and secondary winding is not implemented in the model (compare section 3.2). The model depth equals the width  $w$  of the modeled steel sheet sample, 250 mm in this case. The thickness of the steel sheet sample  $d_{sheet}$  is computed in compliance with [71]:

$$d_{sheet} = \frac{m_{sheet}}{w \cdot l \cdot \rho}. \quad (6.11)$$

The width  $w$  and the length  $l$  define the sample's geometric dimensions. Its mass is given by  $m_{sheet}$  and  $\rho$  denotes the density of electrical steel. The influence of the steel sheet's coating is neglected because its thickness is unknown. The difference between measured sheet thickness, obtained with a micrometer gauge, and calculated thickness using equation (6.11) estimates the air gap between yokes and steel sheet sample.

A controller for the sinusoidal waveform of the flux density is not part of the model which is not necessary because the primary winding is modeled without resistance. Therefore,

the harmonics in the excitation current cannot cause a distorted flux density in the sample. Thus, it is possible to generate a sinusoidal flux density in the sample without a controller.

A transient simulation in steps of the excitation voltage corresponding to a flux density  $B$  from 0.05 T to 1.95 T is performed. To avoid a long simulation time until reaching steady conditions a cosinusoidal excitation voltage is applied. The maximum flux density  $\hat{B}$  is reached after a quarter period due to Faraday's law. Therefore a simulation time of a quarter period is sufficient, which means 5 ms in this case. The transient FE simulation is performed in time steps of  $\Delta t = 100 \mu\text{s}$  with a nonlinear residual of  $10^{-7}$ . A VBA script exports flux density and magnetic field distribution of the sample's middle section (see blue sample part in Fig. 6.3) as text file for each excitation flux density step at a simulation time of 5 ms. This middle section corresponds to the magnetic path length  $l_{\text{Fe}}$  of the SST and equals the actively measured part of the steel sample. Due to the absence of the secondary winding in the SST model, the flux density cannot be calculated using the inducted secondary voltage. Instead, the average flux density in the middle section  $B_{\text{ms}}$  is used, which is obtained by equation (6.12).

$$B_{\text{ms}} = \frac{\sum_{i=1}^q \bar{B}_i \cdot A_i}{A_{\text{ms}}} \quad (6.12)$$

The average flux density per finite element  $\bar{B}_i$  is weighted with the element area  $A_i$ . The ratio of the sum of all  $q$  elements and the entire area of the sample's middle section  $A_{\text{ms}}$  delivers the average flux density for the middle section  $B_{\text{ms}}$ . The leakage flux increases in magnetic saturation, leading to a difference between applied flux density and the average flux density in the sample's middle section. The missing compensation coil and the lack of a secondary voltage controller are responsible for this effect. To avoid an erroneous comparison between simulated and measured power losses, the simulated results are related to the average flux density in the middle section of the steel sheet sample.

Again the two steel grades, C165-36 and 23ZH85 (compare chapter 4), are investigated, and the simulated power losses relying on a *maximum*, *inductive* and *resistive* BH-curve are compared. Fig. 6.4 illustrates the comparison of measured and simulated losses versus average flux density. Differences between the results cannot be recognized, therefore the relative error is calculated and displayed in Fig. 6.5.

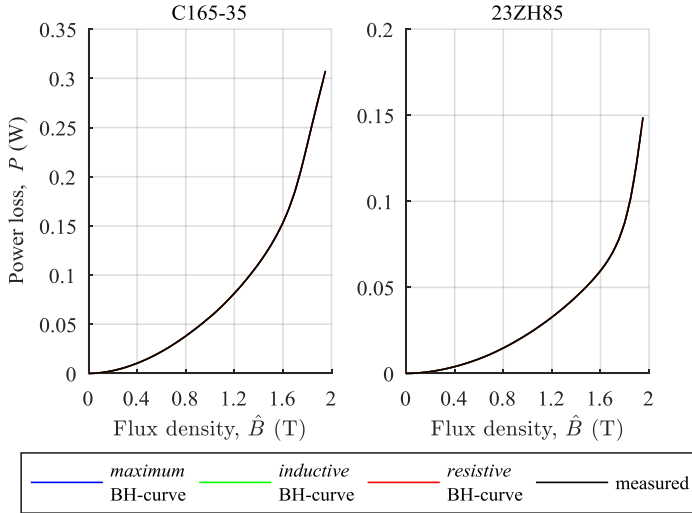


**Fig. 6.4:** Comparison of power loss determination based on *maximum*, *inductive* and *resistive* BH-curves

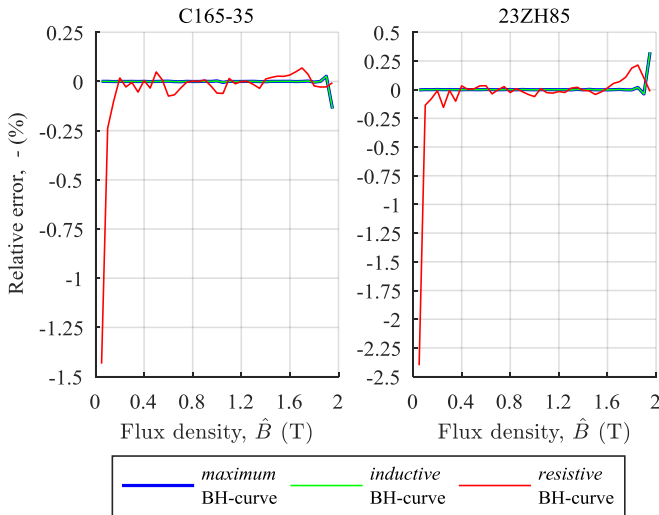


**Fig. 6.5:** Relative error in power loss determination based on *maximum*, *inductive* and *resistive* BH-curve

The loss determination relying on the *maximum* and the *inductive* BH-curve are very similar and show a good agreement across the entire flux density range, only in high saturation, a maximum error of  $\pm 0.3\%$  occurs. Simulations based on the *resistive* BH-curve deliver a higher deviation compared to measured data. Especially for small flux densities, relative errors up to  $2.5\%$  arise. Despite that, the relative error does not exceed a value of  $0.25\%$ , but its variation is higher in comparison to the other BH-curve approaches. All in all, the combination of FE simulation and post-processing algorithm delivers good results for all three BH-curves representing the magnetic characteristics of the investigated electrical steel grades.

## 6.3 Investigation of power transformers

In this part of the thesis, the core losses of power transformers will be analyzed. At first, two single phase applications and in a second step two three phase transformers are modeled, and their power consumptions without load are simulated. The manufacturer provides detailed construction plans and an SST sample of the electrical steel grade applied in the core of each transformer. All of them are manufactured by J. Schneider Elektrotechnik GmbH and are characterized by an air cooled core setup. Information about the measured no-load losses at rated terminal voltage are stated in each test certificate which is available for all devices. The magnetic anisotropy of electrical steel is not implemented in the FE model, reasons are explained in section 4.4. Furthermore, the characteristics of electrical steel in orthogonal to the sheet plane (see chapter 5) cannot be included in the modelling because an implementation of every single sheet of the transformer would be necessary to acquire the same geometric dimensions in model and the real core. Considering each steel sheet leads to a complex FE-model which even super computers cannot process in reasonable time.

### 6.3.1 Single phase transformer

#### 6.3.1.1 Transformer $T_1$

The first power transformer, called  $T_1$ , has a rating of 200 kVA. The stepped core is made of cold rolled grain-orientated steel (C 165-35) in step lap stacking. Fig. 6.6 illustrates the transformer setup. It consists of two identical winding systems connected in series (see Fig. 6.6 a)). The low voltage side (LV) is a layer or barrel winding with two times 23 turns and a rated total voltage of 500 V. The 10 kV high voltage side (HV) is a disk winding with two times 230 turns. The core of the transformer has a stepped cross section to approximate a circular shape (Fig. 6.6 b)). All relevant characteristics of the transformer are

stated in Table 6.1; the variable  $N$  represents the number of turns per winding. Appendix B.1 gives the test certificate of  $T_1$  as example.

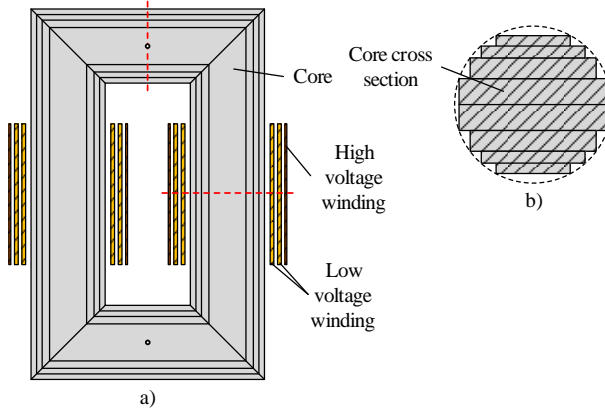


**Fig. 6.6:** a) Transformer setup, b) core cross section

**Table 6.1:** Properties of transformer  $T_1$  (see test certificate in Appendix B.1)

| Rated parameters        |                             | Short circuit test |                              |
|-------------------------|-----------------------------|--------------------|------------------------------|
| Low voltage side (LV):  | $U_{LV} = 500 \text{ V}$    | Apparent power:    | $S_{SC} = 6,394 \text{ kVA}$ |
|                         | $N_{LV} = 46$               |                    |                              |
| High voltage side (HV): | $U_{HV} = 10 \text{ kV}$    | Active power:      | $P_{SC} = 1,411 \text{ kW}$  |
|                         | $N_{HV} = 920$              |                    |                              |
| Rated power:            | $S_R = 200 \text{ kVA}$     | Current:           | $I_{SC} = 386.11 \text{ A}$  |
| Core mass:              | $m_{Core} = 583 \text{ kg}$ |                    |                              |
| Average induction:      | $\bar{B} = 1.65 \text{ T}$  |                    |                              |

The fact that the transformer  $T_1$  belongs to the Institute allows to perform no-load measurements in the Institute's lab. The no-load losses of the power transformer are measured similar to IEEE Std C57.12.91-2011 [66]. Fig. 6.7 sketches the measurement setup. A

power meter LMG 500 [10] is used to gauge the average active power  $P$  in 50 V steps of the terminal voltage  $U$  from 50 V to 500 V (RMS). A four quadrant amplifier which is remote controlled via PC works as power source. The total harmonic distortion (THD, equation (3.6)) of the excitation voltage never exceeds 1 %.

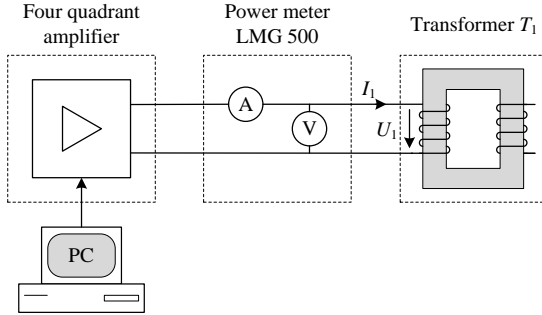


**Fig. 6.7:** Setup to measure no-load losses of transformer  $T_1$

Measured quantities are the power consumption of the core and the parasitic components (copper resistance  $R_{Cu}$  and the leakage inductance  $L_{\sigma 1}$ ) of the low voltage winding, see transformer sketch in Fig. 6.8.

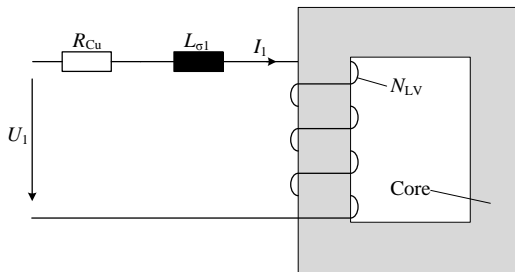


**Fig. 6.8:** Transformer with lumped parasitic elements ( $R_{Cu}$  and  $L_{\sigma 1}$ )

These components are approximated with  $4.73 \text{ m}\Omega$  and  $66.57 \text{ }\mu\text{H}$ . Equation (6.13) and (6.14) calculate both values using the results of a short circuit measurement (index “SC”) from the transformer test certificate stated in Table 6.1. Thereby, an equal separation of copper resistance  $R_{Cu}$  and the leakage inductance  $L_{\sigma 1}$  on high voltage and low voltage winding is assumed [23].

$$R_{Cu} = \frac{P_{sc}}{2 \cdot I_{sc}^2} \quad (6.13)$$

$$L_{\sigma 1} = \frac{\sqrt{S_{sc}^2 - P_{sc}^2}}{2 \cdot \omega \cdot I_{sc}^2} \quad (6.14)$$

The parasitic elements are required to compute the power consumption of the core  $P_{Core}$  using the excitation voltage  $U(t)$  and current  $I(t)$ .

$$P_{Core} = \frac{1}{T} \int_0^T (U(t) \cdot I(t) - I(t)^2 R_{Cu}) dt \quad (6.15)$$

Fig. 6.9 shows a comparison of measured and calculated power consumption. The maximum difference between both is less than 0.1 %. Thus, the influence of parasitic elements ( $R_{Cu}$  and  $L_{\sigma 1}$ ) on no-load losses can be neglected as explained in [48, section 1-6]. It is assumed that the measured no-load losses equal the core losses and therefore measured no-load losses are used for comparison to simulated losses from now on. The terms no-load losses and core losses are applied coequally.

In addition to measurement and calculation, the losses without load are estimated as function of the core mass  $m_{Core}$  and specific total loss  $P_S$  (compare section 4.1):

$$P_{estimated} = P_S(\hat{B}) \cdot m_{Core} \quad (6.16)$$

Fig. 6.9 also illustrates estimation results which differ significantly from the measurements which make the new core loss simulation method combining FE simulation and post-processing necessary.

The measured and estimated losses are compared using the building factor  $BF$  at rated voltage (6.17). As stated in [47, p. 452, 49, p. 111] that the  $BF$  is usually in a range of 1.15 to 1.4, but in the case of  $T_1$  a  $BF$  of 0.8735 is achieved. Reasons for this behavior could be the small size of the transformer and the low-cost electrical steel of the core. The mentioned  $BF$  range is determined for large three phase applications with cores made of high-quality steel.

$$BF = \frac{P_{measured}}{P_{estimated}} \quad (6.17)$$

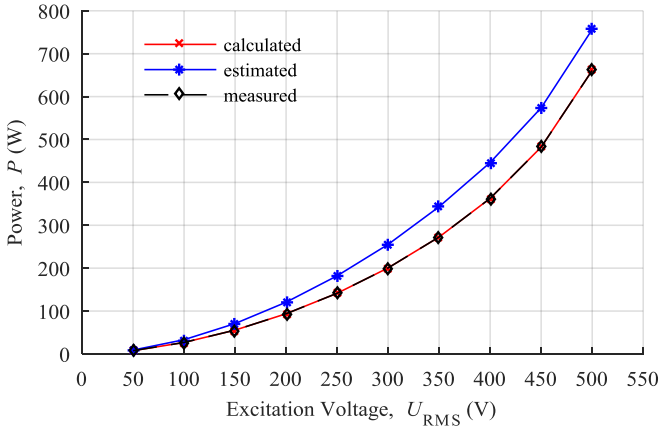


**Fig. 6.9:** Comparison of measured, calculated and estimated core losses

Nevertheless, the FE simulation of the transformer is performed in 3D. The electrical steel grade C165-35 is used in the transformer core. The three BH-curves express its magnetic properties (*maximum*, *inductive* and *resistive*) determined in chapter 4.3 and shown in Appendix B.2. A stacking factor of 96 % known from the electrical steel datasheet [64] describes the relation of steel, coating and air gaps between the steel sheets. The no-load losses are of interest and therefore, only the low voltage winding is part of the model setup. It is a barrel winding with twice 23 turns, 46 turns in total. But not every single turn is implemented in the model. However, based on the real setup, they are separated into one group of 12 and another of 11 turns. Both groups are realized as stranded windings, skin effect and proximity effect are not taken into consideration. All materials which are not essential for the electric and magnetic functionality of the transformer such as glass-fiber or reinforced plastics are ignored, since they do not influence the magnetic behavior of the core.

The 3D model of the power transformer is implemented in the FE Software ANSYS Maxwell 2016. Due to symmetry, only one eighth of the transformer needs to be modeled. An odd symmetry boundary, where the normal component of the magnetic field is zero, is defined for the vertical middle of the transformer. An even symmetry boundary, where the tangential component of the field is zero, is applied to the edges indicated by the red dashed lines in Fig. 6.6. A transient simulation in ten steps of the excitation voltage  $U$  from 50 V to 500 V is performed. A cosinusoidal excitation voltage produces a simulation time of 5 ms because the maximum flux density is reached at that point. Time steps of  $\Delta t = 100 \mu\text{s}$ , a nonlinear residual of  $10^{-7}$  and a fine mesh consisting of approximately

20,000 elements (Fig. 6.10 a)) are applied in the simulation. A further mesh refinement does not affect the loss calculation. Fig. 6.10 b) illustrates the flux density distribution for an excitation of 500 V and a *maximum* BH-curve. The results of a FE simulation relying on an *inductive* BH-curve are very similar. Hence, they are not shown additionally for convenience. Fig. 6.11 displays flux density (a)) and magnetic field (b)) distributions for the same excitation of 500 V based on a *resistive* BH-curve. All distributions are exported as text file for each excitation at a simulation time of 5 ms. The influence of different BH-curves on the flux density distribution is evident while comparing Fig. 6.10 b) and Fig. 6.11 b). Higher flux density values are generated in the L-joint region (compare subsection 2.1.1 ) of the core when a *resistive* BH-curve describes the steel's magnetic properties.

Flux density and magnetic field distributions are input for the post-processing algorithm as explicated in subsection 6.1. The core losses are determined for each BH-curve (*maximum*, *inductive* and *resistive*) separately with a MATLAB program. The loss calculation produces the results illustrated in Fig. 6.12. Measured and simulated loss curves are very similar, and differences can hardly be recognized. Therefore, the relative error is computed and shown in Fig. 6.13. Additionally, the relative error for estimated losses determined by equation (6.16) is illustrated here. The estimated losses differ most from the measured ones, between 14.4 % and 28.7 %.

However, flux distribution in a transformer core and a steel sheet sample are not uniform, especially inside joints of yoke and limb where magnetic flux turns by an angle of 90°. The change in magnetic path length along the width of the core cross section generates the inhomogeneous flux distribution in this parts of the core, which is implemented much better by a FE simulation. The combination of 3D simulation and post-processing generates a similar error of -2.9 % to 7.7 % for a *maximum* and an *inductive* BH-curve. The approach based on the *resistive* BH-curve delivers slightly different results with a deviation to measurements of -4.6 % to 6.8 %. While rated voltage is applied to the transformer, all FE simulations deliver an error between -2.9 % and -0.5 % which is assumed to be within an acceptable range. The investigation of core losses in transformer  $T_1$  besides the combination of FE simulation and post-processing algorithm based on a *maximum* BH-curve has been published previously in [74]. All further transformer investigations do not consider *inductive* and *resistive* BH-curves due to small differences in simulation results. The magnetic characteristics are described by a *maximum* BH-curve only, which is usually provided by electrical steel manufacturers.

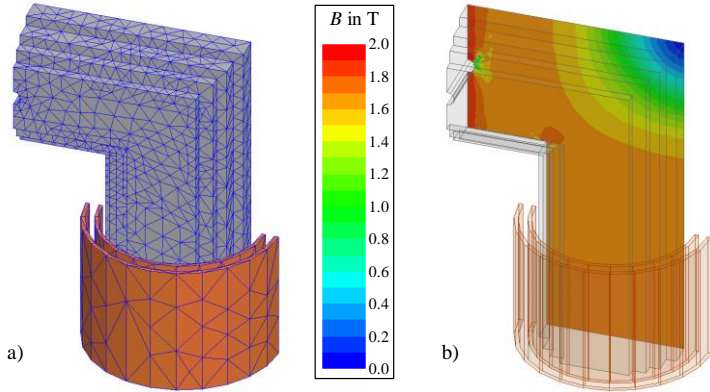


**Fig. 6.10:** Applied mesh (a) and flux density distribution (b) for 500 V (RMS) at  $t=5$  ms based on a *maximum* BH-curve of transformer  $T_1$

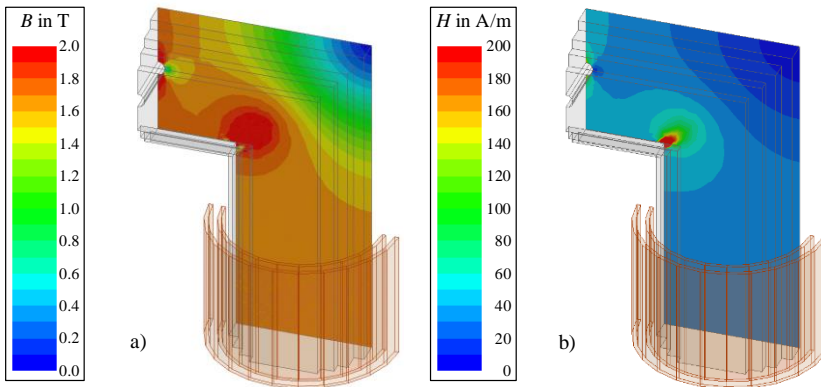


**Fig. 6.11:** Flux density distribution (a) and magnetic field distribution (b) for 500 V (RMS) at  $t=5$  ms based on a *resistive* BH-curve of transformer  $T_1$

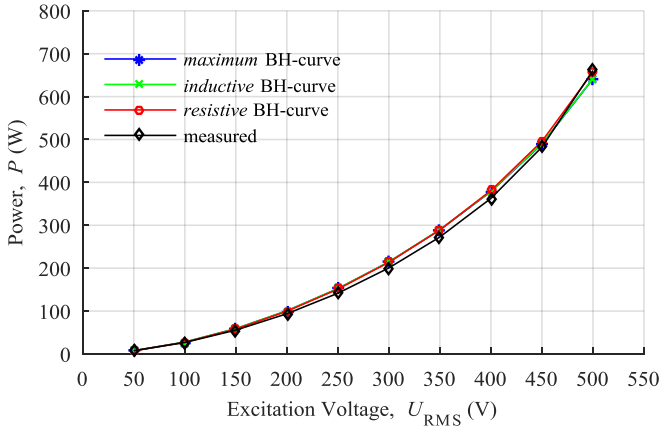


**Fig. 6.12:** Comparison of measured and simulated losses

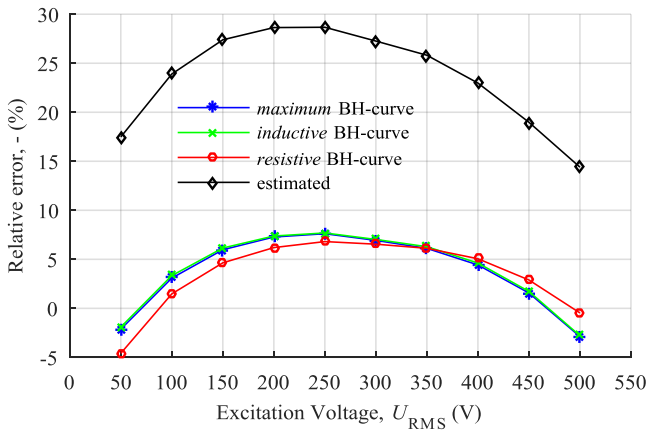


**Fig. 6.13:** Relative error in estimated and simulated core losses

### 6.3.1.2 Transformer $T_2$

The second investigated transformer has a very similar setup compared to the first one. Its winding system is separated equally on both limbs. The step lap method is applied to build the core of the same steel grade M165-35 with a circular core cross section and a stacking factor of 96 %. Table 6.2 shows the relevant parameters.

**Table 6.2:** Rated parameters of transformer  $T_2$

|                    |                                      |
|--------------------|--------------------------------------|
| Low voltage side:  | $U_{LV} = 720 \text{ V}$             |
|                    | $N_{LV} = 48$                        |
| High voltage side: | $U_{HV} = 2 \text{ kV}$              |
|                    | $N_{HV} = 133$                       |
| Rated power:       | $S_R = 240 \text{ kVA}$              |
| Core mass:         | $m_{\text{Core}} = 968.4 \text{ kg}$ |
| Average induction: | $\bar{B} = 1.54 \text{ T}$           |

All details of the core are provided by the manufacturer, but only the height of the low voltage winding  $h_N$  is given. The winding's cross section  $A_{Cu}$  is approximated with a current density  $J_1$  of 3 A/mm<sup>2</sup>, the number of turns  $N_{LV}$  and the rated current which is the ratio of rated power and voltage. Finally, the width of the low voltage winding  $w$  is calculated with its cross section  $A_{Cu}$  and its height  $h_N$  (6.18).

$$A_{Cu} = J_1 \cdot N_{LV} \cdot \frac{S_R}{U_{LV}} \quad (6.18)$$

$$\rightarrow w = \frac{A_{Cu}}{h_N}$$

Although the geometric dimensions of the low voltage winding are not known precisely, an FE simulation of transformer  $T_2$  is possible because the winding is for excitation only and the core is of major interest. A transient 3D FE simulation is performed for 5 ms with time steps of 100  $\mu\text{s}$ , a cosinusoidal excitation voltage and a residual of  $10^{-7}$ . Fig. 6.14 demonstrates the applied mesh of approximately 20,000 pyramids and the flux density distribution of an excitation voltage of 720 V (RMS).

The post-processing algorithm calculates the core losses (compare section 6.1). Table 6.3 gives the results of measured, simulated and estimated core losses (compare equation (6.16)).

**Table 6.3:** Comparison of measured, simulated and estimated core losses for  $T_2$ 

|                 | Test certificate | Simulation | Estimation |
|-----------------|------------------|------------|------------|
| Active power:   | 823 W            | 896.8 W    | 1,052.4 W  |
| Relative error: | --               | 9.0 %      | 27.9 %     |

All loss values are determined for an excitation voltage of 720 V because only information at rated voltage is available. A relative error of 9.0 % for the FE simulation combined with post-processing algorithm is achieved, whereas the loss estimation generates an error of 27.9 %. Although the simulation approach delivers a better result as the estimation, the deviation between simulation and measurement is still substantial.

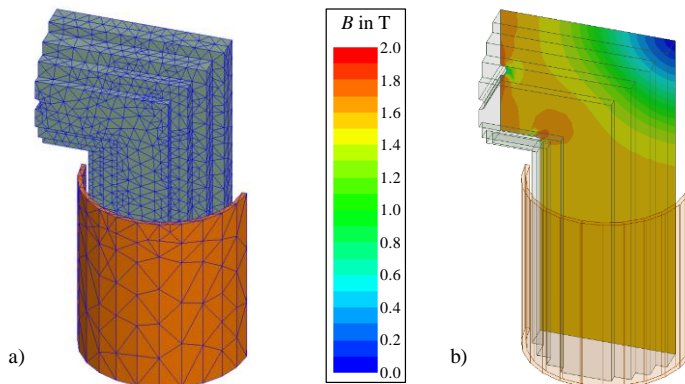


**Fig. 6.14:** Applied mesh (a) and flux density distribution (b) for 720 V (RMS) at  $t=5$  ms based on a *maximum* BH-curve of transformer  $T_2$

### 6.3.2 Three phase transformer

Next to the single phase transformers  $T_1$  and  $T_2$ , two three-phase applications are modeled, and their core losses are simulated in a similar way. The manufacturer provides detailed blueprints of the core construction for both transformers, but values for no-load losses are only available at rated voltage. Their core is built in step lap method with a circular cross section. The FE models equal one-quarter of the entire transformer due to symmetry. The

same boundary conditions are applied as explained in the model setup of transformer  $T_1$ . The core losses are simulated in the following.

### 6.3.2.1 Transformer $T_3$

The parameters in Table 6.4 characterize the transformer  $T_3$ . The core consists of the steel grade M165-35. Although all necessary information about the core is available, only the height of the high voltage winding is known. Similar to the transformer  $T_2$ , the cross section of the winding is estimated with its height and a current density of 3 A/mm<sup>2</sup>. All three coils of the high-voltage winding are delta connected. Again a *maximum* BH-curve describes the magnetic properties of the core, and a stacking factor of 97.5 % is applied which is provided by the transformer manufacturer.

**Table 6.4:** Rated parameters of transformer  $T_3$

|                    |  |
|--------------------|--|
| Low voltage side:  | $U_{LV} = 56 \text{ V}$                |
|                    | $N_{LV} = 4$                           |
| High voltage side: | $U_{HV} = 400 \text{ V}$               |
|                    | $N_{HV} = 29$                          |
| Rated power:       | $S_R = 698 \text{ kVA}$                |
| Core mass:         | $m_{\text{core}} = 2,393.2 \text{ kg}$ |
| Average induction: | $\bar{B} = 1.21 \text{ T}$             |

A transient 3D FE simulation is performed for 20 ms with time steps of 104.167  $\mu\text{s}$ . The excitation corresponds to three sinusoidal voltages with a phase shift of 120° and an amplitude of 400 V. Again a residual of  $10^{-7}$  is chosen, and a mesh of approximately 60,000 pyramids is generated. In contrast to a single phase transformer, the maximum flux density in all finite elements of the transformer core is not reached in one certain time step. Fig. 6.15 illustrates the flux density distribution for a zero crossing of the excitation voltage at each phase  $U$ ,  $V$  and  $W$ . The flux density distribution in the transformer core is a correlation of all three phases. To find the maximum in each finite element for post-processing, all distributions are exported for all time steps during a half period of the excitation voltage. The first 10 ms of simulation time are necessary to assure steady-state conditions, and during the time of 10 ms to 20 ms the flux density data is exported in 104.67  $\mu\text{s}$  steps. In contrast to the single phase applications  $T_1$  and  $T_2$  a longer simulation time of 10 ms is essential for three phase transformers to guaranty an absolute maximum flux density in each phase during this time.

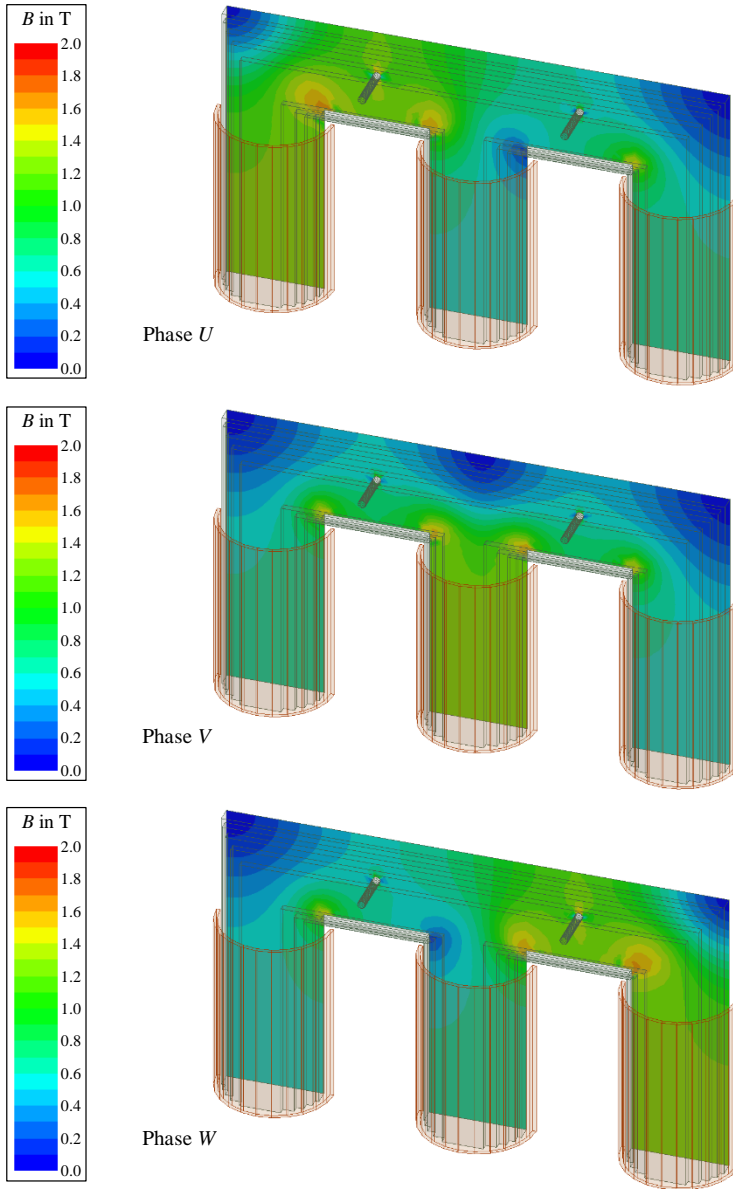


**Fig. 6.15:** Flux density distribution in transformer  $T_3$  with the maximum flux density in phase U, phase V and phase W

The ratio between time step and cycle time must be a multiple of three with respect to the three phase application. The absolute flux density maximum for each spatial axis  $x$ ,  $y$  and  $z$  are searched among all exported time steps. A MATLAB program creates a maximum flux density distribution, which is input to the post-processing algorithm as explained in section 6.1. Table 6.5 shows the results of FE simulation and post-processing including a comparison to measured and estimated core losses.

**Table 6.5:** Comparison of measured, simulated and estimated core losses for  $T_3$

|                 | Test certificate | Simulation | Estimation |
|-----------------|------------------|------------|------------|
| Active power:   | 1,247 W          | 1,408 W    | 1,535.4 W  |
| Relative error: | --               | 12.9 %     | 23.1 %     |

The FE simulation combined with post-processing algorithm creates a relative error of 12.9 %, while the loss estimation achieves an error of 23.1 %. The deviation of the simulation approach is smaller than the estimation, but there is still a major difference to measured losses.

### 6.3.2.2 Transformer $T_4$

The second three-phase transformer  $T_4$  is described by Table 6.6. Its setup is similar to transformer  $T_3$ , but a different electrical steel quality (M140-27) is used in the core. The transformer manufacturer provides an SST sample of the same steel grade, and a *maximum* BH-curve based on own measurements characterizes the magnetic behavior of the core. A stacking factor of 96.4 % is applied known from the transformer construction plan. The geometric dimensions of the low voltage winding are estimated as done for the transformers  $T_2$  and  $T_3$ . The low voltage winding is star connected and modeled for excitation.

**Table 6.6:** Rated parameters of transformer  $T_4$

|                    |                       |
|--------------------|-----------------------|
| Low voltage side:  | $U_{LV} = 400$ V      |
|                    | $N_{LV} = 11$         |
| High voltage side: | $U_{HV} = 21$ kV      |
|                    | $N_{HV} = 999$        |
| Rated power:       | $S_R = 3,500$ kVA     |
| Core mass:         | $m_{Core} = 3,040$ kg |
| Average induction: | $\bar{B} = 1.58$ T    |

Again a maximum flux density distribution is created by searching the maximum among exported flux density data described in the preceding subsection. The post-processing in MATLAB delivers the simulated core losses in Table 6.7 which compares the result to measured and simulated losses.

**Table 6.7:** Comparison of measured, simulated and estimated core losses for  $T_4$

|                 | Test certificate | Simulation | Estimation |
|-----------------|------------------|------------|------------|
| Active power:   | 2,663 W          | 2,308.7 W  | 2,509.5 W  |
| Relative error: | --               | -13.3 %    | -5.8 %     |

This time, the combination of FE simulation and post-processing algorithm is responsible for a relative error of -13.3 %, which is higher than the deviation created by the loss estimation of -5.8 %. Reasons for this behavior are outlined in the next section.

## 6.4 Discussion

Four different transformers are investigated with respect to their core losses which are simulated and compared to measured data. The simulation results of the first transformer  $T_1$  shows good agreement with measurements, especially at rated voltage a small relative error of -2.9 % is achieved. There are simplifications in the transformer modeling like the assumed magnetic isotropy of the core and no step lap stacking which decrease simulated losses in comparison to measurements. Nevertheless, the simulated losses of the transformer  $T_2$  to  $T_4$  deliver a deviation of -13.3 % to 12.9 %, which cannot be explained by model simplifications. After discussing the results of the transformers  $T_2$  to  $T_4$  with the manufacturer, it turned out, that only the used steel grade is known, but their manufacturer cannot be clearly identified. Although the provided steel sheet samples belong to the same steel quality utilized in the core, their manufacturer could be different. Only in the case of transformer  $T_1$ , grade and manufacturer match in sample and core. However, various steel producers cause different magnetic properties, even if the electrical steel belongs to the same standardized grade (see section 4.1). Thus, one reason for the erroneous simulation results is the difference in magnetic properties of investigated SST sample and electrical steel of the transformer core.

Further reasons for differences between measurement and simulation can be found in the measurement device, the SST according to IEC 60404-3 [70]. The magnetic path length of SST changes with polarization amplitude leading to an error in measuring the magnetic field strength [11]. Systematic errors in the magnetic field and flux density measurements are discussed in [20]. Another important aspect is the variance of magnetic properties along a steel sheet coil [4]. In this work a 25 cm x 25 cm steel sample per steel grade is used for SST measurements. Its properties describe the magnetic behavior of the entire transformer core. Hence, there is uncertainty in modeling the magnetic properties. Appendix B.2 gives used the BH- and  $P_s$ -curves.

Despite the deviations of simulation and measurement caused by uncertain steel characteristics, the FE simulation combined with post-processing loss calculation offers the possibility to determine core losses in power transformers without experience achieved from identically constructed transformers. This approach could be helpful when there are changes in core design or core material.



# 7 Core optimization

Nowadays, transformer cores consist of one electrical steel sheet quality. Its magnetic properties determine the power consumption of the transformer at no-load conditions. Chapter 6 introduces a combination of FE simulation and post-processing algorithm for calculating transformer core losses. Based on this loss simulation method, mixed cores made of two different electrical steel grades are investigated in this chapter. The goal of a mixed transformer core design is to reach same production cost but fewer core losses compared to a transformer with a core made of only one steel grade in the same application. The selection of appropriate steel quality combinations is explained and applied to a modeled power transformer. Finally, the core loss reduction caused by a mixed core design is investigated under economical aspects. The concept of a mixed core design was previously introduced in [73].

## 7.1 Mixed core design without change in geometry

The influence of two carefully chosen steel grades on the transformer's core losses is of interest. The design of transformer  $T_1$  analyzed in the preceding chapter is selected as the basis for the following studies. Its geometry remains unchanged in this section.

### 7.1.1 Combination of different steel grades

The specific total loss describes the electrical steel's quality. Different steel grades are categorized by the specific total loss as explained in 4.1. Table 7.2 shows a range of different electrical steel qualities. The manufacturer ThyssenKrupp provides detailed magnetic properties like *maximum* BH-curve and  $P_s$ -curve. An interpolation of the  $P_s$ -curve for each electrical steel grade determines the specific total loss values at a maximum polarization of 1.7 T. The steel grades are sorted based on this value, which could cause a contrary order compared to the steel names (see  $s = 8$ ). The maximum specific total loss value as part of the steel name is only an upper limit. The real specific total loss is usually significantly lower leading to this new order of the listed electrical steel grades.

**Table 7.1:** Electrical steel grade specifications

| Number $s$ | Name    | Specific total loss $P_S$ in W/kg @ $\dot{J}=1.7$ T | Specific costs $C_S$ in €/kg |
|------------|---------|---|------------------------------|
| 1          | C103-27 | 1.000   | 3.45                         |
| 2          | C110-23 | 1.064   | 3.34                         |
| 3          | C110-27 | 1.073   | 3.32                         |
| 4          | C120-23 | 1.141   | 3.21                         |
| 5          | C120-27 | 1.160   | 3.18                         |
| 6          | C130-30 | 1.205   | 3.10                         |
| 7          | C130-27 | 1.210   | 3.09                         |
| 8          | C127-23 | 1.235   | 3.05                         |
| 9          | C140-30 | 1.264   | <b>3.00</b>                  |
| 10         | C150-30 | 1.323   | <b>2.90</b>                  |
| 11         | C140-35 | 1.330   | 2.89                         |
| 12         | C150-35 | 1.397   | 2.75                         |
| 13         | C165-35 | 1.469   | <b>2.60</b>                  |

Fig. 7.1 illustrates an example of a mixed core setup and its combined core cross section. One half of the cross section is sufficient due to symmetry. It is separated into two continuous parts, the area  $A_1$  made of the better steel grade  $P_{S1}$  and area  $A_2$  where the worse steel grade  $P_{S2}$  is utilized. All parts cover the magnetic path length  $l_{Fe}$ . They are parallel connected in an equivalent magnetic circuit of the mixed core.

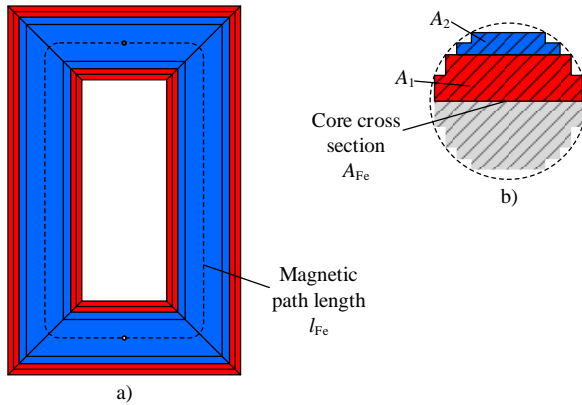


**Fig. 7.1:** a) Mixed core setup, b) Core cross section of a mixed core design

The relationship of better steel grade mass  $m_{Ps1}$  to the entire core mass  $m_{Core}$  defines the grade ratio of the better steel grade  $a$  (7.1). Equation (7.1) also describes the grade ratio of the worse steel grade  $1-a$ :

$$\begin{aligned} a &= \frac{m_{Ps1}}{m_{Core}} \\ 1-a &= \frac{m_{Ps2}}{m_{Core}} \end{aligned} \quad (7.1)$$

The mixed core manufacturing cost ( $CMC_{12}$ ) must equal the reference core manufacturing cost ( $CMC_3$ ) (7.2). Labor cost for cutting sheets and producing the core is already part of the specific price per mass  $C_{S1-3}$  for each steel grade. The cost  $CMC_3$  for the reference core are calculated with the price of the steel grade  $C_{S3}$  and the core mass. The mixed core cost  $CMC_{12}$  is computed with the grade ratio  $a$ , the specific price  $C_{S1}$  of the better steel grade  $P_{S1}$  and the worse steel quality symbolized by  $P_{S2}$  and  $C_{S2}$ . The grade ratio  $a$  can now be computed in (7.2) and relies only on the specific prices of the involved steel qualities.

$$\begin{aligned} CMC_3 &= CMC_{12} = CMC \\ m_{Core} \cdot C_{S3} &= m_{Core} [a \cdot C_{S1} + (1-a) \cdot C_{S2}] \\ \rightarrow \quad a &= \frac{C_{S3} - C_{S2}}{C_{S1} - C_{S2}} = \frac{m_{Ps1}}{m_{Core}} \end{aligned} \quad (7.2)$$

Table 7.1 gives the specific price of each steel grade. It is difficult to get information about prices because electrical steel and transformer manufacturer do not provide all details. Reasons could be individual price negotiations and the fact that electrical steel belongs to worldwide traded goods. Thus, only specific prices of three steel grades are available, indicated by bold digits in Table 7.1. All other specific price values are an inter- or extrapolation of a linear curve fit between specific losses and the known specific prices. This specific price determination is erroneous but still realistic. Without these assumptions, an investigation of mixed core designs would not be possible.

The losses of the mixed core  $P_{12}$  are approximated by equation (7.3):

$$P_{12} = m_{Core} (a \cdot P_{S1}(\hat{B}) + (1-a) \cdot P_{S2}(\hat{B})) \quad (7.3)$$

The flux density  $\hat{B}$  results from the transformer's excitation voltage (compare equation (5.2);  $\hat{B}_{T1}=1.65$  T) and is input for both specific total loss curve fits  $P_{S1}(\hat{B})$  and  $P_{S2}(\hat{B})$  which are based on  $P_S$ -curves provided by ThyssenKrupp. A  $P_S$ -curve defines a relationship of specific total loss and polarization amplitude which is transformed to a function of flux density by equation (4.5). The mixed core losses  $P_{12}$  are compared to the losses of the reference core  $P_3$  which are estimated as follows:

$$P_3 = m_{\text{Core}} \left( P_{S3}(\hat{B}) \right). \quad (7.4)$$

The loss ratio  $p$  of mixed core losses  $P_{12}$  and reference core losses  $P_3$  indicate whether an increase or a decrease of losses is achieved by the combination of two different steel grades.

$$p = \frac{P_3(m_{\text{Core}}, \hat{B}, C_3) - P_{12}(m_{\text{Core}}, a, \hat{B}, C_1, C_2)}{P_3(m_{\text{Core}}, \hat{B}, C_3)} \quad (7.5)$$

Datasets of 13 different steel grades produce 286 possible combinations (7.6).

$$\sum_{s=2}^{12} \underbrace{(s-1)}_{P_{S1}} \cdot \underbrace{(12-s+1)}_{P_{S2}} = 286 \quad (7.6)$$

The variable  $s$  gives the number of each possible steel grade used in the reference core (Table 7.1). The best grade ( $s = 1$ ) and the worst grade ( $s = 13$ ) could not be applied to the reference core. The equal cost condition for mixed and reference core cannot be fulfilled in these cases. The first term in equation (7.6) stands for better steel grades  $P_{S1}$ , whereas the second one defines the number of worse steel grades  $P_{S2}$ . Both choices depend on the selected reference steel grade  $P_{S3}$ . A MATLAB program calculates the mixed and reference core losses for all 286 steel grade combinations. Those combinations with a loss decrease in the mixed core design of more than 1 % are selected and sorted regarding their core manufacturing cost. Finally, steel combinations with the highest loss reduction per manufacturing cost level are selected. Eight different steel grade combinations satisfy these requirements (Table 7.2). The number and kind of steel grade combinations strongly depend on the specific prices of the steel grades. A change in price would cause different steel grade combinations directly because their selection relies on the manufacturing cost of the transformer core (equation (7.2)). Table 7.2 gives information about core manufacturing cost and the grade ratio  $a$ . The first steel combination for a mixed core design with the best loss ratio  $p$  is the most expensive one. However, the second combination belongs

to a transformer with low manufacturing cost. On the other hand, the grade ratio  $a$  ranges between 14.64 % and 94.74 % with no relation to the loss ratio  $p$ . There is neither a dependency to manufacturing cost nor the grade ratio.

**Table 7.2:** Selected steel grade combinations for a mixed core design

| Combination | Name $P_{S1}$ | Name $P_{S2}$ | Name $P_{S3}$ | Core manufacturing costs $CMC$ (€) | Grade ratio $a$ (%) | Loss ratio $p$ (%) |
|-------------|---------------|---------------|---------------|------------------------------------|---------------------|--------------------|
| 1           | C110-23       | C127-23       | C110-27       | 1938                               | 94.74               | 4.21               |
| 2           | C127-23       | C165-35       | C140-35       | 1682                               | 63.59               | 3.56               |
| 3           | C110-23       | C127-23       | C130-27       | 1802                               | 14.62               | 3.22               |
| 4           | C110-23       | C127-23       | C130-30       | 1807                               | 17.54               | 3.14               |
| 5           | C127-23       | C165-35       | C140-30       | 1749                               | 89.06               | 3.05               |
| 6           | C127-23       | C165-35       | C150-30       | 1691                               | 66.79               | 2.62               |
| 7           | C110-23       | C127-23       | C120-27       | 1852                               | 43.86               | 2.32               |
| 8           | C127-23       | C165-35       | C150-35       | 1602                               | 32.94               | 1.81               |

## 7.1.2 Core loss simulation

Based on the steel grade selection stated in Table 7.2, core losses are simulated with the FE model of transformer  $T_1$  introduced in subsection 6.3.1.1. Similar to the analytic calculation of the loss ratio  $p$ , a mixed and a reference core design are modeled, and the core losses are calculated via post-processing for each combination. Fig. 7.2 shows a comparison of loss ratio  $p$  determined with the analytic approach and the combination of FE simulation plus post-processing algorithm. The FE approach delivers a higher loss ratio because an iteration adapts flux density in different steel grade parts and therefore an energetic equilibrium is reached leading to lower losses. Hence, the loss ratio  $p$  based on the FE approach is more realistic.

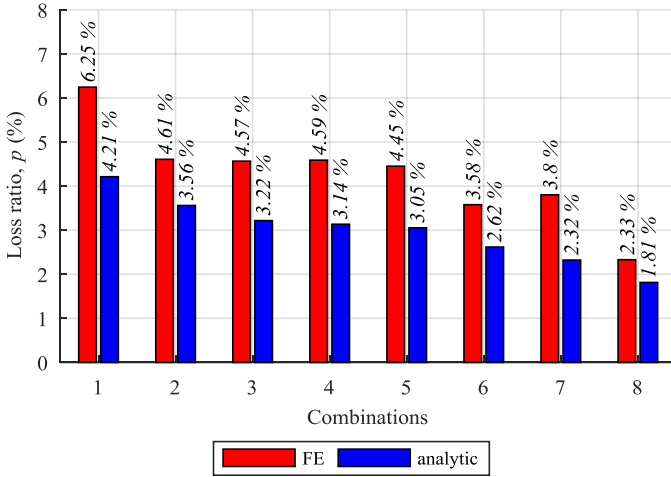


**Fig. 7.2:** Comparison of loss ratio  $p$  for FE simulation and analytic approach

### 7.1.3 Load loss approximation

The core losses represent the no-load losses of a transformer which are generated whenever the transformer is energized. In contrast to that, the load current  $I_{\text{load}}$  is responsible for transformer load losses, which are separated into three categories:

- Resistive loss generated by the parasitic resistance of the windings
- Eddy current loss in windings
- Eddy current loss in tank and auxiliary metal constructions

The investigated transformer type is an air cooled core setup and a tank is not part of it. Furthermore, the losses in the coil conductors as the sum of resistive and eddy current loss contribute the majority of the load losses [49, pp. 54]. Equation (7.7) delivers a good approximation of load losses  $P_k$ .

$$P_k = I_{\text{load}}^2 \cdot R_{\text{AC}} \quad (7.7)$$

The AC resistance of the windings  $R_{\text{AC}}$  already contains eddy effects and represents their losses. It is calculated in subsection 6.3.1.1 with a short circuit test of the transformer  $T_1$ .

An AC resistance of 9.46 mΩ is computed which represents low and high voltage winding. Equation (7.7) calculates the load losses of 1,514.35 W whereas the rated current of 400 A is applied as load current  $I_{\text{load}}$ . Otherwise, the AC resistance can be calculated analytically [21] which implies detailed knowledge about the winding setup and is rather complex. Thus, the approximation of AC resistance based on a short circuit test is used in this work.

### 7.1.4 Cost consideration

Until now only the impact of a mixed core design on the no-load losses is investigated. The no-load losses produce cost over the entire lifetime of a power transformer which is an interesting criterion for the comparison of mixed and reference core design. The entire cost including purchase (initial cost:  $IC$ ) and lifecycle cost are the total cost of ownership ( $TCO$ ) [24].

$$\begin{aligned} TCO &= IC + A \cdot P_0 + X \cdot P_k \\ &= CMC + WMC + A \cdot P_0 + X \cdot P_k \end{aligned} \quad (7.8)$$

The initial cost  $IC$  is the sum of winding manufacturing cost  $WMC$  and core manufacturing cost  $CMC$  (equation (7.2)). The geometric dimensions of the modeled power transformer remain unchanged, and the coil design is the same for all mixed core combinations. The constant  $WMC$  are estimated with the copper mass of the coils  $m_{\text{Cu}}$  and the specific price of copper  $C_{\text{Cu}}$  [54, pp 36]. Equation (7.9) delivers the  $WMC$  for transformer  $T_1$ , with a  $m_{\text{Cu}}$  of 160 kg and  $C_{\text{Cu}}$  of 5 €/kg. A margin of 25 % dedicates expenses for labor.

$$WMC = m_{\text{Cu}} \cdot C_{\text{Cu}} \cdot 1.25 = 160 \text{ kg} \cdot 5.0 \frac{\text{€}}{\text{kg}} \cdot 1.25 = 1000 \text{ €} \quad (7.9)$$

The second component of the  $TCO$  calculation represents cost due to no-load loss  $P_0$ . The variable  $A$  denotes the assigned cost of no-load losses per watt and is defined as follows:

$$A = oh \cdot C_{y/2} \cdot \frac{1 - \left(\frac{1}{1+r}\right)^y}{r} \quad (7.10)$$

A discount rate for the investment per year (“cost of money”)  $r$  of 5 %, an expected lifetime of the transformer  $y$  of 40 years and transformer operating hours  $oh$  of 8,760 h

per year are assumed. Equation (7.11) gives the cost of energy at the mid-life of the transformer  $C_{y/2}$ .

$$C_{y/2} = \frac{C + (C \cdot (1+z)^y)}{2} \quad (7.11)$$

The initial cost of energy  $C$  is chosen to be 0.06 €/ kWh and  $z$  gives the annual increase of energy price of 2 % [24]. The last term of equation (7.8) represents the influence of load losses  $P_k$ , where  $X$  are their assigned cost per watt (7.12).

$$X = k^2 \cdot g \cdot C_{y/2} \cdot \frac{1 - \left(\frac{1}{1+r}\right)^y}{r} \quad (7.12)$$

with

$$k = \frac{\bar{P}_{\text{load}}}{P_R}$$

The calculation of  $X$  is very similar to  $A$ , despite the variable  $k$  which describes the ratio of average loading  $\bar{P}_{\text{load}}$  and rated active power  $P_R$  of the transformer during its lifetime. An average loading of  $k = 1$  is assumed in this work [24].

Fig. 7.3 demonstrates the  $TCO$  of the eight mixed and reference core designs introduced in Table 7.2 relying on the FE simulation. The brighter parts of each bar symbolize the core manufacturing cost while the darker sections of each column in Fig. 7.3 stand for costs created by no-load losses. The parameter  $c$  indicates the cost ratio of the mixed core approach compared to each reference core:

$$c = \frac{TCO_{\text{reference core}} - TCO_{\text{mixed core}}}{TCO_{\text{reference core}}} \quad (7.13)$$

Although combination 1 requires the highest core manufacturing cost, it shows the lowest  $TCO$  over the lifetime of the transformer. As  $CMC$  are below 10 % of the  $TCO$ , the major part of  $TCO$  is created by life cycle costs which explain why the combination 1 (Table 7.2) is the most cost effective solution in this scenario. Costs caused by no-load losses are the only cost component varying between mixed and reference core design, which is the reason why cost ratio  $c$  and loss ratio  $p$  follow the same trend, but  $c$  is smaller than  $p$ .

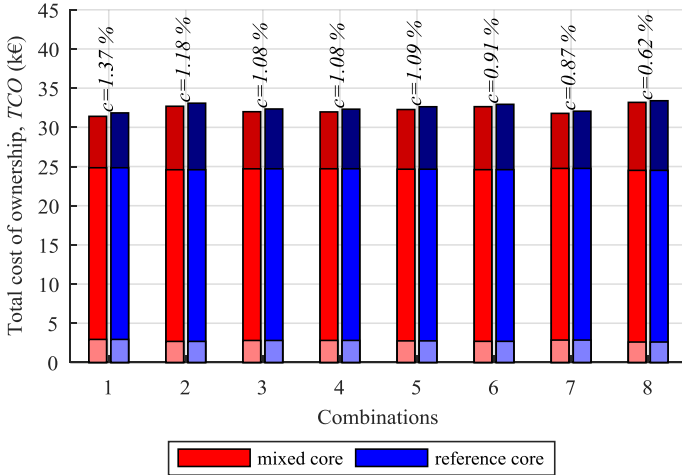


**Fig. 7.3:** TCO of mixed and reference core design

## 7.2 Mixed core design with change in geometry

Up to now, mixed core designs made of two different steel grades are investigated, but the transformer excitation is not changed. This section introduces an adaptation of the average flux density induced by the excitation voltage. The excitation change could be realized by a modification of the terminal voltage, the number of turns in the windings or the core cross section of the transformer based on Faraday's law. Only the last option is useful and leads to an adaptation of the transformer geometry.

### 7.2.1 Analytic approximation of TCO

All 286 different steel grade combinations (compare equation (7.6)) are calculated for a flux density range from 0.05 T to 1.95 T in 0.05 T steps. The maximum loss ratio  $p_{\max}$  is determined for each flux density value; Fig. 7.4 displays the results. The highest influence of a mixed core design on the maximum loss ratio  $p_{\max}$  can be found for small excitations. Its minimum is reached at 1.7 T followed by an increase of  $p_{\max}$  for greater flux densities. The reason for this minimum could be the steel grade characterization at a flux density value of 1.7 T. The maximum loss ratio is not an applicable criterion to find appropriate

steel grade combinations because it does not provide any further information. It only gives a comparison of core losses but does not tell anything about total losses and so about costs.

The *TCO* is useful to select suitable mixed core designs due to its general economic message. As already explained in equation (7.8), the *TCO* is a sum of initial and life cycle costs. The initial cost represents expenses for manufacturing core and coils which are both affected by a change in core cross section.

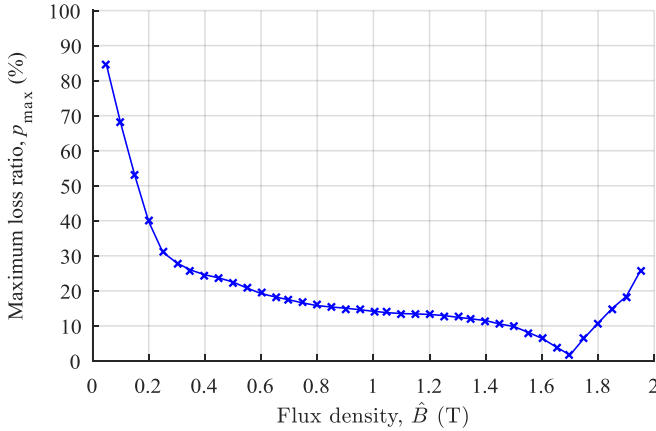


**Fig. 7.4:** Relationship of maximum loss ratio  $p_{\max}$  and excitation flux density

At first, an excitation ratio  $b$  is defined describing the relationship of rated flux density  $\hat{B}_{\text{rated}}$  and the adapted flux density  $\hat{B}_{\text{adpt}}$ , which is reciprocally proportional to the ratio of the core cross:

$$b = \frac{\hat{B}_{\text{adpt}}}{\hat{B}_{\text{rated}}} = \frac{A_{\text{Fe, rated}}}{A_{\text{Fe, adpt}}} \stackrel{\text{single phase}}{=} \frac{m_{\text{Core, rated}}}{m_{\text{Core, adpt}}} . \quad (7.14)$$

In a second step, the excitation ratio  $b$  is used to compute the adapted core manufacturing cost  $CMC_{\text{adpt}, 3}$  for the reference transformer (7.15). Core mass  $m_{\text{Core}}$  and core cross section  $A_{\text{Fe}}$  are proportional to each other due to the single phase setup (compare equation (7.14)).

$$CMC_{\text{adpt}, 3} = C_{S3} \frac{m_{\text{Core, rated}}}{b} \quad (7.15)$$

Similar to (7.2), the manufacturing cost of the mixed core design  $CMC_{\text{adpt}, 12}$  can be calculated as follows:

$$\begin{aligned}
 CMC_{\text{adpt}, 3} &= CMC_{\text{adpt}, 12} \\
 \frac{m_{\text{Core, rated}}}{b} C_{S3} &= \frac{m_{\text{Core, rated}}}{b} [a \cdot C_{S1} + (1-a) \cdot C_{S2}] \\
 \rightarrow \quad a &= \frac{C_{S3} - C_{S2}}{C_{S1} - C_{S2}}
 \end{aligned} \tag{7.16}$$

The costs for mixed and reference core must still be equal and the definition of the grade ratio  $a$  remains the same compared to section 7.1.

There is no difference in winding manufacturing costs  $WMC$  of mixed and reference design due to their identical geometry. However, a modification of core cross section also changes its peripheral length  $S$ , while a circular cross section of the radius  $r_{\text{rated/adpt}}$  is assumed:

$$b = \frac{A_{\text{Core, rated}}}{A_{\text{Core, adpt}}} = \frac{r_{\text{rated}}^2 \cdot \pi}{r_{\text{adpt}}^2 \cdot \pi} \rightarrow \frac{S_{\text{rated}}}{S_{\text{adpt}}} = \frac{2\pi \cdot r_{\text{rated}}}{2\pi \cdot r_{\text{adpt}}} = \sqrt{b} . \tag{7.17}$$

The copper mass  $m_{\text{Cu}}$  of the windings is proportional dependent on the peripheral length  $S$ . The cross section of the used copper wire of the windings remains unchanged because the rated power of all transformer designs is the same. Hence, the adapted winding manufacturing cost relies on the square root of the excitation ratio  $b$ :

$$WMC_{\text{adpt}} = C_{\text{Cu}} \cdot 1.25 \cdot \frac{m_{\text{Cu}}}{\sqrt{b}} . \tag{7.18}$$

Again, a factor of 1.25 approximates the expenses for labor.

Next to the initial cost of the transformer, the no-load losses affected by a change in geometry need to be discussed. The adapted no-load losses for reference and mixed core design ( $P_{3, \text{adpt}}$  and  $P_{12, \text{adpt}}$ ) are estimated with the specific total loss of the applied steel grades leading to the following descriptions (compare subsection 7.1.1):

$$P_{3, \text{adpt}} = \frac{m_{\text{Core, adpt}}}{b} (P_{S3}(\hat{B})) \tag{7.19}$$

and

$$P_{12, \text{adpt}} = \frac{m_{\text{Core, adpt}}}{b} \left( a \cdot P_{S1}(\hat{B}) + (1-a) \cdot P_{S2}(\hat{B}) \right). \quad (7.20)$$

Similar to the initial cost of the windings, the adapted load losses  $P_{k, \text{adpt}}$  of mixed and reference setup are equal. They depend mainly on the AC resistance of the windings which is supposed to be proportional to peripheral length  $S$  of the core cross section (7.17) leading to the relationship:

$$R_{\text{AC, adpt}} = R_{\text{AC, rated}} \frac{S_{\text{adpt}}}{S_{\text{rated}}} = \frac{R_{\text{AC, rated}}}{\sqrt{b}}. \quad (7.21)$$

Finally, the adapted load losses  $P_{k, \text{adpt}}$  are computed with the rated load current  $I_{\text{load}}$  in equation (7.22).

$$P_{k, \text{adpt}} = I_{\text{load}}^2 \cdot \frac{R_{\text{AC, rated}}}{\sqrt{b}} \quad (7.22)$$

All components of the  $TCO$  can now be approximated as a function of chosen steel grades and adapted transformer geometry, which is carried out in the next section.

### 7.2.2 Selection of different steel grades based on $TCO$

The  $TCO$  is computed for the entire flux density range and all possible steel quality combinations as used for the maximum loss ratio determination in Fig. 7.4. In this first approach, core losses are approximated analytically as introduced in subsection 7.1.1. Fig. 7.5 illustrates the  $TCO$  as a function of the  $IC$  for the best economic transformer designs which are indicated by values around the minimum of the  $TCO$  curve. This method is state of the art and explained in [24]. The different designs are named with letters and sorted by the loss ratio  $p$  stated in Table 7.3.

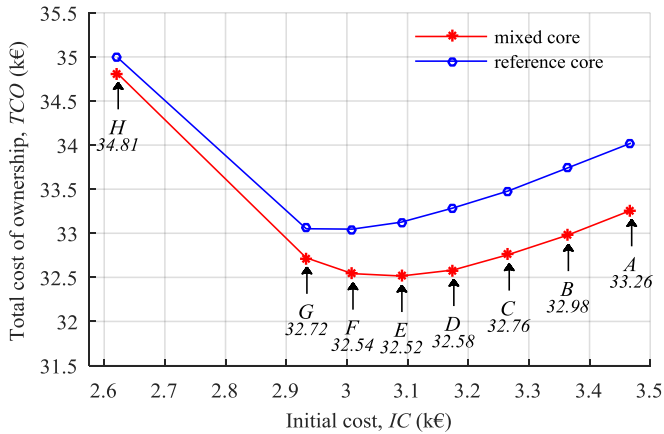


**Fig. 7.5:** TCO of mixed core and reference core design as function of IC based on the analytic approach

**Table 7.3:** Selected mixed core designs

| Design | Name $P_{S1}$ | Name $P_{S2}$ | Name $P_{S3}$ | Excitation ratio $b$ | Grade ratio $a$ (%) | Loss ratio $p$ (%) |
|--------|---------------|---------------|---------------|----------------------|---------------------|--------------------|
| A      | C110-23       | C127-23       | C110-27       | 0.82                 | 94.74               | 11.99              |
| B      | C110-23       | C127-23       | C110-27       | 0.85                 | 94.74               | 11.52              |
| C      | C110-23       | C127-23       | C110-27       | 0.88                 | 94.74               | 10.52              |
| D      | C110-23       | C127-23       | C110-27       | 0.91                 | 94.74               | 9.83               |
| E      | C110-23       | C127-23       | C110-27       | 0.94                 | 94.74               | 8.19               |
| F      | C110-23       | C127-23       | C110-27       | 0.97                 | 94.74               | 6.46               |
| G      | C110-23       | C127-23       | C110-27       | 1.00                 | 94.74               | 4.00               |
| H      | C103-27       | C165-35       | C150-30       | 1.03                 | 35.40               | 1.68               |

This table also gives further information about applied steel grade combinations, excitation ratio  $b$  and grade ratio  $a$ . The transformer designs A to G consist of the same steel grade combinations and the same grade ratio  $a$ . Despite their change in geometry represented by the excitation ratio, they equal combination 1 of the previous investigation with

a constant excitation. A different combination of steel qualities is only found for the design *H*. Similar to the preceding section 7.2.1, the core losses are determined based on FE simulation of each transformer design followed by post-processing operations.

### 7.2.3 Validation with FE simulation

The selected options for transformer designs *A* to *H* in Table 7.3 are modeled in the FE software, and their core losses are calculated, delivering more accurate results than the analytic approach demonstrated by loss ratio comparison in Fig. 7.6. The core losses generate life cycle costs and therefore an inaccuracy in loss determination also affects the value of the *TCO* to choose the most appropriate transformer design.

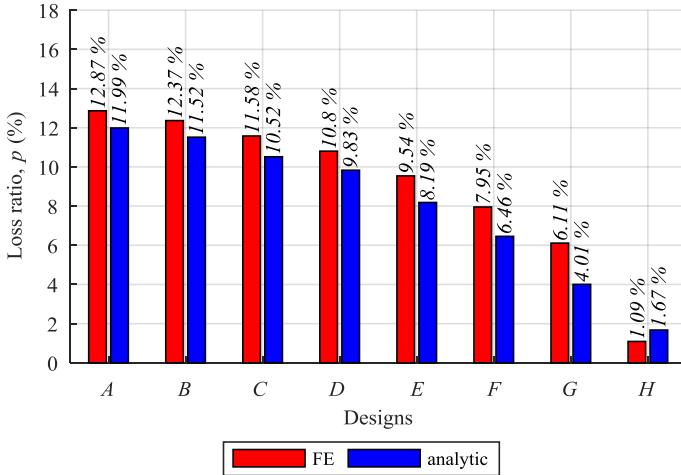


**Fig. 7.6:** Comparison of loss ratio  $p$  for FE simulation and analytic approach

The FE simulation usually shows a higher loss ratio  $p$  despite for the design *H*. Although there are deviations between the analytic and FE approach to determine core losses, the selected designs *A* to *H* still cover the minimum *TCO* as demonstrated in Fig. 7.7.

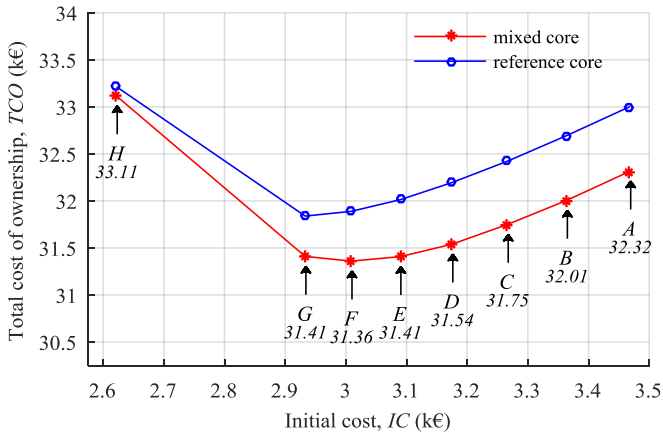


**Fig. 7.7:** TCO of mixed core and reference core design based on FE approach

The best solution is design *F* with the lowest TCO and a loss ratio  $p$  of 9.54 %. It is close to setup *G* and *E* due to their almost identical designs despite a small difference in excitation ratio of  $\pm 3$  % (compare Table 7.3). Initial and life cycle costs contribute differently to the TCO depending on each design.

Fig. 7.8 displays the TCO of reference and mixed core designs for all eight options. The brighter parts of each bar represent the IC which are below 10 % of the TCO. The major part of them indicated by the middle section of each column are created by load losses whereas the upper darker parts symbolize no-load loss costs. The design options *A* to *E* deliver lower costs generated by no-load losses than the best solution *F*. However, their excitation ratio is lower which represents a bigger core cross section and therefore more electrical steel in the core and more copper in the windings are required for these setups. Both provoke an increase in IC and costs produced by load losses which explain the higher TCO of options *A* to *E*. On the other hand, the solutions *G* and *H* have higher excitation ratios leading to lower IC and load loss related costs. However, these two designs show an increase in no-load losses which is the reason for a rise of the TCO. Finally, the TCO is a superposition of geometry and material corresponding costs. The parameter  $c$  in Fig. 7.8 indicates the cost ratio of the mixed core approach compared to each reference setup. Although the cost ratios for the designs *A* to *E* are higher, the design *F* is the most cost effective solution of all. Nevertheless, the TCO is superior criterion concerning all eight options. Although the cost ratio value of design *F* is only 1.66 %, this percentage equals almost 10 % of the initial cost of the transformer. The new mixed core design offers

the possibility to save approximately 10 % of the purchase price over the lifetime of the transformer.

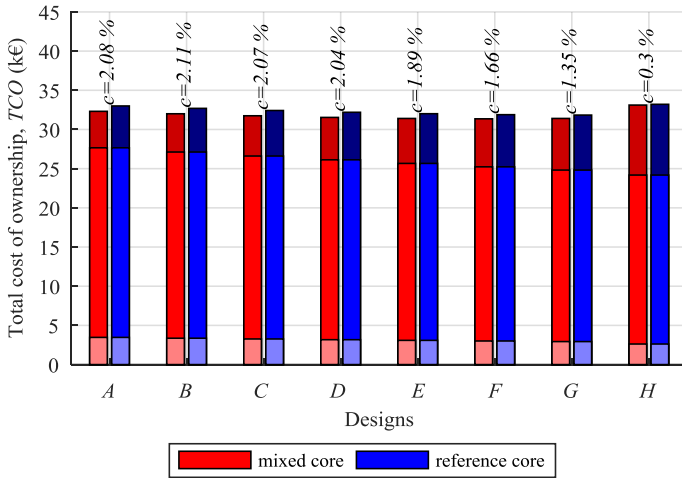


**Fig. 7.8:** TCO of mixed and reference core design

## 8 Conclusion

The simulation of core losses of power transformers and the investigation of new core design concepts are the main focus of this work. The core loss determination combines a FE simulation with a post-processing loss calculation. It is based on a detailed FE model of the entire active part of the transformer in ANSYS Maxwell 2016 and a post-processing algorithm implemented in MATLAB. Four different transformers are analyzed by comparing their simulated and measured core losses. Detailed blueprints, test certificates and a steel sheet sample of the material used in the core for each transformer were provided by the manufacturer. Nevertheless, there was an uncertainty in comparability of provided samples and electrical steel used for core manufacturing; only for one single phase transformer, sample and core material could be approved. In case of this single phase transformer, simulated and measured losses show a good agreement. Hence, the combination of FE simulation and post-processing loss calculation offers the possibility to determine core losses in power transformers during design stage. Based on this approach, the effect of a mixed core design on no-load losses is investigated. A mixed core consists of two different steel grades whereas a reference core for comparison is made of only one steel quality. However, the core manufacturing cost for both are the same which defines the steel grade selection and their ratio in the entire core. Next to the combination of different steel qualities, the transformer excitation by means of the average flux density in the core is changed leading to an adaptation in core cross section. In order to find appropriate steel grade combinations and useful core cross sections, loss reduction caused by the mixed core design is approximated analytically with a MATLAB program. The results are the input to the FE simulation and the post-processing algorithm which is more realistic than the analytic approximation. If an excitation change between 1.35 T and 1.7 T is considered, a loss reduction of more than 10 % can be achieved by the mixed core design concept compared to the corresponding reference core setup. A further criterion is the total cost of ownership including purchase price and life cycle costs for the customer. Life cycle costs of a transformer are capitalized losses over its lifetime which is assumed to be 40 years in this work. It turned out, that the total cost of ownership is significantly lower for the mixed core design leading to cost savings of almost 10 % of the former purchase price during the time the transformer is in service.

Another important part of this thesis is dedicated to the measurement of magnetic properties orthogonal to the sheet plane. A new measurement device, the normal direction tester, to study electrical steel with flux applied in normal direction is developed. The homogeneity of the flux density in the steel sheet samples and a negligible leakage flux

are proved by an FE simulation of the NDT. Especially, the generation of eddy currents inside the steel sheet samples as part of the new measurement setup and the ability to gauge magnetic properties orthogonal to the sheet plane are analyzed in detail. It becomes apparent that specific losses in normal direction cannot be determined due to their dependence on the sample geometry. The BH-curve in normal direction shows an almost linear relationship of magnetic field versus flux density and a considerably small relative permeability value of approximately 30 for different steel qualities. Simulations of core losses in power transformers can be improved using measurement results of the NDT because up to now only characteristics of the trans-rolling direction are implemented to describe magnetic properties in normal direction [27].

Another topic of the thesis is a new hysteresis model for electrical steel. It relies on measured hysteresis curves from minor to major loops. The data analysis is implemented in a MATLAB program which creates a hysteresis model for a variety of different electrical steels. Although the model requires detailed measurements, the transfer from time to frequency domain delivers a significant data reduction. Finally, less than 15 % of the former measured data amount is needed for a good reproduction of the magnetic field as a function of arbitrary flux density amplitudes. In comparison to the linear interpolation of the magnetic field in time domain, the new model shows better results, especially for saturating fields. In this work this new hysteresis model is used to determine three different magnetization curves for the characterization of magnetic properties in FE software.

### **Outline of future work**

The normal direction tester as new measurement device delivers BH-curve characterizing magnetic properties of electrical steel orthogonal to the sheet plane which could be used to simulate flux density and magnetic field distribution in FE models of step-lap joints. The contribution of hysteresis and excess losses to the specific total losses can be investigated with a low excitation frequency decreasing the distortion of flux density by eddy currents to an acceptable minimum. Since the flux density can be assumed to be homogeneous, hysteresis and excess losses do not depend on the sample size and they can be calculated as stated in [43]. After adapting the frequency to values utilized in power systems, losses generated by the flux in normal direction can be determined in an FE model as the sum of eddy current losses computed with the eddy current distribution plus hysteresis and excess losses.

According to the mixed core design concept, a more overall steel grade database of possible steel qualities including more reliable price information can be implemented which may lead to better steel grade combinations. Assumptions for material costs and labor expenses should be replaced by approved price information of all transformer components to improve the total cost of ownership calculation as a criterion to select the best

transformer design option. Nonetheless, the method to determine specific prices and labor expenses in this work seems to be realistic. However, a transformer manufacturer has such data available and is, therefore, able to implement a mixed core design concept. The environmental cost of transformer losses as introduced in [28] could be carried out in the total cost of ownership calculation. Furthermore, transformers including three phase applications must be investigated leading to improvements in the core loss simulation approach by means of rotational power losses [25, 26] and magnetic anisotropy of electrical steel. In a future step, the mixed core design needs to be verified by measurements on real transformers and the impact of the new design method on noise emission of transformers must be considered [13].



# Appendix

## A Measurement setup

### A.1 Graphic user interface (GUI)

The software controlling the measurement procedure of electrical steel's properties runs on a usual PC and is based on MATLAB. There are three different interfaces which guide the user through the measurement preparation and provide feedback about the measurement progress. Fig. A-1 shows the first one termed "Measurement Device & Sample Specifications". The user can choose between different measurement devices and adapt its parameters. Furthermore, the settings of steel sheet sample, the gain for the four quadrant chopper and variables for signal processing can be defined.

**Measurement Device & Sample Specifications**

Select measurement device

Epstein frame     Single Sheet Tester     Normal Direction Tester

**Parameters**

Magnetic path length [m]    0.2

N1 turns    150

N2 turns    150

R<sub>primary</sub> [Ohm]    1

**Steel sheet sample**

Sample mass [kg]    0.160

Density [kg/m<sup>3</sup>]    7650

Sample length [m]    0.25

Active sample mass [kg]    0.128

Calculate cross section

Cross section [m<sup>2</sup>]    8.366e-05

**Four quadrant chopper**

Gain    5.3

**Signal processing**

Shunt resistor [Ohm]    0.5

**Current gain**

Gain:    1

**Voltage gain**

Gain:    0.798

Stop    Calculate    Save and Continue

**Fig. A-1:** Measurement device and sample specifications

In the next step of the procedure, the steel sheet sample is demagnetized to avoid an erroneous measurement due to remanence. Fig. A-2 illustrates the “Demagnetization” GUI with its adjustable parameters in the upper half and a preview window for the generated voltage signal plus a figure for the measured voltage slope in the lower half.

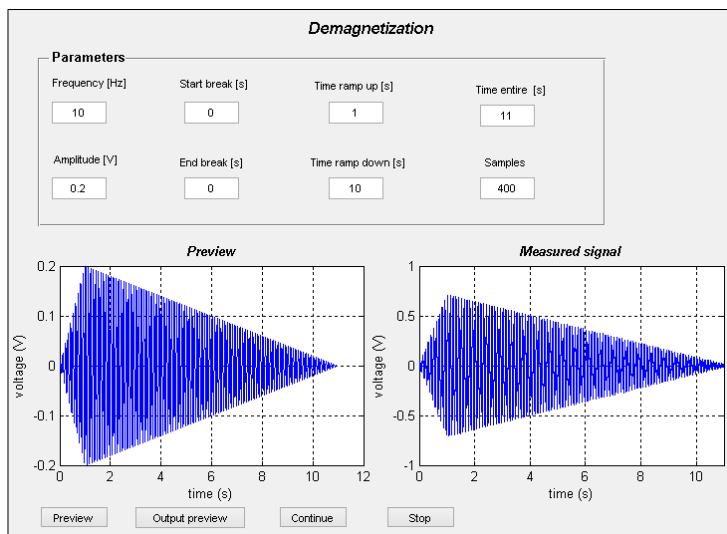


**Fig. A-2:** Parameters for demagnetization

The main tasks to measure magnetic properties of electrical steel are implemented in the GUI shown in Fig. A-3. Red rectangles indicate different working areas of the interface. The user can select measurement parameters like frequency and polarization ranges in section I. Part II contains the settings of the controller for a sinusoidal secondary voltage and section III delivers calculated values of the latest measurement. Additionally, there are five graphs which display the demagnetization voltage slope (1), the measured primary current and secondary voltage (2) as well as the already gauged hysteresis curves in the applied polarization range. The graphs 5 and 6 express the controller progress by the relative error of the required polarization amplitude and the *THD* of the secondary voltage. The magnetic measurement software offers the possibility to gauge magnetic characteristics of electrical steel with three different measurement devices in an arbitrary frequency and polarization range automatically. After each polarization and frequency step all measured and calculated results plus the entire settings are stored in a separate file on the hard drive of the PC and can be used for further analysis.

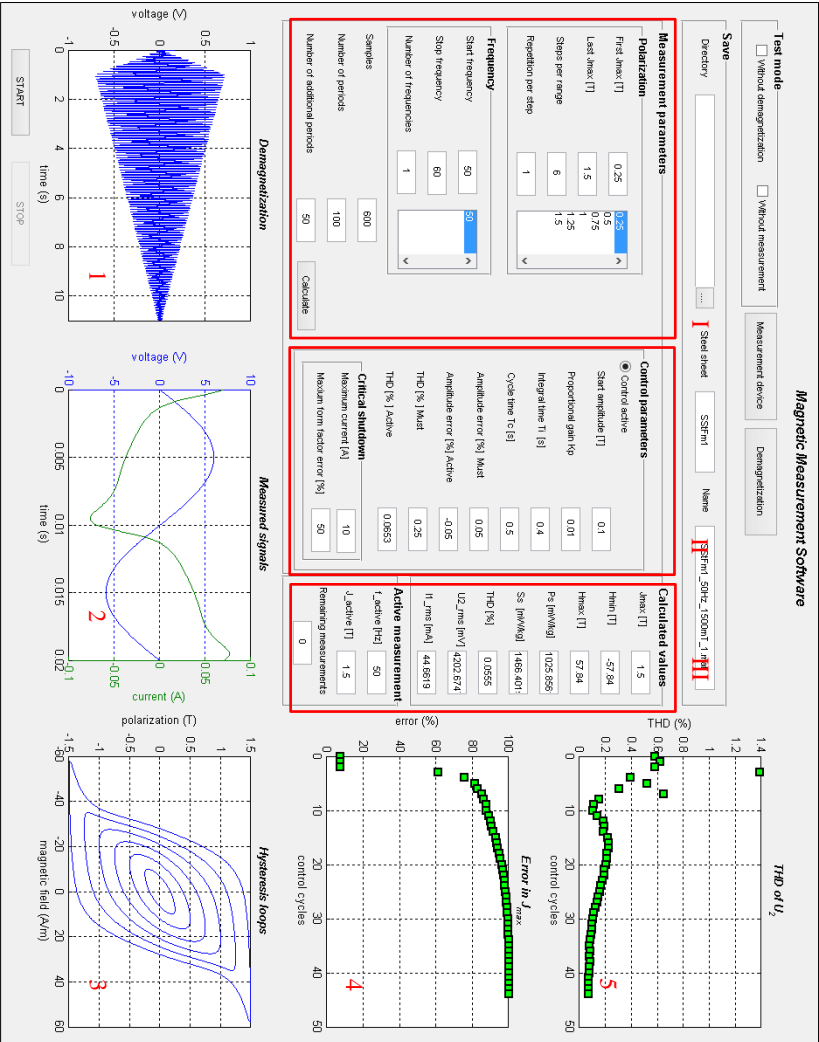


Fig. A-3: Magnetic measurement software

## A.2 Datasheets

### A.2.1 Data acquisition and signal generation unit

## DT9847 Series

### Dynamic Signal Analyzer for USB With Low THD and Wide Dynamic Range

The DT9847 Series are high-accuracy, dynamic signal acquisition modules designed for sound and vibration applications. These modules are ideal for precision measurements with microphones, accelerometers, and other transducers that have a large dynamic range. Common applications include audio, acoustic, and vibration testing.

Combine the DT9847 with the ready-to-measure QuickDAQ application to create a powerful FFT Analyzer instrument. Additionally, all Data Translation devices include comprehensive driver and software support, and interface tools for LabVIEW™ and MATLAB® programmers.

#### Key Features:

- Simultaneous analog input and waveform analog output operations
- Analog input subsystem:
  - Up to three, simultaneous 24-bit A/D converters
  - Throughput rate from 1 kSamples/s to 216 kSamples/s
  - Input range of  $\pm 10V$  with software-selectable gains of 1 and 10 for an effective input range of  $\pm 10V$  and  $\pm 1V$
  - Support for IEPE (Integrated Electronic Piezoelectric) inputs, including use of a 4mA current source with 18V compliance voltage for AC or DC coupling
  - Supports a start trigger for acquiring pre-trigger samples and a reference trigger for acquiring post-trigger samples. Specify the number of post-trigger samples to acquire before stopping the operation.
  - For the start trigger, supports a software-programmable trigger source (software, external digital trigger, or a positive- or negative-going analog threshold trigger on any of the analog input channels). The threshold trigger can be programmed for a value from  $\pm 10V$ .
  - For the reference trigger, supports a positive- or negative-going analog threshold trigger on any of the analog input channels. The threshold trigger can be programmed for a value from  $\pm 10V$ .

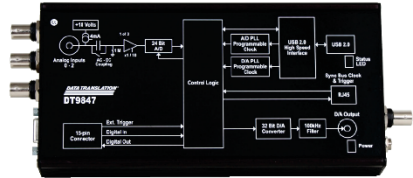


Figure 1: The DT9847 Series features ultra-low total harmonic distortion (THD) of 102 dB and wide dynamic range up to 123 dB for precision measurements in sound and vibration applications.

- Analog output subsystem:
  - Up to two 32-bit D/A converters
  - Single value, waveform, and continuous streaming output
  - Programmable output rate from 30 kSamples/s to 216 kSamples/s
  - Output range of  $\pm 10V$  and  $\pm 3V$
  - Software-programmable trigger source (software trigger or external digital trigger) to start the analog output operation
- Internal clock source (shared between the analog input and analog output subsystems)
- Sync Bus (RJ45) connector for synchronizing acquisition on up to four DT9847 Series modules

#### Analog Input Channels

The DT9847-2-2 module provides two analog input channels and the DT9847-3-1 module provides three analog input channels. These are single-ended channels; IEPE sensors can be connected to these inputs. Software-selectable gains of 1 and 10 provide effective input ranges of  $\pm 10V$  and  $\pm 1V$ . The DT9847 Series modules use 24-bit Delta-Sigma analog-to-digital converters (ADCs) that provide anti-aliasing filters based on the clock rate. These filters remove aliasing, which is a condition where high frequency input components erroneously appear as lower frequencies after sampling.

DT9847 Series modules can acquire a single value from a single analog input channel, a single value from all the analog input channels simultaneously, or multiple values from a group of analog input channels.

Fig. A-4: Data acquisition and signal generation unit, Data Translation DT9847

## A.2.2 Power supply

## Übersicht DCP520-Reihe

servowatt

## Lineare Präzisions Leistungs-Operations-Verstärker. Standardversionen mit 500 Watt Ausgangsleistung

Die Leistungs-Operations-Verstärker der DCP 520-Reihe beinhalten auf einer Chassisgrundfläche von 430 mm x 250 mm zwei Endstufen mit je einem Lüfter zur Kühlung und das dazugehörige Hauptnetzteil mit einem Einphasen-Netztransformator für 230 Volt.

## Ausgangsdaten (\* bevorzugte Standardversionen)

| Typ          | Ausgangsspannung im Leerlauf | Ausgangsspannung bei Nennstrom | Ausgangsennstrom | **Spitzenstromeinstellungen       |                                   |
|--------------|------------------------------|--------------------------------|------------------|-----------------------------------|-----------------------------------|
|              |                              |                                |                  | C 2-fach<br>$\tau = 500\text{ms}$ | B 3-fach<br>$\tau = 200\text{ms}$ |
| DCP 520/30 * | + 30 V                       | + - 25 V                       | + - 20,0 A       | 40,0 A                            | 60,0 A                            |
| DCP 520/42   | + - 42 V                     | + - 35 V                       | + - 14,4 A       | 28,8 A                            | 43,2 A                            |
| DCP 520/60 * | + 60 V                       | + 50 V                         | + 10,0 A         | 20,0 A                            | 30,0 A                            |
| DCP 520/84   | + - 84 V                     | + - 71 V                       | + - 7,2 A        | 14,4 A                            | 21,6 A                            |

\*\* Der Dauernennstrom und der Spitzenstrom werden mit den Trimmern P1, P2, P3 und P4 werkseitig eingestellt. Die Spitzenstromdauer wird durch Auswahl der Kondensatoren C5 und C6 werkseitig eingestellt. Abweichende Einstellungen sind je nach Applikation nach Absprache möglich, siehe auch Leistungsdiagramme.

## Eingangsdaten - Differenzverstärker E+ / E-

| Eingangsstufe von OpAmp                             | Standard            | FET                       |
|---|---------------------|---------------------------|
| Differenz-Eingangswiderstand                        | 100 M $\Omega$      | 10 <sup>12</sup> $\Omega$ |
| Eingangsruhestrom (input bias current)              | <2 nA               | 5 pA                      |
| Eingangsruhestrom-Differenz                         | <1 nA               | 1 pA                      |
| Offsetspannungs-Temperaturdrift                     | 0,3 $\mu\text{V/K}$ | 5 $\mu\text{V/K}$         |
| Gleichtakteingangsspannungs-Unterdrückung / 10 Hz   | 135 dB              | 95 dB                     |
| Eingangsoffsetstellbereich                          | + - 1 mV            | + - 10 mV                 |
| Eingangsrauschen Breitband, V <sub>r</sub> = - 1000 | 7 $\mu\text{Veff}$  | 15 $\mu\text{Veff}$       |
| Maximale zulässige Eingangsspannung (E+ & E-)       | + - 11 V            | + - 11 V                  |
| Versorgungsspannungs-Durchgriff                     | -170 dB             | -150 dB                   |

Die Eingangsoffsetspannung von ca. 1 mV ist durch 25k $\Omega$ -Trimmer auf Null abgleichbar.

## Transferdaten

|   |                      |                      |
|---|----------------------|----------------------|
| Offene Verstärkung im Leerlauf (10 Hz)                  | 50.000.000 V/V       | 10.000.000 V/V       |
| Offene Verstärkung bei Last (80% Last, 10 Hz)           | 30.000.000 V/V       | 5.000.000 V/V        |
| Regelgüte bei V <sub>r</sub> = -10 ist somit besser als | 3.000.000 : 1        | 500.000 : 1          |
| Ausgangsspannung Slew-Rate (dU <sub>a</sub> /dt)        | 7,5 V/ $\mu\text{s}$ | 7,5 V/ $\mu\text{s}$ |

Die 500 W Standardendstufe enthält Hochleistungstransistoren im Verlustleistungsgesamtwert von 3440 W.

Die 500 W Endstufe mit hermetischen Transistoren (TO3-Metall) hat einen Verlustleistungsgesamtwert von 3000 W.

Arbeitstemperaturbereich bei Nennlast

-30 °C bis +45 °C

Maximale Kühlkörpertemperatur bei Nennlast

+90 °C

Gewicht netto 18 kg, verpackt 20 kg

Obige Daten gelten, wenn nicht anders angegeben, bei 25 Grad C und Nennanschlussspannungen. Änderungen vorbehalten.

Fig. A-5: Power supply, Servowatt DCP 520/30

## A.2.3 Galvanic separation

### VariTrans A 26000

#### Product Line

| Device  | Input  | Output   | Order No.                     | Order No.                 |
|---|--|--|-------------------------------|---------------------------|
|   |  |  | with pluggable screw terminal | with fixed screw terminal |
| VariTrans A 26000<br>with calibrated switching<br>of input and output | 0 ... ±20 mA<br>0 ... ±10 V                                | 0 ... ±20 mA<br>0 ... ±10 V                                | A 26000 H1                    | A 26000 F1                |
| VariTrans A 26000<br>with fixed settings                              | 0 ... ±20 mA<br>0 ... ±20 mA<br>0 ... ±10 V<br>0 ... ±10 V | 0 ... ±20 mA<br>0 ... ±10 V<br>0 ... ±20 mA<br>0 ... ±10 V | A 26016 H1                    | A 26016 F1                |
|   |  |  | A 26018 H1                    | A 26018 F1                |
|   |  |  | A 26036 H1                    | A 26036 F1                |
|   |  |  | A 26038 H1                    | A 26038 F1                |

#### Power supply

20 ... 253 V AC/DC

#### Specifications

##### Input data

|                   |                                |   |
|-------------------|--------------------------------|---|
| Inputs            | 0 ... ±20 mA<br>0 ... ±10 V    | terminal selectable / switchable (default setting ±10 V)<br>or fixed setting (see product line)       |
| Input resistance  | Current input<br>Voltage input | voltage drop approx. 250 mV at 20 mA<br>approx. 1 Mohm  |
| Overload capacity | Current input<br>Voltage input | ≤ 300 mA<br>Voltage limiting to 30 V by suppressor diode,<br>max. allowable continuous current: 30 mA |

##### Output data

|                 |  |   |
|-----------------|--|---|
| Outputs         | 0 ... ±20 mA<br>0 ... ±10 V                | terminal selectable / switchable (default setting ±10 V)<br>or fixed setting (see product line) |
| Load            | with output current<br>with output voltage | ≤ 10 V (500 ohms at 20 mA)<br>≤ 10 mA (1 kohm at 10 V) <sup>1)</sup>                            |
| Offset          | 20 µA or 10 mV                             |   |
| Residual ripple | < 10 mV <sub>rms</sub>                     |   |

##### Transmission behavior

|                                       |   |
|---------------------------------------|---|
| Gain error                            | < 0.1 % meas.val. (DC)                        |
| Cutoff frequency                      | > 5 kHz, -3 dB                                |
| Temperature coefficient <sup>2)</sup> | 0.0075 %/K full scale (reference temp. 23 °C) |

Fig. A-6: Galvanic separation, Knick VariTrans A 26000

### A.3 Transfer ratios and calibration

The measurement system introduced in chapter 3.1 includes two analog input channels for a current and a voltage signal. The transfer ratios of both inputs must be determined reliably. Fig. A-7 illustrates the test setup for the transfer ratio determination. The measurement device is a SST equipped with an arbitrary steel sheet sample. A power meter LMG 500 [10] works as reference. All other components of the setup are the same as explained in chapter 3.1. The transfer ratio describes the entire signal path, beginning at the analog source including voltage divider or shunt resistor, passing the A/D converters and finally reaching software calculations. Each path is influenced differently by the chain of signal processing. The voltage divider mainly affects the ratio of the voltage path and the shunt resistor plays the same role for the current path. Nonetheless, all steps in each signal chain must be considered.

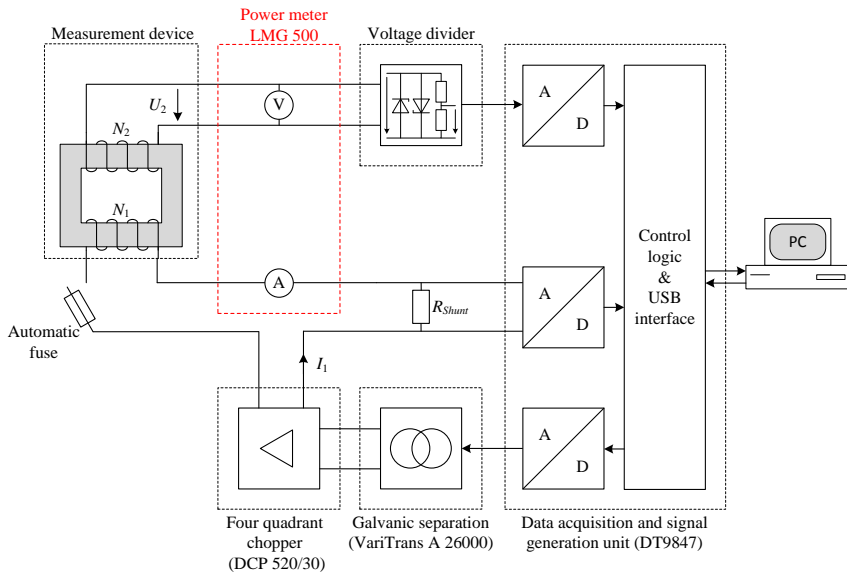


**Fig. A-7:** Test setup for transfer ratio determination and calibration

A comparison of measurements obtained by software and power meter define each transfer ratio. Table A-1 gives the voltage ratio determination based on five measurements while a ratio of 0.8:1 is assumed in the MATLAB GUI. The current transfer ratio is concluded in Table A-2 whereas again five repetitions are performed and the ratio in the GUI is supposed to be of 1:1.

**Table A-1:** Determination of the transfer ratio for the voltage signal path

| Number   | LMG 500<br>$U_2$ in V | MATLAB GUI<br>$U_2$ in V | Transfer ratio |
|----------|-----------------------|--------------------------|----------------|
| 1        | 3.027                 | 3.021                    | 0.798          |
| 2        | 3.029                 | 3.023                    | 0.798          |
| 3        | 3.027                 | 3.021                    | 0.798          |
| 4        | 3.025                 | 3.019                    | 0.798          |
| 5        | 3.028                 | 3.022                    | 0.798          |
| Average: |                       |                          | 0.798 : 1      |

**Table A-2:** Determination of the transfer ratio for the current signal path

| Number   | LMG 500<br>$I_1$ in mA | MATLAB GUI<br>$I_1$ in mA | Transfer ratio |
|----------|------------------------|---------------------------|----------------|
| 1        | 25.78                  | 25.75                     | 1.00           |
| 2        | 26.09                  | 25.96                     | 1.00           |
| 3        | 26.00                  | 25.90                     | 1.00           |
| 4        | 26.08                  | 25.98                     | 1.00           |
| 5        | 25.98                  | 25.93                     | 1.00           |
| Average: |                        |                           | 1 : 1          |

The average calculation of the two transfer ratios shows a negligible deviation and both average values are used to characterize the signal path of the voltage and the current signal respectively.

According to [70] the calibration of the active power requires a measurement uncertainty 0.5 %. In this work, the deviation of active power gauged by the measurement setup and recorded by the power meter as reference approximates the uncertainty of the setup (compare Fig. A-7). Table A-3 demonstrates the relative deviation in active power measurements from small to high polarization values.

**Table A-3:** Approximation of measurement uncertainty in gauged active power

| Polarization<br>$\hat{J}$ in T | LMG 500<br>$P$ in mW | MATLAB GUI<br>$P$ in mW | Deviation<br>in % |
|--------------------------------|----------------------|-------------------------|-------------------|
| 0.10                           | 0.775                | 0.775                   | 0.00              |
| 0.25                           | 4.310                | 4.306                   | -0.09             |
| 0.50                           | 15.705               | 15.699                  | -0.04             |
| 0.75                           | 34.146               | 34.091                  | -0.16             |
| 1.00                           | 57.550               | 57.569                  | 0.03              |
| 1.25                           | 89.002               | 89.007                  | 0.01              |
| 1.50                           | 130.962              | 130.876                 | -0.07             |
| 1.68                           | 182.910              | 182.841                 | -0.04             |
| 1.73                           | 204.570              | 204.659                 | 0.04              |
| 1.84                           | 266.200              | 266.133                 | -0.03             |

The approximation delivers a highest deviation of -0.16 %. Hence, it is assumed that the measurement setup fullfills the requirements stated in the standard IEC 60404-3 [70].



## B.2 Measured steel sheet data

In this work, several electrical steel grades are investigated; *maximum*, *inductive* and *resistive* BH-curves plus a  $P_S$ -curve (compare chapter 4) characterize their magnetic properties. Table B-1 explains which steel grade is used in which application and Fig. 2 to Fig. 5 illustrate the BH- and  $P_S$ -curves.

**Table B-1:** Relationship of steel grade and application

| Steel grade | Application                  | Chapter   |
|-------------|------------------------------|-----------|
| 23ZH85      | SST                          | 3,4 and 6 |
| C165-35     | SST, $T_1$ , $T_2$ and $T_3$ | 3,4 and 6 |
| H103-27     | NDT                          | 5         |
| M140-27     | $T_4$                        | 6         |

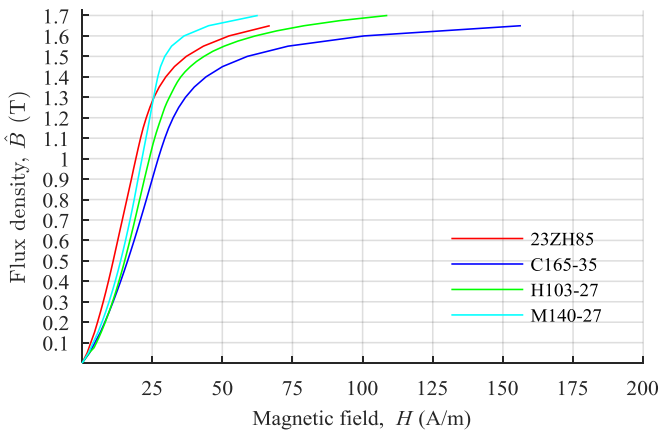


**Fig. B-2:** *maximum* BH-curves of applied electrical steel grades

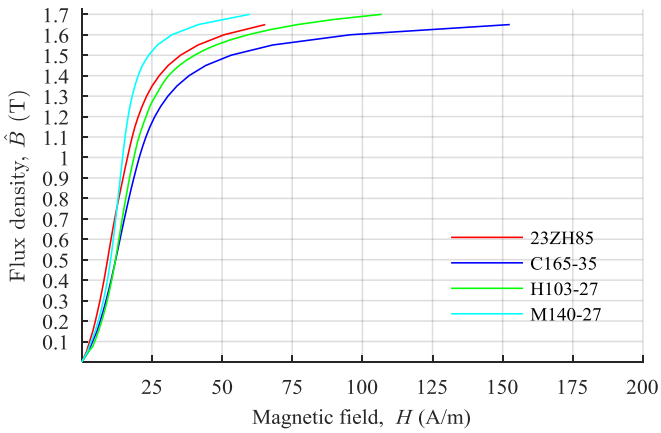


**Fig. B-3:** inductive BH-curves of applied electrical steel grades

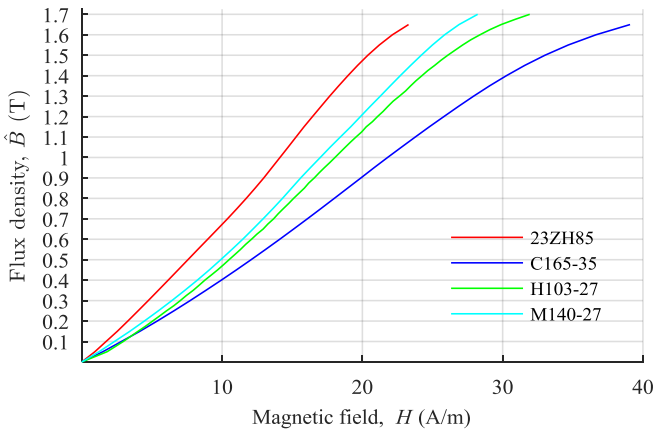


**Fig. B-4:** resistive BH-curves of applied electrical steel grades

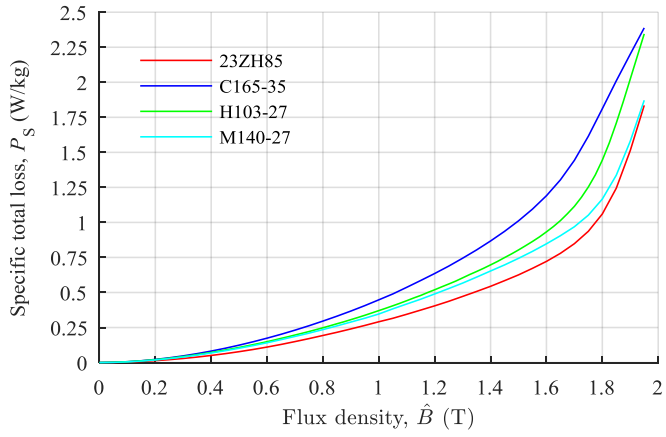


**Fig. B-5:** Specific total loss curves of applied electrical steel grades

## C Bibliography

### C.1 References

- [1] Coey, J. M. D., *Magnetism and magnetic materials*, Cambridge Univ. Press, Cambridge 2010. ISBN: 9780521816144.
- [2] Song, M., Yoon, H., Yang, H., Koh, C. S., "A generalized Chua-type vector hysteresis model for both the non-oriented and grain-oriented electrical steel sheets". *IEEE Transactions on Magnetics*. 2011, 47, 1146–1149, DOI: 10.1109/TMAG.2010.2073686.
- [3] Saito, Y., Hayano, S., Nakamura, H., Kishino, Y., Tsuya, N., "A representation of magnetic hysteresis by fourier series". *Journal of Magnetism and Magnetic Materials*. 1986, 54-57 (1986), 1613–1614.
- [4] Stalprodukt S.A., "Laser treated electrical steel", [Internet], Stalprodukt S.A., 2011 [modified 2011; cited 2015 Apr 2]. Available from: [http://www.stalprodukt.com.pl/pub/File/PDF/new\\_3/blachy\\_laserowane.html](http://www.stalprodukt.com.pl/pub/File/PDF/new_3/blachy_laserowane.html).
- [5] Sievert, J., Ahlers, H., "Epstein to SST relationship - statistical rather than deterministic". *Przegląd Elektrotechniczny*. 2011, 87, 17–19.
- [6] Shirkoohi, G. H., Arikat, M.A.M., "Anisotropic properties of high permeability grain-oriented 3.25% Si-Fe electrical steel". *IEEE Transactions on Magnetics*. 1994, 30, 928,930.
- [7] Tumański, S., "A method of testing of the plane distribution of anisotropy". *IEEE Transactions on Magnetics*. 2002, 38, 2808–2810, DOI: 10.1109/TMAG.2002.803565.
- [8] Yoon, H., Kim, I., Shin, P. S., Koh, C. S., "Finite element implementation of a generalized chua-type vector hysteresis model and application to iron loss analysis of three-phase transformer". *IEEE Transactions on Magnetics*. 2011, 47, 1122–1125, DOI: 10.1109/TMAG.2010.2073684.
- [9] Shirkoohi, G. H., Arikat, M. A. M., "Anisotropic properties of high permeability grain-oriented 3.25% Si-Fe electrical steel". *IEEE Transactions on Magnetics*. 1994, 30, 928–930, DOI: 10.1109/20.312448.
- [10] ZES Zimmer, "LMG 500 Präzisions-Leistungsmessgerät", [Internet], 2011 [cited 2016 Aug 23]. Available from: <http://www.zes.com/de/Produkte/Praezisions-Leistungsmessgeraete/LMG500>.
- [11] Sievert, J., "The measurement of magnetic properties of electrical sheet steel – survey on methods and situation of standards". *Journal of Magnetism and Magnetic Materials*. 2000, 647–651, DOI: 10.1016/S0304-8853(00)00251-1.
- [12] Lutz, H., Wendt, W., *Taschenbuch der Regelungstechnik: Mit MATLAB und Simulink*, 10th Ed., Verl. Europa-Lehrmittel Nourney Vollmer, Haan-Gruiten 2014. ISBN: 9783808556795.

- 
- [13] Smith, S. W., *The scientist and engineer's guide to digital signal processing*, 1st Ed., California Technical Publ, San Diego, Calif. 1997. ISBN: 9780966017632.
- [14] Sievert, J., *Comparison of different measuring procedures for the determination of the magnetic characteristics of electrical steel sheets using single sheet testers* EUR BCR information - applied metrology, Vol. 12265, Commission of the European Communities, Luxembourg 1989.
- [15] Nakata, T., Takahashi, N., Kawase, Y., Nakano, M., Miura, M., Sievert, J. D., "Numerical analysis and experimental study of the error of magnetic field strength measurements with single sheet testers". *IEEE Transactions on Magnetics*. 1986, MAG-22.
- [16] Godec, Z., "Influence of Slitting on Core Losses and Magnetization Curve of Grain-Oriented Electrical Steels". *IEEE Transactions on Magnetics*. 1977, MAG-13, 1053–1057, DOI: 10.1109/TMAG.1977.1059514.
- [17] Nakata, T., Fujiwara, K., Nakano, M., Kayada, T., "Influence of Yoke Construction on Magnetic Characteristics of Single Sheet Testers". *IEEE Translation Journal on Magnetics in Japan*. 1990, 5, 618–624, DOI: 10.1109/TJMJ.1990.4564151.
- [18] Sievert, J., Son, D., "On the effective magnetic path length used for field strength and loss determination". *Journal of Magnetism and Magnetic Materials*. 1984, 41, 235–237.
- [19] Nakata, T., Takahashi, N., Fujiwara, K., Nakano, M., "Measurement of magnetic characteristics along arbitrary directions of grain-oriented silicon steel up to high flux densities". *IEEE Transactions on Magnetics*. 1993, 29, 3544–3546, DOI: 10.1109/20.281224.
- [20] Tang, Q., Wang, Z., et al., "Measurement of magnetic properties of electrical steel at high flux densities using an improved single sheet tester". *18th International Symposium on High Voltage Engineering (ISH)*. Hanyang University Seoul Korea, Aug. 25, 2013. ISBN: 978-89-86510-18-8.
- [21] Biela, J., *Skriptum Professur für Hochleistungselektronik: Wirbelstromverluste in Wicklungen induktiver Bauelemente*, ETH Zürich 2012.
- [22] Leibfried, T., *Manuskript zur Vorlesung Energieübertragung und Netzregelung (EÜN)*, Karlsruhe Institute for Technology, Sommersemester 2016.
- [23] Fitzgerald, A. E., Kingsley, C., Umans, S. D., *Electric machinery* McGraw-Hill series in electrical engineering Power and energy, 6th Ed., McGraw-Hill, Boston, Mass. 2003. ISBN: 0071121935.
- [24] ABB Transformers, "Total Cost of Ownership method basics of transformer TCO calculation", [Internet], ABB Transformers, 2015 [cited 2016 Aug 8]. Available from: <http://new.abb.com/docs/librariesprovider95/energy-efficiency-library/tco-method-basics.pdf?sfvrsn=2>.
- [25] Moses, A. J., "Importance of rotational losses in rotating machines and transformers". *Journal of Materials Engineering and Performance*. 1992, 1, 235–244, DOI: 10.1007/BF02648622.

- [26] Enokizono, M., Suzuki, T., Sievert, J., Xu, J., "Rotational power loss of silicon steel sheet". *IEEE Transactions on Magnetics*. 1990, 26, 2562–2564.
- [27] Mechler, G. F., Girgis, R. S., "Calculation of spatial loss distribution in stacked power and distribution transformer cores". *IEEE Transactions on Power Delivery*. 1998, 13, 532–537, DOI: 10.1109/61.660925.
- [28] Georgilakis, P. S., Fofana, I., Olivares-Galvan, J. C., Escarela-Perez, R., Stefanopoulos, G. K., "Environmental cost of transformer losses for industrial and commercial users of transformers" *43rd North American Power Symposium (NAPS)*. Boston USA, 2011. ISBN: 9781457704192, DOI: 10.1109/NAPS.2011.6024860.
- [29] Yagisawa, T., Takekoshi, Y., Wada, S., "Magnetic properties of laminated steel sheets for normal fluxes". *Journal of Magnetism and Magnetic Materials*. 1982, 26, 340–342.
- [30] Mechler, G. F., Girgis, R. S., "Magnetic flux distributions in transformer core joints". *IEEE Transactions on Power Delivery*. 2000, 15, 198–203, DOI: 10.1109/61.847251.
- [31] Hihat, N., Lecoite, J. P., Duchesne, S., Napieralska, E., Belgrand, T., "Experimental method for characterizing electrical steel sheets in the normal direction". *Sensors (Switzerland)*. 2010, 10, 9053–9064, DOI: 10.3390/s101009053.
- [32] Booth, T., Pftzner, H., "Characteristics of transformer core materials for flux normal to the sheet plane". *Journal of Magnetism and Magnetic Materials*. 1994, 133, 183–186.
- [33] Burkard, H., *Tabellenbuch Elektrotechnik: Tab., Formeln, DIN-Normen, VDE-Bestimmungen für Rechnen, Fachkunde, Zeichnen, Werkstoffkunde Europa-Fachbuchreihe : Elektrotechnik*, 9th Ed., Verlag Europa-Lehrmittel, Wuppertal 1978. ISBN: 9783808531099.
- [34] Theocharis, A. D., Tzinevrakis, A., Charalampakos, V., Miliadis-Argitis, J., Zacharias, T., "Transformer modeling based on incremental reluctances *Power System Technology: Technological Innovations Making Power Grid Smarter (POWERCON 2010)*, International Conference on. Hangzhou China, DOI: 10.1109/POWERCON.
- [35] Theocharis, A. D., Miliadis-Argitis, J., Zacharias, T., "Single-phase transformer model including magnetic hysteresis and eddy currents". *Electrical Engineering*. 2008, 90, 229–241, DOI: 10.1007/s00202-007-0071-5.
- [36] Debye, P., "Wirbelströme in Stäben von rechteckigem Querschnitt". *Zeitschrift für Mathematik und Physik*. 1906, 54, 418–437.
- [37] Nippon Steel & Sumitomo Metal Corporation Group, "ELECTRICAL STEEL SHEETS", [Internet], Nippon Steel & Sumitomo Metal Corporation Group, 2015 [modified 09.2015; cited 2016 Aug 24]. Available from: [http://www.nssmc.com/product/catalog\\_download/pdf/D003jec.pdf](http://www.nssmc.com/product/catalog_download/pdf/D003jec.pdf).
- [38] Hoffman, P., Bryan, W., "Large Power Transformers and the U.S. Electric Grid", [Internet], Infrastructure Security and Energy Restoration Office of Electricity Delivery and Energy Reliability U.S. Department of Energy, 2014 [modified April 2014; cited 2016 Sep 21]. Available from: <http://www.energy.gov/sites/prod/files/2014/04/f15/LPTStudyUpdate-040914.pdf>.

- [39] Bertotti, G., *Hysteresis in Magnetism: For physicists, materials scientists, and engineers* *Electromagnetism*, Academic Press, San Diego 1998. ISBN: 9780120932702, DOI: 10.1016/b978-0-12-093270-2.x5048-x.
- [40] Loffler ,F., Booth, T., Pfutzner ,H., Bengtsson, C., Gramm, K., "Influence of air gaps in stacked transformer cores consisting of several packages". *IEEE Transactions on Magnetics*. 1994, 30, 913–915, DOI: 10.1109/20.312443.
- [41] R., S. Girgis, E., G. te Nijenhuis, K., Gramm, J., E. Wrethag, "Experimental investigations on effect of core production attributes on transformer core loss performance". *IEEE Transactions on Power Delivery*. 1998, 13, 526–531, DOI: 10.1109/61.660924.
- [42] Brailsford, F., Oliver, D. A., Hadfield, D., Polgreen, G. R., "Magnetic materials. A review of progress". *Electrical Engineers - Part I: General, Journal of the Institution of*. 1948, 1948, 522–543, DOI: 10.1049/ji-1.1948.0195.
- [43] Bertotti, G., "General properties of power losses in soft magnetic materials". *IEEE Transactions on Magnetics*. 1987, 24, 621–630, DOI: 10.1109/20.43994.
- [44] Tumański, S., *Handbook of magnetic measurements* *Series in sensors*, CRC Press, Boca Raton, FL 2011. ISBN: 1439829527, DOI: 10.1201/b10979.
- [45] Goss, N. P., *Electrical sheet and method and apparatus for its manufacture and test*. US1965559 A, 1933.
- [46] R. Minhaz, "Transformer Manufacturing Processes", *IEEE Hamilton Section*, Hamilton, Ontario, Canada 2015 Oct 15.
- [47] Del Vecchio, R. M., Poulin, B., Feghali, P. T., Shah, D. M., Ahuja, R., *Transformer design principles: With applications to core-form power transformers*, 2nd Ed., CRC Press, Boca Raton, Fla. 2010. ISBN: 9781439805824.
- [48] Harlow, J. H., *Electric Power Transformer Engineering* *The Electric Power Engineering Hbk, Second Edition*, CRC Press, Boca Raton 2004. ISBN: 0-8493-1704-5, DOI: 10.1201/9781420008715.
- [49] Heathcote, M. J., *J&P Transformer Book*, Elsevier, Oxford 2007. ISBN: 978-0-7506-8164-3, DOI: 10.1016/b978-075068164-3/50001-6.
- [50] EUROPEAN COMMISSION, *COMMISSION REGULATION (EU) No 548/2014 on implementing Directive 2009/125/EC of the European Parliament and of the Council with regard to small, medium and large power transformers*, 2014.
- [51] Dornbusch, H. W., *Method of making wound transformer cores*. US 2489625 A, 1949.
- [52] Loffler ,F., Booth, T., Pfutzner ,H., Bengtsson, C., Gramm, K., "Relevance of step-lap joints for magnetic characteristics of transformer cores". *IEE Proceedings Electric Power Applications*. 1995, 142, 371–378, DOI: 10.1049/ip-epa:19952228.
- [53] Kulkarni, S. V., Khaparde, S. A., *Transformer engineering: Design, technology, and diagnostics*, 2nd Ed., CRC Press, Boca Raton, Fla. 2012. ISBN: 978-1-4398-5377-1, DOI: 10.1201/b13011.
- [54] Feinberg, R., *Modern power transformer practice*, Macmillan, London 1979. ISBN: 0333245377, DOI: 10.1007/978-1-349-04087-2.

- [55] Zhou, P., *Numerical Analysis of Electromagnetic Fields Electric Energy Systems and Engineering Series*, Springer, Berlin, Heidelberg 1993. ISBN: 9783642503214, DOI: 10.1007/978-3-642-50319-1.
- [56] Kahveci, A., Tietz, M., "Herstellung, Charakterisierung und Normung von anwendungsoptimierten Elektrolechen höchster Effizienz", thyssenkrupp Steel *Instituts-kolloquium am Elektrotechnischen Institut, Karlsruher Institut für Technologie*, Elektrotechnisches Institut 2016 Jun 13.
- [57] *Introduction to ANSYS Maxwell: Module 03: Transient solvers*, ANSYS, Inc, 2016.
- [58] *Introduction to ANSYS Maxwell: Module 07: Transformers/Inductors*, ANSYS, Inc, 2016.
- [59] Schwab, A. J., *Field Theory Concepts: Electromagnetic Fields Maxwell's Equations grad, curl, div. etc. Finite-Element Method Finite-Difference Method Charge Simulation Method Monte Carlo Method*, Springer Berlin Heidelberg, Berlin, Heidelberg 1988. ISBN: 9783642489433, DOI: 10.1007/978-3-642-48941-9.
- [60] Drake, A. E., "Precise total power loss measurements on electrical sheet steels". *Journal of Magnetism and Magnetic Materials*. 1982, 26, 181–184.
- [61] Ivers-Tiffée, E., Münch, W., *Werkstoffe der Elektrotechnik*, 10th Ed., B.G. Teubner Verlag / GWV Fachverlage GmbH Wiesbaden, Wiesbaden 2007. ISBN: 9783835100527, DOI: 10.1007/978-3-8351-9088-7.
- [62] Barranger, J., *Hysteresis and eddy-current losses of a transformer lamination viewed as an application of the Poynting theorem* NASA technical note D, Vol. 3114, National Aeronautics and Space Administration, Washington, DC 1965.
- [63] Sievert, J., "Recent Advances in the One- and Two-Dimensional Magnetic Measurement Technique for Electrical Sheet Steel". *IEEE Transactions on Magnetics*. 1990, 26, 2553–2558, DOI: 10.1109/20.104796.
- [64] thyssenkrupp Steel Europe AG, "Grain oriented electrical steel PowerCore", [Internet], 2016 [cited 2016 Sep 23]. Available from: [https://www.thyssenkrupp-steel.com/media/content\\_1/produkte/elektroband/electrical\\_steel\\_integration/thyssenkrupp\\_electrical\\_steel\\_product\\_range\\_2016.pdf](https://www.thyssenkrupp-steel.com/media/content_1/produkte/elektroband/electrical_steel_integration/thyssenkrupp_electrical_steel_product_range_2016.pdf).

## C.2 Standards

- [65] IEC 61000-4-7:2002 + A1:2008, *Electromagnetic compatibility (EMC) - Part 4-7: Testing and measurement techniques - General guide on harmonics and interharmonics measurements and instrumentation, for power supply systems and equipment connected thereto*, 2008.
- [66] IEEE C57.12.91-2011, *IEEE Standard Test Code for Dry-Type Distribution and Power Transformers*, 2012, DOI: 10.1109/IEEESTD.2012.6152116.
- [67] EN 10341:2006, *Cold rolled electrical non-alloy and alloy steel sheet and strip delivered in the semi-processed state*, 2006.

- [68] EN 10342:2005, *Magnetic materials - Classification of surface insulations of electrical steel sheet, strip and laminations; German version*, 2005.
- [69] EN 10107:2014, *Grain-oriented electrical steel strip and sheet delivered in the fully processed state; German version*, 2014.
- [70] IEC 60404-3:1992 + A1:2002 + A2:2009, *Magnetic materials - Part 3: Methods of measurement of the magnetic properties of electrical steel strip and sheet by means of a single sheet tester*, 2010.
- [71] EN 60404-13:2007, *Magnetic materials - Part 13: Methods of measurement of density, resistivity and stacking factor of electrical steel sheet and strip (German version)*, 2008.
- [72] IEC 60404-2:1996 + A1:2008, *Magnetic materials - Part 2: Methods of measurement of the magnetic properties of electrical steel strip and sheet by means of an Epstein frame*, 2008.

### C.3 Author's publications

- [73] Freitag, C., Leibfried, T., "Mixed core design for power transformers to reduce core losses". *Optimization of Electrical and Electronic Equipment (OPTIM), 2017 International Conference on*. Brasov Rumania, submitted for publication.
- [74] Freitag, C., Leibfried T., Kasti, J., "New approach to calculate core losses in power transformers based on combination of FEM simulation and post processing algorithm". *19th International Symposium on High Voltage Engineering (ISH)*. University of West Bohemia Plisen Czech Republic, Aug. 28, 2015. ISBN: 978-80-261-0477-3.
- [75] Freitag, C., Stumpf, J., Höllig, M., Leibfried T., "Untersuchung der Entmagnetisierung von Transformatorkernen". *Diagnostik elektrischer Betriebsmittel 2012 (ETG-FB 134)*. Fulda Germany, Nov. 15, 2012. ISBN: 978-3-8007-3465-8.
- [76] Freitag, C., Joost, C., Leibfried, T., "Modified Epstein frame for measuring electrical steel under transformer like conditions". *High Voltage Engineering and Application (ICHVE), 2014 International Conference on*. Poznan Poland, Sept. 11, 2014, DOI: 10.1109/ICHVE.2014.7035441.
- [77] Freitag, C., Leibfried T., Bender, T., "Magnetic hysteresis model based on harmonics in the magnetic field". *18th International Symposium on High Voltage Engineering (ISH)*. Hanyang University Seoul Korea, Aug. 25, 2013. ISBN: 978-89-86510-18-8.
- [78] Freitag, C., Leibfried, T., "Transformatormodell auf Basis eines Hysterese Modells des im Transformatorkern verwendeten Elektrolechs". *Diagnostik elektrischer Betriebsmittel 2014 (ETG-FB 144)*. Berlin Germany, Nov. 25, 2014. ISBN: ISBN 978-3-8007-3648-5.

- [79] Freitag, C., Leibfried T., "Advanced magnetic hysteresis model describing polarization and frequency dependence". *Optimization of Electrical and Electronic Equipment (OPTIM), 2014 International Conference on*. Brasov Rumania, May 24, 2014, DOI: 10.1109/OPTIM.2014.6850905.

#### C.4 Supervised thesis by author

- [80] Höllig, M., "Entwicklung eines Gerätes zur Messung der Remanenz in Transformator-kernen", *Bachelor's Thesis*, Karlsruhe Institute for Technology, 2012.
- [81] J. Stumpf, "Entwicklung eines Algorithmus zur Entmagnetisierung von Leistungs-transformatorkernen", *Bachelor's Thesis*, Karlsruhe Institute for Technology, 2012.
- [82] Jansenberger, F., "Entwicklung eines Messsystems zur Bestimmung der magneti-schen Eigenschaften von Elektrolech in Normal-Richtung", *Master's Thesis*, Karlsruhe Institute for Technology, 2016.
- [83] Kasti, J., "Untersuchung und Modellierung der Kernverluste in Leistungstransfor-matoren", *Bachelor's Thesis*, Karlsruhe Institute for Technology, 2014.
- [84] Stumpf, J., "Modellierung und Simulation eines Leistungstransformators mit einem neuen Kernaufbau mit der FEM-Software MAXWELL", *Master's Thesis*, Karls-ruhe Institute for Technology, 2015.
- [85] Frank, M., "Untersuchung von Stromalgorithmen zur Entmagnetisierung von Leis-tungstransformatorkernen", *Bachelor's Thesis*, Karlsruhe Institute for Technology, 2013.
- [86] Joost, C., "Entwicklung eines Gerätes zur Messung der magnetischen Eigenschaften von Elektrolech", *Master's Thesis*, Karlsruhe Institute for Technology, 2013.

## D Nomenclature

|                   |  |                            |
|-------------------|--|----------------------------|
| $a$               | Grade ratio  | %                          |
| $A$               | Assigned cost of no-load losses per watt                         | €/W                        |
| $A_1$             | Part of core cross section made of better steel grade            | m <sup>2</sup>             |
| $A_2$             | Part of core cross section made of worse steel grade             | m <sup>2</sup>             |
| $A_{Cu}$          | Copper cross section of a winding                                | m <sup>2</sup>             |
| $A_{Fe}$          | Cross section of magnetic material                               | m <sup>2</sup>             |
| $A_{Fe, adapt}$   | Adapted core cross section                                       | m <sup>2</sup>             |
| $A_{Fe, rated}$   | Rated core cross section   | m <sup>2</sup>             |
| $a_h$             | Cosine harmonic component in the magnetic field of the order $h$ | A/m                        |
| $A_{ms}$          | Area of a SST sample's middle section                            | m <sup>2</sup>             |
| AC                | Alternating Current  |                            |
| A/D               | Analog/Digital converter   |                            |
| $B$               | Magnetic flux density  | T                          |
| $b$               | Excitation ratio   | 1                          |
| $BF$              | Building factor  | 1                          |
| $b_h$             | Cosine harmonic component in the magnetic field of the order $h$ | A/m                        |
| $B_{ms}$          | Flux density in the middle section of a SST sample               | T                          |
| $B_R$             | Remanent flux density / Remanence                                | T                          |
| $B_S$             | Saturation flux density  | T                          |
| $\bar{B}$         | Average flux density value                                       | T                          |
| $\hat{B}$         | Magnetic flux density amplitude                                  | T                          |
| $\hat{B}_{rated}$ | Rated flux density amplitude                                     | T                          |
| $\hat{B}_{adpt}$  | Adapted flux density amplitude                                   | T                          |
| $C$               | Initial cost of energy   | €/kWh                      |
| $c$               | Cost ratio   | %                          |
| $\chi_m$          | Magnetic susceptibility  | 1                          |
| $C_0$             | Hysteresis loss parameter  | (A m <sup>4</sup> )/(kg s) |

|                  |   |                          |
|------------------|---|--------------------------|
| $C_1$            | Excess / Anomalous loss parameter                         | $(A\ m^3)/(V^{0.5}\ kg)$ |
| $C_{Cu}$         | Specific price of copper                                  | €/kg                     |
| $CMC$            | Core manufacturing cost                                   | €                        |
| $CMC_{12}$       | Mixed core manufacturing cost                             | €                        |
| $CMC_3$          | Reference core manufacturing cost                         | €                        |
| $CMC_{adpt, 12}$ | Manufacturing cost of adapted mixed core                  | €                        |
| $CMC_{adpt, 3}$  | Manufacturing cost of adapted reference core              | €                        |
| $c_p$            | Proportional constant for eddy current loss approximation | 1                        |
| $C_S$            | Specific price  | €/kg                     |
| $C_{S1}$         | Specific price of better steel grade                      | €/kg                     |
| $C_{S2}$         | Specific price of worse steel grade                       | €/kg                     |
| $C_{S3}$         | Specific price of reference steel grade                   | €/kg                     |
| $C_{y/2}$        | Cost of energy at mid-life of a transformer               | €/kWh                    |
| $d$              | Thickness   | m                        |
| $d_{plastic}$    | Thickness of plastic layer                                | m                        |
| $d_{sheet}$      | Thickness of steel sheet                                  | m                        |
| $\delta$         | Relative flux density deviation                           | %                        |
| DC               | Direct Current  |                          |
| $E$              | Electric field strength                                   | V/m                      |
| EMC              | Electromagnetic Compatibility                             |                          |
| EPF              | Epstein Frame   |                          |
| $f$              | Frequency   | Hz                       |
| $FF$             | Form Factor   | 1                        |
| FE               | Finite Element  |                          |
| FEA              | Finite Element Analysis                                   |                          |
| FEM              | Finite Element Method                                     |                          |
| $G_{4qc}$        | Four-quadrant chopper gain                                | 1                        |
| $\gamma$         | Relative standard deviation                               | %                        |
| GSU              | Generator Step-up Transformer                             |                          |
| GUI              | Graphic User Interface                                    |                          |

|                        |  |                  |
|------------------------|--|------------------|
| $H$                    | Magnetic field strength                    | A/m              |
| $h$                    | Order of harmonic component                | 1                |
| $H_1$                  | Fundamental of the magnetic field strength | A/m              |
| $H_C$                  | Magnetic coercivity                        | A/m              |
| $h_N$                  | Height of a winding                        | m                |
| $H_L$                  | Inductive magnetic field strength value    | A/m              |
| $h_{\max}$             | Maximum number of harmonic orders          | 1                |
| $H_R$                  | Resistive magnetic field strength value    | A/m              |
| $\hat{H}$              | Magnetic field strength amplitude          | A/m              |
| $\bar{H}$              | Average magnetic field strength            | A/m              |
| HVDC                   | High Voltage Direct Current                |                  |
| $I$                    | Current                                    | A                |
| $i$                    | Finite element / point index               | 1                |
| $I_{\mu, \text{real}}$ | Real part of magnetization current         | A                |
| $I_{\mu, \text{im}}$   | Imaginary part of magnetization current    | A                |
| $I_1$                  | Primary current                            | A                |
| $I_{1, 1}$             | Fundamental of primary current             | A                |
| $I_{1, 3}$             | Third harmonic of primary current          | A                |
| $I_{1, \text{im}}$     | Imaginary part of primary current          | A                |
| $I_{1, \text{real}}$   | Real part of primary current               | A                |
| $IC$                   | Initial Cost                               | €                |
| $I_{EC}$               | Eddy current                               | A                |
| $I_{\text{load}}$      | Load current                               | A                |
| $I_{SC}$               | Short circuit current                      | A                |
| $J$                    | Polarization                               | T                |
| $J_1$                  | Current density                            | A/m <sup>2</sup> |
| $\hat{J}$              | Magnetic polarization amplitude            | T                |
| $\hat{J}_{\text{sat}}$ | Saturation polarization                    | T                |
| $j$                    | Sampling index                             | 1                |
| $k$                    | Average loading during life time           | 1                |

|                   |   |       |
|-------------------|---|-------|
| $K_P$             | Proportional action coefficient         | 1     |
| $L$               | Inductance                              | Vs/A  |
| $l$               | Length                                  | m     |
| $l_{Cu}$          | Length of copper wire                   | m     |
| $l_{Fe}$          | Magnetic path length                    | m     |
| $L_m$             | Main inductance                         | Vs/A  |
| $L_{\sigma 1}$    | Leakage inductance                      | Vs/A  |
| $M$               | Magnetization                           | A/m   |
| $m$               | Mass                                    | kg    |
| $\mu$             | Magnetic permeability                   | Vs/Am |
| $\mu_0$           | Absolute permeability                   | Vs/Am |
| $\mu_{diff}$      | Differential permeability               | Vs/Am |
| $\mu_r$           | Relative permeability                   | 1     |
| $m_a$             | Active mass                             | kg    |
| $m_{Core}$        | Core mass                               | kg    |
| $m_{Core, rated}$ | Rated core mass                         | kg    |
| $m_{Cu}$          | Copper mass                             | kg    |
| $m_{Ps1}$         | Core mass made of better steel grade    | kg    |
| $m_{Ps2}$         | Core mass made of worse steel grade     | kg    |
| $m_{Ps3}$         | Core mass made of reference steel grade | kg    |
| $m_{sample}$      | Sample mass                             | kg    |
| MSL               | Multi-Step Lap                          |       |
| $n$               | Controller cycle index                  | 1     |
| $N$               | Number of turns in a winding            | 1     |
| $N_1$             | Number of turns in primary winding      | 1     |
| $N_2$             | Number of turns in secondary winding    | 1     |
| $N_{HV}$          | Number of turns in High Voltage winding | 1     |
| $N_{LV}$          | Number of turns in Low Voltage winding  | 1     |
| $N_s$             | Number of samples                       | 1     |
| NDT               | Normal Direction Tester                 |       |
| $oh$              | Operating hours per year                | h     |

|                         |  |          |
|-------------------------|--|----------|
| $\omega$                | Angular frequency                            | 1/s      |
| $p$                     | Loss ratio                                   | %        |
| $P_0$                   | No load losses                               | W        |
| $P_{12}$                | Mixed core losses                            | W        |
| $P_{12, \text{adpt}}$   | Adapted mixed core losses                    | W        |
| $P_3$                   | Reference core losses                        | W        |
| $P_{3, \text{adpt}}$    | Adapted reference core losses                | W        |
| $P_{\text{calculated}}$ | Calculated core losses                       | W        |
| $P_{\text{Core}}$       | Core losses                                  | W        |
| $P_{\text{EC}}$         | Eddy current loss                            | W        |
| $P_{\text{element}}$    | Power loss of a finite the element           | W        |
| $P_{\text{entire}}$     | Entire losses                                | W        |
| $P_{\text{estimated}}$  | Estimated core losses                        | W        |
| $P_k$                   | Load losses                                  | W        |
| $P_{k, \text{adpt}}$    | Adapted load losses                          | W        |
| $P_{\text{measured}}$   | Measured core losses                         | W        |
| $P_S$                   | Specific total loss                          | W/kg     |
| $P_{S, \text{EC}}$      | Specific eddy current loss                   | W/kg     |
| $P_{S, \text{EX}}$      | Specific excess / anomalous loss             | W/kg     |
| $P_{S, \text{H}}$       | Specific hysteresis loss                     | W/kg     |
| $P_{S1}$                | Specific total loss of better steel grade    | W/kg     |
| $P_{S2}$                | Specific total loss of worse steel grade     | W/kg     |
| $P_{S3}$                | Specific total loss of reference steel grade | W/kg     |
| $P_{\text{SC}}$         | Short circuit direct power                   | W        |
| $p_1$ to $p_4$          | Points of a finite the element               |          |
| $\Phi$                  | Magnetic flux                                | Vs       |
| $q$                     | Number of finite elements                    | 1        |
| $R$                     | Resistance                                   | $\Omega$ |
| $r$                     | Discount rate for the investment per year    | %        |
| $R_{\text{AC}}$         | AC resistance                                | $\Omega$ |
| $R_{\text{AC, adpt}}$   | Adapted AC resistance                        | $\Omega$ |

|                     |   |                   |
|---------------------|---|-------------------|
| $r_{\text{adpt}}$   | Radius of adapted core cross section            | m                 |
| $R_{\text{Device}}$ | Input resistance of the measurement device      | $\Omega$          |
| $R_{\text{Fe}}$     | Equivalent core loss resistance                 | $\Omega$          |
| $R_{\text{m}}$      | Magnetic resistance                             | A/Vs              |
| $r_{\text{rated}}$  | Radius of rated core cross section              | m                 |
| $R_{\text{Shunt}}$  | Shunt resistor                                  | $\Omega$          |
| $\rho$              | Mass density                                    | kg/m <sup>3</sup> |
| $\rho_{\text{Cu}}$  | Specific resistance of copper                   | $\Omega\text{m}$  |
| <b>RMS</b>          | Root Mean Square                                |                   |
| $s$                 | Number of steel grade combination               | 1                 |
| $\sigma$            | Electric conductivity                           | $\Omega\text{m}$  |
| $S_{\text{dapt}}$   | Peripheral length of adapted core cross section | m                 |
| $S_{\text{R}}$      | Rated power                                     | VA                |
| $S_{\text{rated}}$  | Peripheral length of rated core cross section   | m                 |
| $S_{\text{S}}$      | Specific apparent power                         | VA/kg             |
| $S_{\text{SC}}$     | Short circuit apparent power                    | VA                |
| <b>SSL</b>          | Single-Step Lap                                 |                   |
| <b>SST</b>          | Single Sheet Tester                             |                   |
| $T$                 | Cycle time / Period                             | s                 |
| $t$                 | Time  | s                 |
| $\Delta t$          | Simulation time step                            | s                 |
| $T_{\text{C}}$      | Controller cycle time                           | s                 |
| <b>TCO</b>          | Total Cost of Ownership                         | €                 |
| <b>THD</b>          | Total Harmonic Distortion                       | %                 |
| $T_{\text{I}}$      | Reset time                                      | s                 |
| $\Theta$            | Magneto-motive force                            | A                 |
| $T_1$               | Transformer 1                                   |                   |
| $T_2$               | Transformer 2                                   |                   |
| $T_3$               | Transformer 3                                   |                   |
| $T_4$               | Transformer 4                                   |                   |
| $U$                 | Voltage   | V                 |

|                      |   |              |
|----------------------|---|--------------|
| $U_2$                | Secondary voltage                       | V            |
| $U_{2, n}$           | Measured secondary voltage of cycle $n$ | V            |
| $U_{2, \text{ref}}$  | Reference secondary voltage             | V            |
| $U_h$                | Harmonic voltage component of order $h$ | V            |
| $U_{\text{HV}}$      | Voltage of High Voltage winding         | V            |
| $U_{\text{LV}}$      | Voltage of Low Voltage winding          | V            |
| $V$                  | Volume                                  | $\text{m}^3$ |
| $v$                  | Magnetic voltage                        | A            |
| $V_{\text{element}}$ | Volume of a finite the element          | $\text{m}^3$ |
| VBA                  | Visual Basic                            |              |
| $w$                  | Width                                   | m            |
| $WMC$                | Winding manufacturing cost              | €            |
| $WMC_{\text{adpt}}$  | Adapted winding manufacturing cost      | €            |
| $W_s$                | Specific work                           | Ws/kg        |
| $X$                  | Assigned cost per watt                  | €/W          |
| $y$                  | Assumed transformer life time           | a            |
| $y_n$                | Controller output variable              | 1            |
| $y_n'$               | Improved controller output variable     | 1            |
| $z$                  | Annual increase of energy price         | %            |
| 2D                   | Two dimensional                         |              |
| 3D                   | Three dimensional                       |              |

